Hadrons dans un calorimètre électromagnétique silicium-tungstène hautement granulaire - Production du quark top à l'International Linear Collider

Philippe Doublet

LAL 11-222

THÈSE DE DOCTORAT

Présentée pour obtenir le grade de

Docteur en Sciences de l'Université Paris-Sud 11

Spécialité : **PHYSIQUE DES PARTICULES**

par

Philippe Doublet

Hadrons dans un calorimètre électromagnétique silicium-tungstène hautement granulaire

Production du quark top à l'International Linear Collider

Soutenue le 3 octobre 2011 devant le jury composé de :

Prof.	A. Stocchi	Président du jury
Dr.	T. Behnke	Rapporteur
Prof.	M. E. Peskin	Rapporteur
Prof.	B. C. Barish	Examinateur
Dr.	L. Serin	Examinateur
Dr.	R. Pöschl	Directeur de thèse
Dr.	F. Richard	Membre invité

Abstract

The International Linear Collider (ILC) is a proposed e^+e^- collider with a center-of-mass energy of 500 GeV or more, aimed at precision measurements, e.g. of a light Higgs boson that could be discovered soon at the Large Hadron Collider. Its detectors foresee the use of fine grained calorimeters to achieve the desired precisions.

This thesis presents the study of the response to hadrons of a highly granular silicon-tungsten electromagnetic calorimeter (SiW ECAL), and the study of top quark pair production at the ILC.

The SiW ECAL prototype developed by the CALICE collaboration was tested with beams of charged particles at FNAL in May and July 2008. After selecting single negatively charged pions entering the ECAL, its fine granularity is used to introduce a classification among four types of events, used to describe hadronic interactions.

Motivated by extra-dimensional models which may explain the A_{FB}^b LEP anomaly by modifying the couplings of third generation quarks to the Z boson, the semileptonic decay of the top quark is studied with a full simulation of the proposed ILD detector for the ILC at center-of-mass energy $\sqrt{s} = 500\,\text{GeV}$ and integrated luminosity $\mathcal{L} = 500\,\text{fb}^{-1}$. Detector performances permit to reach efficiencies larger than 70% in finding those events with a purity larger than 95%. This translates into a relative accuracy of about 1% on both the left-right asymmetry of top production $A_{LR}^{0,t}$ and the top forward-backward asymmetry A_{FB}^t with electrons polarized at 80% and no polarization of the positrons. The relative uncertainties in the left and right couplings of the top quark to the Z boson could be as good as 0.9% and 1.5%.

Résumé

L'International Linear Collider (ILC) est un projet de futur collisionneur e^+e^- opérant à une énergie nominale dans le centre de masse de 500 GeV. Il fera des mesures de précision, par exemple d'un boson de Higgs léger qui pourrait être bientôt découvert au Large Hadron Collider. Les détecteurs de l'ILC prévus à cet effet seront composés de calorimètres à haute granularité.

Cette thèse présente l'étude de la réponse d'un calorimètre électromagnétique silicium-tungstène hautement granulaire (ECAL SiW) ainsi que l'étude de la production du quark top à l'ILC.

Le prototype d'un ECAL SiW développé par la collaboration CALICE a été testé sous faisceaux de particules chargées au FNAL en Mai et Juillet 2008. Après avoir sélectionné des pions chargés négativement et entrant dans le ECAL, sa haute granularité est mise à profit pour introduire une classification en quatre types d'événements, afin de décrire des interactions hadroniques.

Des modèles de dimensions supplémentaires expliquent l'anomalie A_{FB}^b du LEP par une modification des couplages des quarks de troisième génération au boson Z. Ces effets motivent l'étude de la désintégration semileptonique des paires de quarks top, effectuée ici au moyen d'une simulation complète du détecteur ILD proposé pour l'ILC à une énergie dans le centre de masse $\sqrt{s} = 500\,\text{GeV}$ pour une luminosité intégrée $\mathcal{L} = 500\,\text{fb}^{-1}$. Les performances de ce détecteur permettent d'atteindre des efficacités de sélection de plus de 70% avec une pureté meilleure que 95%. Cela se traduit par une précision relative d'environ 1% sur l' asymétrie gauche-droite de la production du quark top $A_{LR}^{0,t}$ ainsi que sur l'asymétrie avant-arrière du quark top A_{FB}^t dans le cas où les électrons sont polarisés à 80% et pas les positrons. Les incertitudes relatives sur les couplages gauche et droit du quark top au boson Z peuvent aller jusqu'à 0.9% et 1.5%.

Acknowledgments

First of all, I would like to thank the two consecutive directors of the LAL, Guy Wormser and Achille Stocchi, for allowing me to pursue this thesis and to work in excellent conditions during these three years.

Second, I would like to thank all of the members of the jury. It is a real honor to have all of them in this jury and I am grateful for their approbation to be part of it.

Then I want to thank my supervisors Roman and François for everything they taught me. Their passion of physics and constant belief in my work has always motivated me to continue in this fascinating branch of particle physics.

It was a pleasure to have conversations with other friends of the LAL : Cécile, Olivier and Julien. And I am grateful for all of the discussions we had with Hengne, Michele, Thibault whom I worked with during the thesis and were of great help as well as Stephane from CERN. I wish to Jérémy who just started his PhD to have such fruitful relations.

La thèse n'est pas seulement la thèse et grâce aux enseignements que j'ai donnés, j'ai eu le plaisir de rencontrer et travailler avec une équipe dynamique. Merci à Christine, Laetitia, Rosa, Véronique, Fabien, Frédéric et Eric pour leur aide. Et je tiens à remercier plus particulièrement Fabienne qui a accepté d'être ma tutrice et m'a énormément apporté pendant ces trois années.

Cette thèse n'aurait pas abouti sans l'appui constant de mes amis. Audrey, Florent Alzetto du CAG et Marion, binôme et Flo, Romaing, Jimmy, M. La Bella, Clément, Mélanie, Minh, Hervé, Alex, Jean-Baptiste, Jean-Auguste, le mouz, Adrien, Jean-Sébastien et Jeanne, Laura, Jérémie, voisin, Mickael et Charly, papy, Vince et Vince de la Chô team, Andrey, Edwige, Nono, Bruno, Etienne, Claire, barbu, Soso, Tom, Karim, Serge, Alborosie. Merci.

Celle qui a subi le plus cette thèse et qui me subit au quotidien, c'est Audrey. Bien sûr, à partir de maintenant, c'est à moi de te le rendre et te le dire tous les jours. Merci pour tout.

Je tiens à remercier toute ma famille pour leur support et attention constante pendant ces trois années. Merci papa, maman, Isabelle, Bertrand et grand-mère ainsi que Claire et Jean-Philippe. Votre soutien a été important pour moi.

Un dernier mot à la mémoire de mon grand-père mort pendant ces trois années. Il avait été passionné de mathématiques par son professeur d'Alger et ne comprenait pas pourquoi j'ai choisi la physique. J'ai découvert en fin de thèse que son professeur, André Blanc-Lapierre, avait été un physicien de premier plan ainsi que directeur du LAL. Donc les gens bien font de la physique. Merci grand-père, place à la physique.

Contents

List of Figures

List of Tables

Chapter 1

Introduction

The Standard Model of particle physics describes the electromagnetic, weak and strong nuclear interactions. It has been developed in the middle of the 20th century and measured since then with great accuracy.

Despite the great success of the Standard Model over the past decades, some experimental and theoretical issues remain unknown. In particular, the presence of a spin 0 boson, the Higgs boson, is foreseen to explain that the observed particles of the Standard Model are massive. It has however not been discovered yet but the Large Hadron Collider (LHC) [web], a proton-proton collider at CERN, may soon provide an answer to its existence.

Models adding other particles to the actual Standard Model as well as others without any Higgs boson have also been proposed and are actively under study at the LHC. Some new physics is expected between 100 GeV and 1 TeV at the LHC, be it a Higgs or another mechanism. While the LHC may discover new particles soon, an electron-positron machine is expected to accurately measure the properties of e.g. a Higgs boson found at the LHC.

The International Linear Collider [BOW07] (ILC) is a proposed electron-positron collider aimed at precision measurements between center-of-mass energies of 90 GeV and 1 TeV. To achieve precision measurements, the design of detectors for the ILC is driven by the particle flow approach which foresees the use of highly granular calorimeters. Two important aspects were studied during this thesis and constitute its two parts: the use and potential of highly granular calorimeters and precisions measurements at the ILC.

The first part of this thesis will present results of test beams of a prototype of a highly granular silicon-tungsten electromagnetic calorimeter (SiW ECAL) with pions at energies ranging from 2 GeV to 10 GeV. The granularity of this ECAL is employed to find tracks inside its volume, find interactions of pions and classify them. On the one hand, this study compares the data with various Monte Carlo simulations in order to improve models of hadronic interactions. On the other hand, the introduced classification can improve identifications of several patterns by particle flow algorithms.

The second part will focus on analysis of the top quark production at the ILC using the semileptonic decay mode at a center-of-mass energy $\sqrt{s} = 500$ GeV with an integrated

luminosity of $\mathcal{L} = 500\,\mathrm{fb}^{-1}$. Emphasis will be put on some extra-dimensional scenarios and the possible distinction among them. It will illustrate the critical properties of the ILD detector relevant to this analysis, as well as emphasize the role of electron and positron polarization for precision physics.

The resulting organization is the following: this Chapter 1 reviews the important features of the Standard Model of particle physics. The Higgs mechanism will be described in order to facilitate its adaptation into extra-dimensional models. Some relevant questions for particle physics raised by experimental observations are then reviewed. These questions are relevant for the physics case of an ILC and justify its design. The first part will begin, Chap. 2, by recalling interactions of particles in matter, relevant for the analysis of hadrons in the SiW ECAL, with emphasis on the simulation of hadronic interactions. This calorimeter will be presented in Chap. 3 with its characteristics. Chapter 4 describes the beam line and the selection of events containing single pions in the test beam data. When possible, the same cuts are applied on both data and Monte Carlo simulations. In Chap. 5 the method to find and classify interactions is explained. This lead to the development of an algorithm which optimization on Monte Carlo samples is described. The results shown Chap. 6, following from the classification, give insights into the development of hadronic showers as implemented in some models used for simulations. The second part of the thesis will start Chap 7 by introducing theoretical motivations to study the top quark at the ILC: models of warped extra-dimensions which foresee deviations in the left and right couplings of the top quark to the Z boson. The top quark with its principal backgrounds for this analysis is presented in Chap. 8. Some relevant observables, in particular the left-right and forward-backward asymmetries of top pair production, are indicated and used to derive the sensitivities on the left and right couplings of the top quark to the Z boson. The ILD detector used for the top quark studies is described Chap. 9 and its relevant properties for the analysis of the semileptonic decay mode are shown Chap. 10. The steps to reconstruct this decay mode are described in Chap. 11. The final results on the asymmetries and the couplings of the top quark with particular emphasis on the extra-dimensional models.

1.1 The Standard Model of particle physics

Particle physics studies the components of matter and their interactions. They are described by the Standard Model (SM) of particle physics illustrated Fig. 1.1. It is a relativistic quantum field theory using local gauge symmetries. [1]

The electromagnetic, weak and strong interactions are all described within the SM. Gravitation is not included. The weakness of this interaction at the energies at which the SM is valid does not lead to measurable effects. Currently, there exists no satisfactory theory which includes gravity.

1. In all the text, we will use natural units: $\hbar = c = 1$. Energies, masses and momenta will be expressed in GeV.

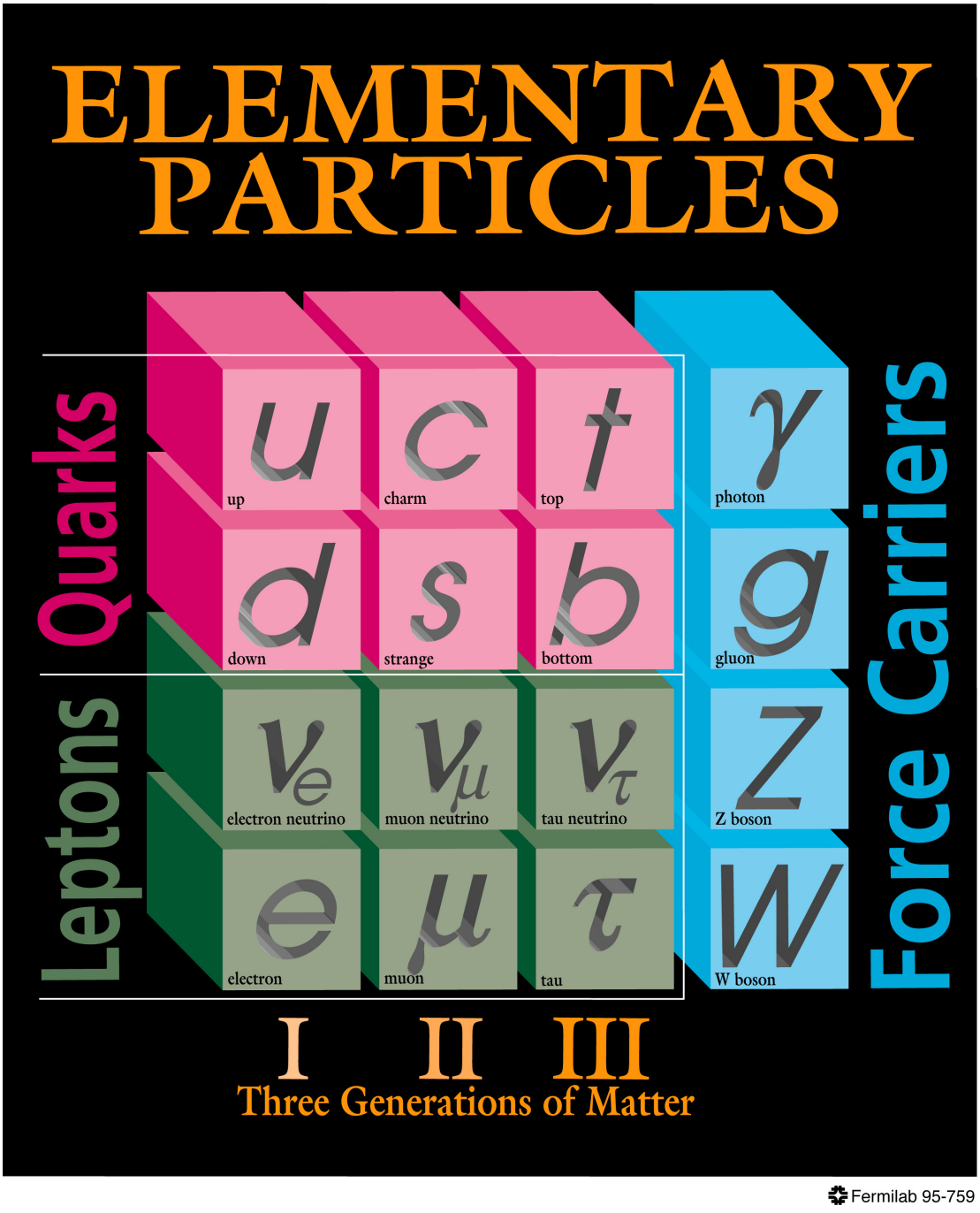

Figure 1.1: The Standard Model of particle physics. Fermions that build up matter are subdivided into three families of quarks and leptons. Vector bosons carry the strong, electromagnetic and weak forces. Picture taken from `http://www.fnal.gov/`.

1.1.1 Content of the SM

Spin 1/2 fermions are the building blocks of matter, divided in three families. They are organized in left-handed doublets and right-handed singlets under $SU(2)_L$ and charged under $U(1)_Y$ (where Y is the hypercharge). Leptons are color singlets while quarks are triplets under $SU(3)_c$ (c stands for color), the gauge group of the strong interaction. The electroweak group $SU(2)_L \times U(1)_Y$ is actually broken down to the electromagnetic group $U(1)_{em}$, giving the electric charge Q (in units of e) by:

$$Q = I_3^L + Y \tag{1.1}$$

where I_3^L is the third component of the $SU(2)_L$ isospin, with $I_3^L = \pm 1/2$ for left-handed fermions and $I_3^L = 0$ for right-handed fermions.

Spin 1 vector bosons mediate the interactions. The photon is massless and couples to electrically charged particles. The three bosons (Z^0 and $W^\pm$) mediate the weak force. There are 8 gluons associated to the strong interaction.

1.1.2 Electromagnetic interaction

Quantum electrodynamics (QED) is the quantum field theory used for electromagnetic interactions using the $U(1)_{em}$ gauge group. The simplest associated Lagrangian for a massless fermion ψ with a massless photon field A_μ is:

$$\mathcal{L} = \bar{\psi}(i\gamma^\mu D_\mu)\psi - \frac{1}{4}F_{\mu\nu}F^{\mu\nu} \tag{1.2}$$

where $D_\mu = \partial_\mu - iQeA_\mu$ is the covariant derivative with Q the electric charge of ψ in units of e ($Q = -1$ for an electron). The gauge invariant kinetic term of the fermion features the electromagnetic interaction $-ie(j^{em})^\mu A_\mu = -ie(\bar{\psi}\gamma^\mu Q\psi)A_\mu$. $F_{\mu\nu} = \partial_\mu A_\nu - \partial_\nu A_\mu$ is the strength tensor of the photon field.

This Lagrangian is invariant under

$$\left\{ \begin{array}{rcl} \psi & \rightarrow & \psi\, e^{iQe\chi(x)} \\ A_\mu & \rightarrow & A_\mu + \partial_\mu \chi \end{array} \right. \tag{1.3}$$

The strength of the electromagnetic interaction $\alpha = \dfrac{e^2}{4\pi\epsilon_0}$ is actually a running coupling constant depending on the transferred four-momentum squared, Q^2, in the reaction ($\alpha = 7.2973525376(50) \cdot 10^{-3} \approx \frac{1}{137}$ [Nak10] for zero exchanged momentum, and $\alpha(m_Z^2) \approx \frac{1}{128}$). Indeed, an electron can emit virtual photons which may convert into e^-e^+ pairs (but also into pairs of quark-anti-quark and the other charged leptons) with the positrons being attracted by the electron. The charge of the electron is thus screened and a probe moving closer and closer to the electron (large Q^2) would feel an increasing charge when penetrating the positrons' cloud.

1.1.3 Strong interaction

QCD Lagrangian Quantum chromodynamics (QCD) is the quantum field theory of strong interactions. The $SU(3)_c$ group is the relevant gauge group for three color charges. The gauge invariant Lagrangian of a massless quark q with fields of massless gluons G^a_μ $(a = 1, ..., 8)$ reads:

$$\mathcal{L} = \bar{q}(i\gamma^\mu D_\mu)q - \frac{1}{4}G^a_{\mu\nu}G^{\mu\nu}_a \tag{1.4}$$

where $D_\mu = \partial_\mu - igT_aG^a_\mu$, with g the coupling constant, $G^a_{\mu\nu} = \partial_\mu G^a_\nu - \partial_\nu G^a_\mu - gf_{abc}G^b_\mu G^c_\nu$ and T^a and f_{abc} are respectively the non-abelian group generators and the structure constants.

This group $SU(3)_c$ which is non-abelian leads to extra terms in the kinetic term of the gluon field which are triple and quadruple gluon couplings. These couplings are uniquely determined by the single coupling g.

Facts of QCD Due to the number of colors and families, the running of the QCD strength $\alpha_s = \frac{g^2}{4\pi}$ ($\alpha_s(m_Z^2) = 0.1184(7)$ [Nak10]) leads to different behaviors from the QED constant α: α_s features an asymptotic freedom.

The asymptotic freedom implies that the force between quarks at short distances is small (large Q^2). But it is strong at larger distances (small Q^2), which prevents the existence of colored objects. A quark-anti-quark pair cannot separate because of this, what leads to colorless mesons. However, if their energy is large enough, as the potential energy between the quark and anti-quark increases with their distance, it becomes at a given point sufficiently large to create a pair of quark-anti-quark and so on. Quark-anti-quark pairs are produced until the energy is insufficient to continue the process. The final state partons combine into hadrons. This process is called hadronization. The particles resulting from the primary quark form a jet: a cone of hadrons produced by the hadronization of the initial parton.

1.1.4 Electroweak interactions

The model of weak interactions first proposed by Fermi was an effective theory, valid at energies well below 100 GeV. The weak and electromagnetic interactions have been unified in the $SU(2)_L \times U(1)_Y$ by Glashow in 1961 [Gla61] and the actual model was proposed by Weinberg [Wei67] and Salam [Sal68].

The weak interactions have a V-A (vector - axial vector) structure. In particular, the charged current only acts on left-handed fermions (right-handed anti-fermions).

Using W^i_μ $(i = 1, 2, 3)$ for the vector fields of $SU(2)_L$ with coupling g and B_μ for the vector field of $U(1)_Y$ with coupling g', the basic electroweak interaction taken from the gauge covariant derivative applied on a fermion f can be written:

$$-ig(J^i)^\mu W^i_\mu - ig'(j^Y)^\mu B_\mu \tag{1.5}$$

The weak isospin current $J^i_\mu = \bar{f}\frac{\tau^i}{2}\gamma_\mu\frac{1-\gamma^5}{2}f$ only couples to left-handed fermions while $j^Y_\mu = \bar{f}Y\gamma_\mu f$ couples to all fermions charged under the hypercharge Y. The matrices τ^i $(i = 1, 2, 3)$ are the Pauli matrices.

Using $\tau_\pm = \frac{1}{2}(\tau_1 \pm i\tau_2)$ and $W^\pm_\mu = \dfrac{W^1_\mu \mp iW^2_\mu}{\sqrt{2}}$, the charged part can be identified with a $\frac{g}{\sqrt{2}}$ coupling.

The weak neutral current is known to have a right-handed component, which suggests that there be a mixing between the neutral W^3_μ and B_μ bosons to embed weak and electromagnetic interactions arising from the breaking of the $SU(2)_L \times U(1)_Y$ symmetry, down to $U(1)_{em}$. It is parametrized as:

$$\begin{array}{rcl} A_\mu &=& B_\mu \cos\theta_W + W^3_\mu \sin\theta_W \\ Z_\mu &=& -B_\mu \sin\theta_W + W^3_\mu \cos\theta_W \end{array} \tag{1.6}$$

where A_μ and Z_μ are now the physical states of the photon and Z boson. θ_W is the Weinberg or weak mixing angle. Requiring that the photon current is that of QED $(-ie\bar{f}\gamma^\mu Q f)$, one identifies the following relations:

$$\begin{array}{rcl} \dfrac{g'}{g} &=& \tan\theta_W \\ e &=& g'\cos\theta_W \end{array} \tag{1.7}$$

and the couplings to Z_μ are:

$$\frac{e}{\sin\theta_W \cos\theta_W}(I^L_3 - Q\sin^2\theta_W) \tag{1.8}$$

This form shows that the couplings are different from the pure left-handed couplings of $SU(2)_L$ because of the $Q\sin^2\theta_W$ term that allows coupling of the Z with charged right-handed fermions.

1.2 Generating the masses of particles

So far we have omitted masses of gauge bosons and fermions, whereas fermions, the $W^\pm$ and the Z bosons are known to be massive particles. Because of the group structure, terms like $m\bar{\psi}\psi = m(\bar{\psi}_L\psi_R + \bar{\psi}_R\psi_L)$ are forbidden, since it would not be a scalar under $SU(2)_L \times U(1)_Y$. And the gauge mass terms $\dfrac{1}{2}m^2_A A_\mu A^\mu$ are not gauge invariant.

1.2.1 Spontaneous symmetry breaking

Let us consider the following Lagrangian of a real scalar field ϕ under a quartic potential V:

$$\mathcal{L} = T - V = \frac{1}{2}(\partial_\mu\phi)^2 - (\frac{1}{2}\mu^2\phi^2 + \frac{1}{4}\lambda\phi^4) \tag{1.9}$$

In the case where $\mu^2 > 0$ and $\lambda > 0$, this Lagrangian describes a scalar particle of mass μ with a quartic self-coupling. The ground state corresponds to $\phi = 0$ and respects the symmetry of the Lagrangian $\phi \to -\phi$.

In the case where $\mu^2 < 0$, the μ-term is not the mass term anymore. The potential V is minimum for $\phi = \pm v$, where $v = \sqrt{-\mu^2/\lambda}$. Developing the field around the minimum v: $\phi(x) = v + \eta(x)$ leads to the Lagrangian

$$\mathcal{L}' = \frac{1}{2}(\partial_\mu \eta)^2 - \frac{1}{2}(-2\mu^2)\eta^2 - \lambda v \eta^3 - \frac{1}{4}\lambda \eta^4 - \frac{1}{4}\mu^2 v^2 \tag{1.10}$$

The η field is a massive scalar of mass $m_\eta = \sqrt{-2\mu^2}$ with triple and quartic self-couplings. The choice of the vacuum ($+v$ rather than $-v$) apparently breaks the symmetry of the Lagrangian. This process is known as spontaneous symmetry breaking and one sees that the η particle is the physical field that is used for perturbative calculations.

1.2.2 Higgs mechanism

Applying spontaneous symmetry breaking to a local gauge symmetry is the "Higgs mechanism" that allows to give masses to gauge bosons. Adding a $U(1)$ local gauge symmetry to the previous Lagrangian, the new Lagrangian reads:

$$\mathcal{L} = D_\mu \phi^\dagger D^\mu \phi - (\mu^2 \phi^\dagger \phi + \lambda(\phi^\dagger \phi)^2) - \frac{1}{4} F_{\mu\nu} F^{\mu\nu} \tag{1.11}$$

where $D_\mu = \partial_\mu - ieA_\mu$, A_μ and $F_{\mu\nu}$ are like in QED and ϕ is now a complex scalar field. To generate masses via spontaneous symmetry breaking, the parameter μ^2 must be taken negative. This allows to develop ϕ around the minimum of its potential, writing $\phi(x) = (\frac{v+h(x)}{\sqrt{2}})e^{i\frac{\theta(x)}{v}}$, where $v = \sqrt{\frac{-\mu^2}{\lambda}}$, and h and θ are two real fields. The potential of the ϕ field in 1.11 leads to a massive scalar h like in 1.10. And inserting this expression in the kinetic term of ϕ in 1.11 leads to:

$$\begin{aligned} D_\mu \phi^\dagger D^\mu \phi &= \tfrac{1}{2}(\partial_\mu h)^2 + \left[\left(\tfrac{v+h}{\sqrt{2}}\right)\left(-\tfrac{\partial_\mu \theta}{v} + eA_\mu\right)\right]^2 \\ &= \tfrac{1}{2}(\partial_\mu h)^2 + \tfrac{1}{2}(\partial_\mu \theta)^2 + \tfrac{v^2 e^2}{2} A_\mu^2 + \text{interacting terms} \end{aligned} \tag{1.12}$$

The mass of the gauge boson A_μ is thus generated via the interaction term $|-ieA_\mu\phi|^2$ embedded in this covariant derivative squared term of the Lagrangian, when ϕ is developed around its vacuum expectation value and is here $M_A = ve$. "Interacting terms" in the previous equation correspond to the terms involving the product of at least two different fields (h, θ or A_μ) and are not of interest in this discussion.

One is left with a massive gauge boson, as well as one massive field h called the Higgs field, and a massless boson θ. This is the illustration of the Goldstone theorem: after a spontaneous symmetry breaking of a local gauge symmetry, a massive gauge boson is created but a massless boson occurs because of the choice of the ground state. θ is a Goldstone boson but is not physical. By choosing the gauge transformation: $A_\mu \to A_\mu + \frac{1}{ev}\partial_\mu \theta$, the terms in θ will vanish in the resulting Lagrangian and one is left with observable particles only.

1.2.3 Electroweak symmetry breaking: boson masses

Following the recipe of the previous section, we add a doublet of complex scalar fields $\phi = \begin{pmatrix} \phi^+ \\ \phi^0 \end{pmatrix}$ (i.e. four real fields) to the electroweak Lagrangian which must be invariant under the $SU(2)_L \times U(1)_Y$ gauge symmetry, with hypercharge $Y_\phi = 1/2$. The goal is to generate the masses of the $W^\pm$ and Z gauge bosons:

$$\mathcal{L}_\mathcal{H} = (D_\mu \phi)^\dagger D^\mu \phi - \left(\mu^2 \phi^\dagger \phi + \lambda (\phi^\dagger \phi)^2\right) \tag{1.13}$$

where $D_\mu = \partial_\mu - ig\frac{\tau^i}{2}W_\mu^i - ig' Y B_\mu$.

The potential of the field ϕ is minimum for $\phi^\dagger\phi = -\frac{\mu^2}{2\lambda} = \frac{v^2}{2}$. The choice of a value around which the field will be expanded will break the symmetry of the Lagrangian. We choose as a minimum $\begin{pmatrix} 0 \\ \frac{v}{\sqrt{2}} \end{pmatrix}$ and expand around this minimum the field $\phi = \begin{pmatrix} 0 \\ \frac{v+h(x)}{\sqrt{2}} \end{pmatrix} e^{i\tau^i \theta^i(x)}$, where the four scalar fields are θ^i $(i = 1, 2, 3)$ and h. Using this form, θ^i are the Goldstone bosons which will vanish after a gauge invariant redefinition of the gauge fields and the mass of the Higgs boson is $M_h = \sqrt{-\mu^2}$.

When developing the kinetic term $(D_\mu \phi)^\dagger D^\mu \phi$ around the vacuum v, it gives rise to masses for gauge bosons via $\left|\left(-ig\frac{\tau^i}{2}W_\mu^i - ig' Y B_\mu\right)\phi\right|^2$:

$$\begin{aligned} M_{W^\pm} &= \frac{gv}{2} \\ M_Z &= \frac{gv}{2\cos\theta_W} = \frac{M_W}{\cos\theta_W} \end{aligned} \tag{1.14}$$

The photon remains massless since $U(1)_{em}$ is left unbroken.

1.2.4 Fermion masses

Since left-handed fermions (right-handed anti-fermions) are incorporated in an $SU(2)_L$ doublet and right-handed fermions (left-handed anti-fermions) are singlet under this group, it is not possible to incorporate mass terms in the Lagrangian of the form $m\bar{\psi}\psi = m(\bar{\psi}_L\psi_R + \bar{\psi}_R\psi_L)$ since it does not respect the $SU(2)_L$ invariance.

The Higgs field being a doublet of $SU(2)_L$, it can be used to write a gauge invariant Yukawa coupling between fermions and developed around its vacuum expectation value. Using up and down quarks as an example:

$$\begin{aligned} \Delta\mathcal{L} &= -\lambda_d \left(\bar{\Psi}_L \phi d_R + \bar{d}_R \phi^\dagger \Psi_L\right) \\ &= -\frac{\lambda_d v}{\sqrt{2}}(\bar{d}_L d_R + \bar{d}_R d_L) - \frac{\lambda_d}{\sqrt{2}} h(\bar{d}_L d_R + \bar{d}_R d_L) \end{aligned} \tag{1.15}$$

where the $SU(2)_L$ doublet is $\Psi_L = \begin{pmatrix} u_L \\ d_L \end{pmatrix}$ and d_R is the right-handed component of the down quark d considered which acquires the mass $m_d = \lambda_d v/\sqrt{2}$ seen in the first term. The second term is the Yukawa coupling of the fermion to the Higgs boson h with the coupling parameter $\lambda_d/\sqrt{2} = m_d/v$ directly proportional to the mass of the fermion.

To generate a mass for the up quark u of the $SU(2)_L$ doublet, one introduces another conjugate doublet $\phi' = i\tau_2\phi^*$ (where ϕ^* is the complex conjugate of ϕ). It transforms identically to ϕ and using the same form of Lagrangian that 1.15, the fermion will acquire a mass in the same way.

1.3 Questions to answer

The Standard Model has been tested to high precision in the last thirty years at lepton colliders, such as SLC and LEP and at hadron colliders such as SPS and TeVatron. A summary of the electroweak precision data is given in Fig. 1.2.

However some issues remain unexplained by the Standard Model. The most important questions in particle physics are summarized in a report written by the High Energy Advisory Panel in 2004 [Pan, Lyk06]. Some relevant questions for this thesis will be briefly sketched here.

So far, the Higgs boson has not been discovered. LEP, SLC and TeVatron have set limits on a SM Higgs boson or Higgs bosons coming from other theories and there is no evidence of its existence. The data favor a low mass Higgs boson, between about 115 GeV and 160 GeV at 95% confidence level in the case of the SM. If a SM Higgs exists, it is highly probable that it will be discovered by the Large Hadron Collider (LHC) at CERN, in the forthcoming years. After that, precision measurements need to pin down exactly the nature of the discovered boson.

Apart from its role in the generation of masses, a light Higgs boson is also needed to dump the rise of e.g. the $W_L^+W_L^- \to W_L^+W_L^-$ scattering cross-section, where the subscript L stands for longitudinally polarized. This cross-section would violate unitarity at around 1 TeV center-of-mass energy [Djo08]. If the Higgs boson were not to exist, some new physics would be needed in the TeV range to restore unitarity and be responsible for the generation of masses.

Masses can obey large hierarchies. Gravitation which is not included in the SM acts at a mass scale given by the Planck mass $M_{Pl} = 1/\sqrt{G} \approx 10^{19}\,\text{GeV}$, where $G = 6.67428(67) \times 10^{-11}\,\text{m}^3\text{kg}^{-1}\text{s}^{-2}$ is Newton's gravitational constant. The typical masses of the electroweak bosons are of about 100 GeV, like the preferred value of the mass of the SM Higgs boson. This is a hierarchy of 17 orders of magnitude which should be understood in a theory implementing gravitation in the SM.

Observations of gravitational effects in astrophysics also indicate that another form of matter called "dark matter" exists. Both dark matter and the previous hierarchy problem can be accommodated in supersymmetry (SUSY). SUSY theories add to the actual content of the SM, partners which spin differs by half a spin unit from the SM ones. Some of these partners can be candidates for dark matter. Additionally, SUSY

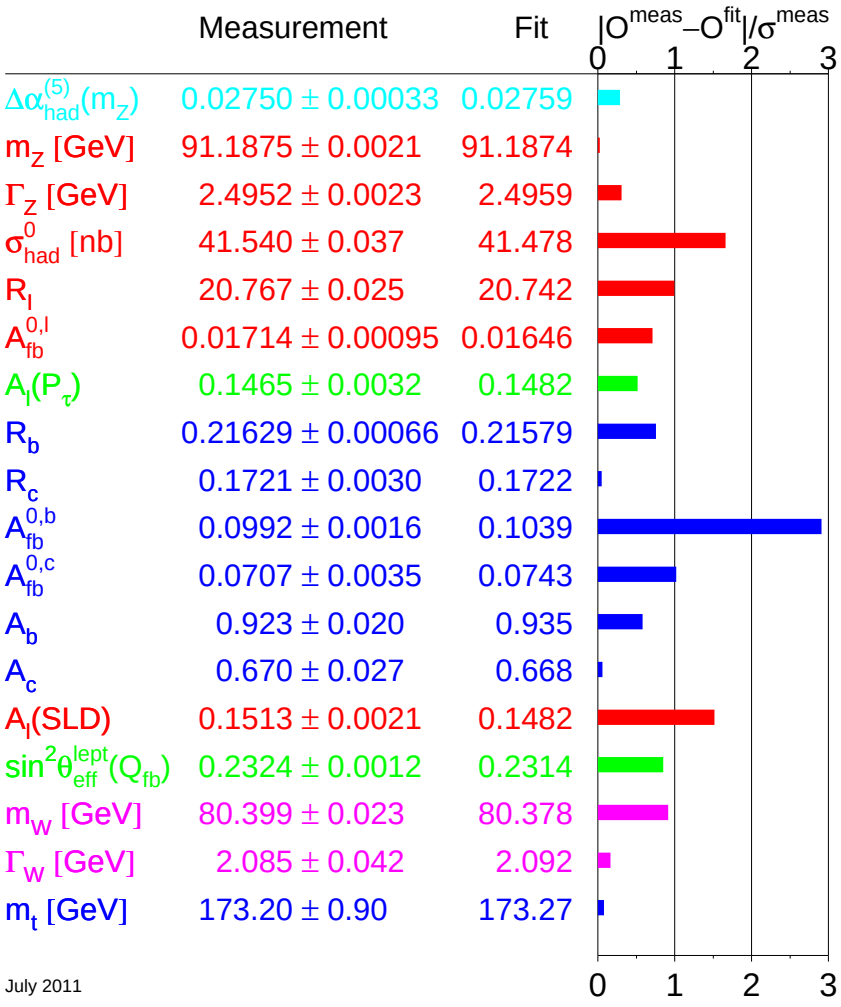

Figure 1.2: Comparison of measurements of important SM observables and their SM values using a global χ^2 fit. Also shown is the pull of each measurement: the difference between the measured value and its SM expectation in unit of the measurement uncertainty [The06]. Updated picture taken from `http://lepewwg.web.cern.ch/LEPEWWG/plots/summer2011/`.

predicts preferably a low mass Higgs boson.

There are also issues with flavor i.e. the three generations of quarks and leptons. For instance, Fig. 1.2 includes the asymmetry $A_{FB}^{0,b}$ which is in tension with the other electroweak precision data. This represents the asymmetry in the number of produced events containing a bottom quark in the forward hemisphere of the detector with respect to the backward hemisphere. Its deviation from the preferred SM value may be a sign that the coupling of the bottom quark to the Z boson needs to be modified. According to the theory, this may be caused by new physics acting mainly on heavy fermions. In this case the effect is expected to be amplified for top quarks in the final state.

The top quark is the heaviest elementary particle known with a mass of about 173 GeV, while an up quark weights only a couple of MeV and less than 1 eV for a neutrino. This represents 12 orders of magnitude in the mass spectrum of the fermions and cannot be explained with the current Higgs mechanism where the masses of the fermions are free parameters. The origin of this hierarchy may be indicated by the heavier fermions, as suggested by the discrepancy in the bottom quark sector with $A_{FB}^{0,b}$.

While SUSY alone does not explain this fermionic hierarchy, other theories addressing this issue as well are discussed in Chap. 7.

1.4 The International Linear Collider

The LHC at CERN is now the most energetic collider ever built. It collides protons at energies in the center-of-mass of 7 TeV and aims at discoveries of a Higgs boson, SUSY or other physics beyond the Standard Model.

It is a worldwide consensus that the next machine after the LHC will be a linear electron positron collider [Acc]. It would complement the LHC by providing much more precise measurements and eventually additional discoveries. Currently the most advanced proposal is the International Linear Collider (ILC) which will be described in the following. The worldwide efforts and ongoing R&D on the ILC are coordinated by the Global Design Effort (GDE). The major baseline of the ILC was documented in 2007 in a "Reference Design Report" [BOW07, DLM$^+$07, PTW07, BDJM07]. The goal of the GDE is now to provide a "Technical Design Report" by the end of 2012 which will assess changes to the baseline in particular to better optimize the costs and performances. An alternative at higher center-of-mass energies than the ILC is the Compact Linear Collider (CLIC).

1.4.1 Physics cases for the ILC

Measuring the properties of a light Higgs boson or revealing other physics beyond the SM which must appear at an energy scale of about 1 TeV justifies the need for a precision machine in this energy range. Different scenarios of physics are envisaged for the ILC [Ric07].

LHC should soon provide an essential answer to the question: "is there a light Higgs as predicted by the SM and a minimal version of SUSY (MSSM) ?" In case there is a

Higgs only and no accompanying signal, the question of an SM-alone scenario will be raised. The answer would need to test the Higgs, but also top quark and W pairs to a precision which would require a linear collider. This can be done with an ILC operating at 500 GeV. In case there are other accompanying signals from SUSY or other theories, one would use this information to optimize accordingly the energy of a future linear collider.

In view of these possibilities, the ILC is designed at a nominal energy of 500 GeV in the electron positron center-of-mass with symmetric momenta, while physics runs are possible above 90 GeV.

The machine can be upgraded up to $\sqrt{s} = 1\,\text{TeV}$. Several other options are also proposed like "GigaZ" which consists in running at the Z pole to produce about 10^9 Z bosons in less than a year. Other options of e^-e^- collisions or $e^-\gamma$ and $\gamma\gamma$ collisions (by using an intense laser beam near the IP) are foreseen.

1.4.2 Accelerator part

The expected luminosity of the ILC is of $500\,\text{fb}^{-1}$ at a center-of-mass energy of 500 GeV and in four years of running, while the design luminosity is $\mathcal{L} = 2{\times}10^{34} cm^{-2} s^{-1}$.

At high energies circular electron-positron machines become inefficient. Losses due to synchrotron radiation cannot be compensated anymore by reasonable means. The ILC is thus a 31 km-long linear electron-positron machine [BOW07] using superconductive accelerating cavities [PTW07].

The principal systems are schematized Fig. 1.3, with the parameters given Table 1.1.

- A photocathode DC gun generates bunch trains of polarized electrons. The polarization of the electrons is required to be greater than 80%. The electrons are accelerated up to 5 GeV and sent to the electron damping ring.
- The positrons are produced using already accelerated electrons. These electrons are extracted from the main linear accelerator (linac), deviated to an helical undulator and returned to the main linac with about 3 GeV lost, while high energy photons of approximately 10 MeV have been created and are targeted to create e^-e^+ pairs. The remaining photons and the created electrons are separated and then dumped. The positrons are accelerated to 5 GeV and enter their damping ring.
- Two damping rings with a circumference of 3.2 km will exist: one for electrons, one for positrons, where their spin is rotated perpendicular to the plane of the ring in order not to loose polarization. The aim is to reduce the transverse emittance of the bunches. Electrons and positrons need to be injected in the "ring to main linac" part of the accelerator without affecting the emittance and within the time between each train.
- Once electrons and positrons are extracted from the damping rings located near the center of the site, they need to be transported to the main linac. The ring to main linac system is thus used to inject the trains in the corresponding linac while rotating the spins to provide longitudinally polarized beams. It will also compress the bunch trains from several mm to a few hundred μm.

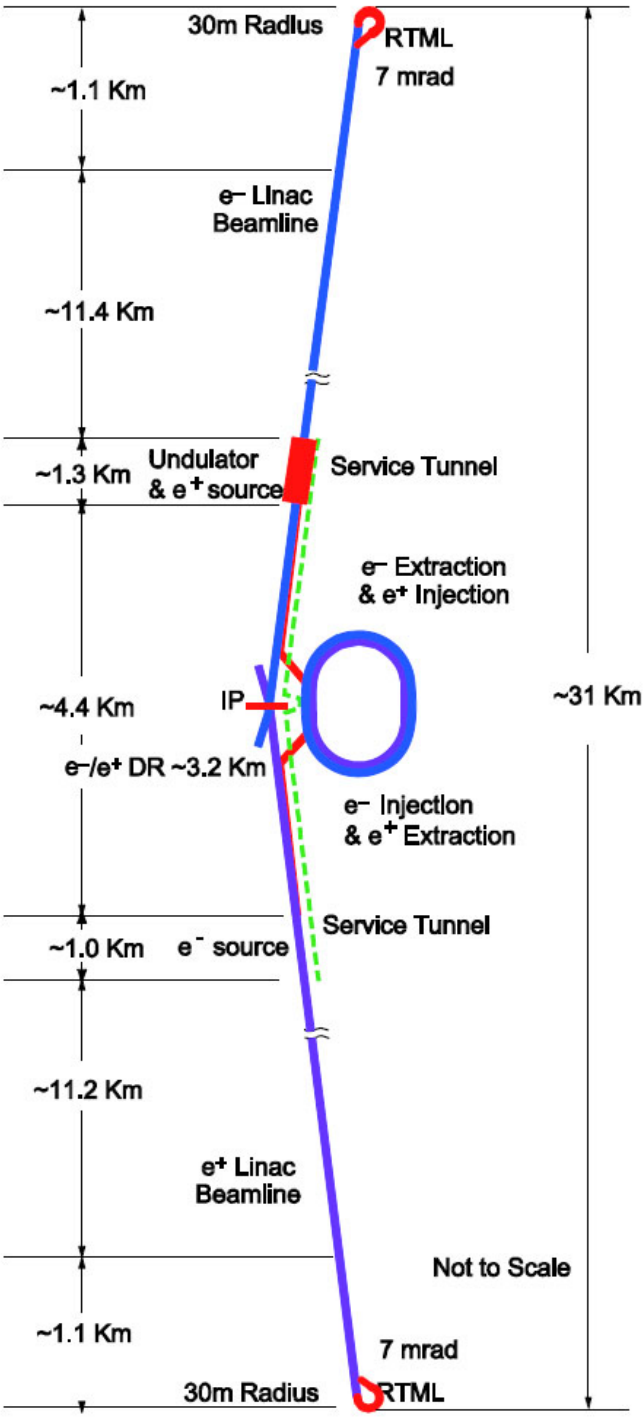

Figure 1.3: Layout of the ILC. Picture adapted from [E+11].

– The main linacs are 11 km long. The accelerating elements of the main linac are superconductive radio-frequency 1.3 GHz cavities, as recommended by the International Technology Recommendation Panel in August 2004 [ITR04], cooled down to 2 K. This is the primary cost driver of the project and an extensive and international R&D is made to produce these cavities. The basic element is a nine-cell 1.3 GHz niobium cavity, with an average accelerating gradient of 31.5 MV/m. To ensure this gradient for operations, a reproducible 35 MV/m gradient for these cavities must be demonstrated with a production yield greater than 90%. The beam spread must remain within approximately 0.1% at the interaction point (IP).
– Finally, the beams are collided with the beam delivery system (BDS). It is a 4.5 km-long system which focuses the beams at the IP to reach the designed luminosity with collisions at a 14 mrad crossing angle. In addition, it must extract the beams from the high energy linacs to protect the detectors. It should also provide means to monitor the beams before and after the interaction.

As for all previous colliders, there are strong motivations for having two detectors: competition and redundancy in the physics results, but also complementarity, in having different types of subdetectors. In addition, a failure of one of these very challenging detectors would not cause too long downtime. Two interaction zones had been envisaged by switching periodically the beams near the interaction region in two opposite points. But costs forced to keep only one IP. In an alternating fashion, two detectors will be moved into the interaction zone. To realize this push-pull scheme intensive engineering studies are ongoing [BOW07].

1.4.3 Measuring beam polarization

Polarization is important in several physics cases [MPAA$^+$08]. The polarimeters present in the baseline of the ILC should provide a 0.5% accuracy on the polarization of both beams before and after the IP but some processes even need it to be known with a better accuracy at the IP. To achieve this, a commonly used scheme is the "Blondel scheme" proposed in [Blo88]. The W pair production ($e^+e^- \to W^+W^-$) is expected to be used with a modified version of the Blondel scheme, as shown in [BEM09], to measure the polarization of the beams with a 0.2% precision. It requires to provide regular helicity-sign flip of the beams [MWS$^+$05].

Some improvements for the process $e^+e^- \to W^+W^-$ can be foreseen [Ric]. Its left-right polarization asymmetry is about 98.8% (see Table 8.1). Selecting small W polar angles ($\cos\theta > 0.7$), one reaches an almost 100% pure sample of left-handed W bosons ($A^0_{LR} \approx 100\%$, see [MPAA$^+$08] Fig.5.22), thus allowing to deduce the uncertainty on P_{eff} with 0.1% accuracy if only two configurations of polarization are used, those with opposite helicities of the beams. This could be valid even if the positrons are not polarised, as is the case in the baseline of the ILC.

Center-of-mass energy $\sqrt{s}$ (GeV)	200	230	250	350	500	upgrade 1,000
Collision rate f_{rep} (Hz)	5	5	5	5	5	4
Electron linac rate f_{linac} (Hz)	10	10	10	5	5	4
Number of bunches nb	1,312	1,312	1,312	1,312	1,312	2,625
Electron bunch population N- ($\times 10^{10}$)	2	2	2	2	2	2
Positron bunch population N+ ($\times 10^{10}$)	2	2	2	2	2	2
Main linac average gradient G_{av} (MV/m)	12.6	14.5	15.8	22.1	31.5	>31.5
RMS bunch length σ_{z} (mm)	0.3	0.3	0.3	0.3	0.3	0.3
Electron RMS energy spread $\Delta p/p$ (%)	0.22	0.22	0.22	0.22	0.21	0.11
Positron RMS energy spread $\Delta p/p$ (%)	0.17	0.15	0.14	0.1	0.07	0.04
Electron polarization P (%)	80	80	80	80	80	80
Positron polarization P' (%)	31	31	31	29	22	22
IP RMS horizontal beam size $\sigma_{\text{x}}*$ (nm)	904	843	700	662	474	554
(without traveling focus [Bal]) IP RMS vertical beam size $\sigma_{\text{y}}*$ (nm)	9.3	8.6	8.3	7	5.9	3.3
Luminosity $\mathcal{L} \times 10^{34}\, cm^{-2} s^{-1}$	0.47	0.54	0.71	0.86	1.49	2.7
Fraction of luminosity in top 1% $\mathcal{L}_{0.01}/\mathcal{L}$	92.20%	89.80%	84.10%	79.30%	62.50%	63.50%
Average energy loss δE_{BS}	0.61%	0.78%	1.23%	1.75%	4.30%	4.86%
(with traveling focus) IP RMS vertical beam size $\sigma_{\text{y}}*$ (nm)	6	5.6	5.3	4.5	3.8	2.7
Luminosity $\mathcal{L} \times 10^{34}\, cm^{-2} s^{-1}$	0.64	0.73	0.97	1.17	2.05	3.39
Fraction of luminosity in top 1% $\mathcal{L}_{0.01}/\mathcal{L}$	91.60%	89.00%	83.00%	77.90%	60.80%	62.30%
Average energy loss δE_{BS}	0.61%	0.79%	1.26%	1.78%	4.33%	4.85%

Table 1.1: Parameters of the ILC, as given in [E$^+$11]. The R&D is still ongoing and some figures may change.

Part I

Hadrons in a highly granular SiW ECAL

This part of the thesis presents an analysis of the interactions of hadrons in a highly segmented silicon-tungsten electromagnetic calorimeter (SiW ECAL). The purpose is twofold. On the one hand, the profound understanding of these interactions of hadrons is a key to improve existing algorithms of particle flow with hadrons, especially in the ECAL. On the other hand, the high granularity allows the verification and improvement in the modeling of hadronic showers by simulation programs as GEANT4. It also provides new insights into the structure of hadronic showers.

The principal interaction processes in matter acting in this study are presented in Chap. 2. The CALICE SiW ECAL and the setup of the test beams are then presented in Chap. 3 and 4. The focus of the study has been to develop an algorithm to find interactions of pions in the calorimeter at energies below 10 GeV and classify the events seen in different kinds. The classification of pion events is explained in Chap. 5. Finally, results in terms of the introduced classification are given Chap. 6, allowing for a better distinction between the hadronic models implemented in GEANT4.

Chapter 2

Interactions of particles in matter

Particle detection requires that the particle interacts with the material of the detector. In the following section, the principal interactions of particles in matter acting at the energies studied are presented. The energy losses are the result of the electromagnetic, strong and more rarely weak interactions with matter.

2.1 Electronic energy losses : the Bethe-Bloch equation, application to muons

When passing through matter, muons undergo mainly electromagnetic interactions with nuclei. These are of two kinds : multiple scattering when passing near atomic nuclei of the medium and ionization by energy transfer to the atomic electrons. This is true for all charged particles but at the energies studied here, other effects are negligible in the case of muons and will be discussed later.

The mean energy losses per unit of length $\langle -dE/dx \rangle$ of muons are shown Fig. 2.1. Several areas delimited by vertical bands which show boundaries between the relevant approximations used to describe these energy losses.

At the intermediate momenta studied here, i.e. ranging between 10 MeV and 100 GeV, the mean rate of energy loss is best described by the "Bethe-Bloch" equation (Eq. (27.3) in [Nak10], p285–287), i.e. the "Bethe" area of the figure. The Bethe-Bloch formula is valid in this momenta region where ionization processes are the dominant effects for energy losses of particles passing through matter.

- Starting from momenta p larger than 10 MeV, the energy losses decrease with an increasing momentum and reach a minimum, typically around a few GeV momentum. Particles with a momentum corresponding to this minimum are called "minimum ionizing particles" or "mips".
- Up to 100 GeV, muons primarily lose energy via the ionization processes modeled by the Bethe-Bloch formula or by δ-rays. δ-rays are secondary knock-on electrons resulting from a high energy transfer of the muon to an atomic electron.
- At higher energies, radiative effects become sizable. These effects will remain

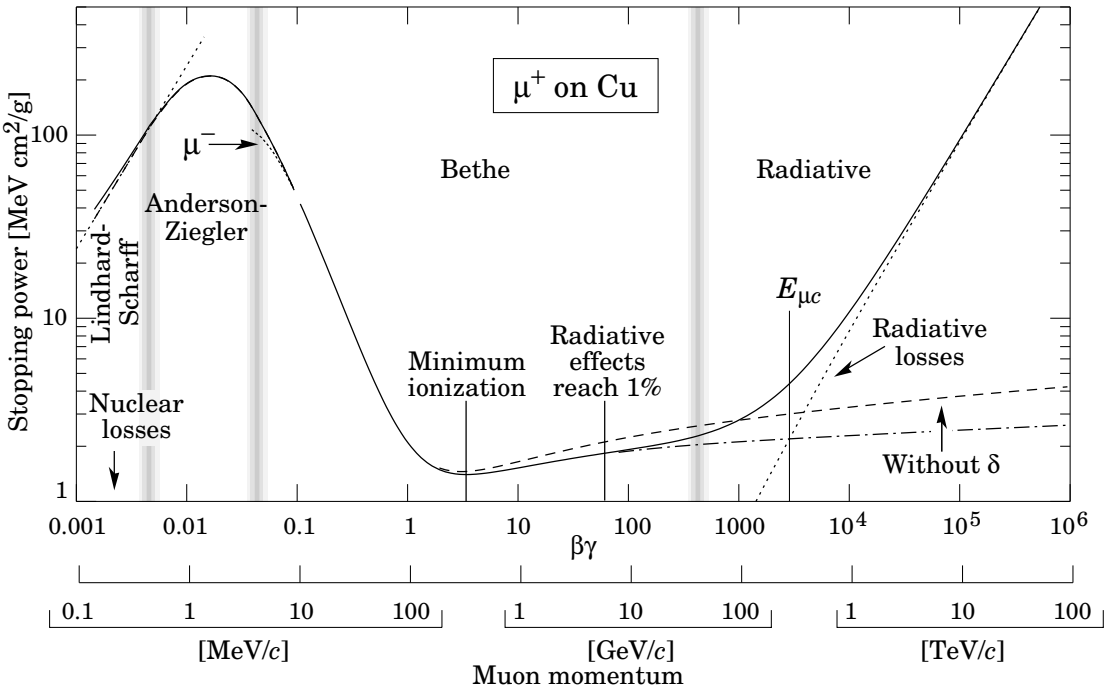

Figure 2.1: Stopping power ($= \langle -dE/dx \rangle$) for positive muons in copper as a function of the velocity β times the Lorentz factor γ ($\beta\gamma = p/Mc$) over nine orders of magnitude in momentum p. The part discussed in this text starts from several tenths of MeV up to tenths of GeV in muon momentum. Figure taken from [Nak10].

negligible for the muons studied here but are important for the electromagnetic cascades as discussed in the next section.

– In any case, charged particles which travel faster than the local speed of light loose energy by emitting Cherenkov radiation. The angle θ_C of the emitted Cherenkov light with respect to the momentum of the particle (of velocity β) is given by $\cos\theta_C = 1/\beta n$ where n is the refractive index of the medium.

2.2 Electromagnetic cascades

As electrons at energies above 100 MeV are already ultra-relativistic they loose their energy mainly in bremsstrahlung, i.e. photon radiation when passing near an atomic nucleus.

Most of the cases studied in this thesis will show electrons with energies well above 100 MeV, so that these radiative losses dominate the losses by ionization. The characteristic amount of matter traversed in these cases is the radiation length X_0, defined by the mean distance after which a high energetic electron has a fraction $1/e$ of its initial energy (or mean free path of the electron). This constant is a characteristic of the material considered. Some indicative values are given Table 2.1.

In addition, positrons are affected by e^+e^- pair annihilation with atomic electrons into pairs of photons.

Photons lose their energy by three means : at small energies $E \ll 1\,\text{MeV}$ via the photoelectric effect, at $E \sim 1\,\text{MeV}$ via Compton scattering and at higher energies via e^+e^- pair production. The typical mean free path for pair production for a high energy photon is given by $\frac{9}{7}X_0$.

These reactions involving electrons, photons and positrons, combined together lead to an electromagnetic cascade called electromagnetic shower. The energy losses for electromagnetic particles passing through matter arise typically over the radiation length X_0 such that $dE/dx \sim -E/X_0$. Thus a block of matter with a depth of several radiation length contains almost all of the electromagnetic shower.

To describe the transverse size of a shower, the Molière radius R_M is often used. It is proportional to X_0 and represents, on average the radius of a cylinder containing 90% of the electromagnetic shower. Some indicative values are given Table 2.1.

2.3 Hadronic showers

Hadrons undergo strong interactions too. A charged hadron will ionize the traversed medium like a muon until it undergoes nuclear reactions. These reactions are numerous : from elastic scattering to inelastic scattering with complex final states. Neutral hadrons will not ionize the medium and the energy losses can only happen through nuclear reactions.

In general, particles produced in a hadronic interaction can also decay via the electromagnetic interaction, especially π^0s ans ηs which decay into two photons. The energy deposited in a hadronic shower thus always carries an electromagnetic fraction. The rest of the deposited energy comes from nuclear reactions such as nuclear spallation reactions. Some of this energy is unmeasurable, like the nuclear binding energy needed to release nucleons during a spallation reaction. The large event-to-event fluctuations due to the variety of nuclear processes involved renders the measurement of hadronic energy deposited in showers less precise than with electromagnetic showers.

The mean free path of a hadron between two nuclear interactions is the nuclear interaction length λ_{int}. Typical values of λ_{int} are shown Table 2.1.

Material	$X_0\,(cm)$	$R_M\,(cm)$	$\lambda_{\text{int}}\,(cm)$
Air (dry, 1 atm)	30390	7330	74770
Iron (Fe)	1.757	1.729	16.77
Tungsten (W)	0.35	0.9327	9.946
Lead (Pb)	0.56	1.602	17.59

Table 2.1: Radiation lengths, Molière radii and interaction lengths for several materials. Figures taken from `http://pdg.lbl.gov/2010/AtomicNuclearProperties/`.

2.4 Simulations of hadronic showers

Due to the complicated nature of hadronic interactions a precise description of hadronic showers in simulations is difficult to achieve. Several models called physics lists are proposed in the GEANT4 simulation toolkit to implement the hadronic interactions [G4l]. Some models provide a description of the intra-nuclear cascade, others describe the low energy or high energy formation of strings in the initial collision with the nucleus and others handle the de-excitation of the remnant nucleus. Thus, there exists combinations of the models briefly described below.

- The Bertini cascade model simulates the intra-nuclear cascade. The incident hadrons collide with protons and neutrons in the target nucleus and produce secondaries which in turn collide with other nucleons. The target nucleus is treated as an average nuclear medium and final states appear according to the free-particle cross-section data with the nucleus being then decayed.
- The Binary cascade model simulates the intra-nuclear cascade too. The nucleus is treated as a collection of nucleons rather than an averaged medium. The propagation of the incident hadron and secondaries is modeled by a cascading series of two-particle collisions. Secondaries are created during the decay of resonances produced by the collisions.
- The Quark-Gluon-String (QGS) model handles the formation of strings for the collision of the initial hadron in the nucleus which are then fragmented using the Quark-Gluon String fragmentation model.
- The Fritiof model handles the formation of strings for the collision of the initial hadron in the nucleus which are then fragmented, like QGS does. The Lund fragmentation model is here used for string fragmentation.
- The Precompound model generates the final state for the hadron inelastic scattering. It provides the smooth transition from reactions in the previous models to equilibrium via de-excitation. It is thus used in combination with other models describing the intra-nuclear cascade.
- There exist also Low Energy and High Energy Parametrized models (LEP,HEP) which parametrize the mean number of hadrons produced in the hadron-nucleus collision to produce secondaries.

Chapter 3

R&D toward highly granular calorimeters

3.1 Design of a highly granular ECAL

The CALICE collaboration designs and studies electromagnetic and hadronic calorimeters (ECAL, HCAL) for experiments at the ILC. For an ILC detector, they should lead to reconstruction of every particles in jets (see details Part II) as well as be compact as possible to reduce the cost of the surrounding magnet.

To reconstruct particles in a jet, calorimeters need to be able to separate among their energy depositions. A crucial quantity for an ECAL is thus the Molière radius R_{M} which should be minimum and combined with high lateral granularity, to allow a better separation between clusters of deposited energy for each particle entering the calorimeter.

To have a small longitudinal size of the ECAL, its material needs to be have a small radiation length, to fully contain in a small area the showers initiated by electrons and photons. According to Table 2.1, one of the best materials to achieve these goals is tungsten (W). A physics prototype of silicon-tungsten (SiW) ECAL was designed and commissioned [RYH$^+$08] and tested under beams of single particles to validate this choice.

3.2 The SiW ECAL prototype

The SiW ECAL features a sandwich structure comprising 30 layers of silicon (Si) as active material, alternated with tungsten (W) as absorber material [RYH$^+$08].

The active layers are made of Si wafers segmented in 1×1 cm^2 pixels (or pads). As shown in Fig. 3.1, each wafer consists of a square of 6×6 pixels and each layer is a matrix of 3×3 of these wafers resulting in an active zone of 18×18 cm^2 with in total 9720 channels.

The ECAL is divided in 3 modules of 10 layers. The W depth per layer is different in

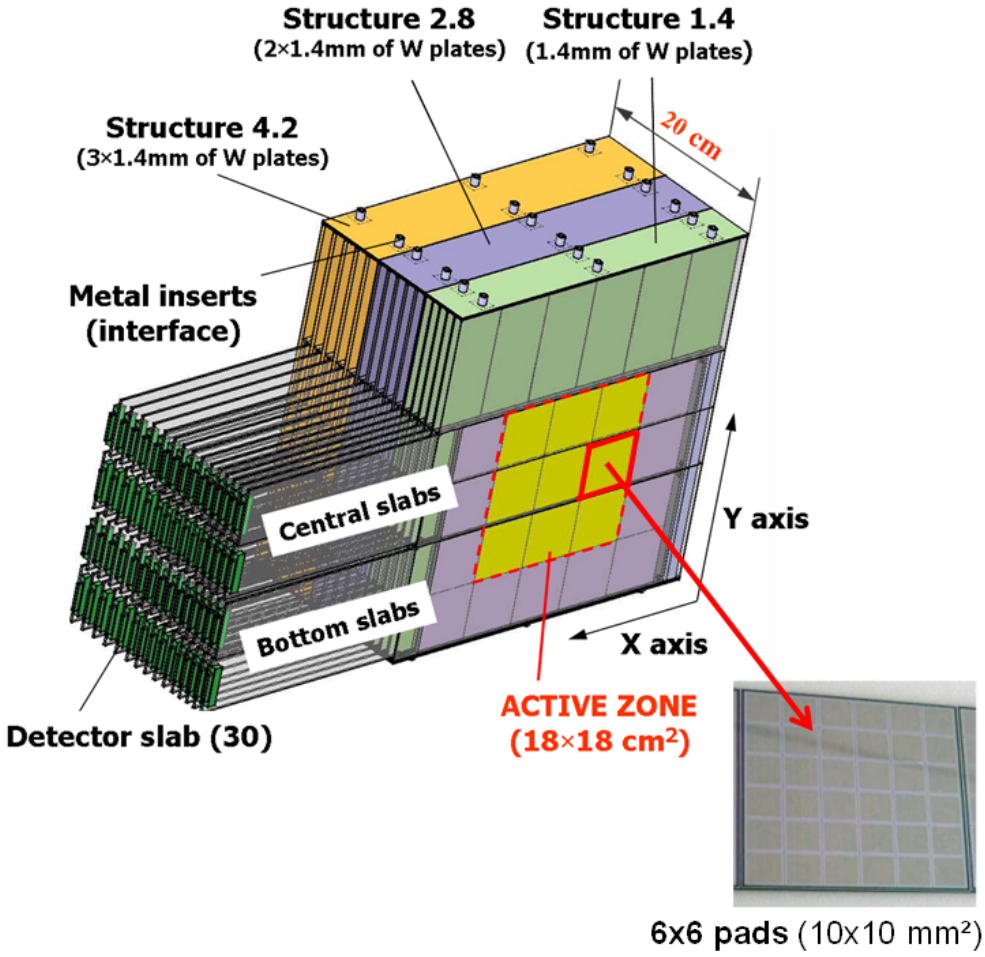

Figure 3.1: Schematic view of the SiW ECAL prototype. Pictures combined from [C+09]

each module increasing from 1.4 mm (0.4 X_0) in the first one, to 2.8 mm in the second and 4.2 mm in the last one. This corresponds to 24.6 X_0, around 1.0 λ_{int}, which ensures that more than half of the hadrons will have a primary interaction in the ECAL.

The Si wafers are held by a printed circuit board (PCB). As shown Fig. 3.2, the PCBs are mounted two by two in an elementary detection unit (slab). The Si wafers are located on each side of a H-shaped tungsten supporting structure. These slabs are shielded by aluminum foils and inserted in the mechanical W structure (Fig. 3.1). From this arrangement, it follows that two successive layers of Si are either separated only by one W layer or by one W layer and two PCBs with their corresponding shielding. The amount of material seen by a particle passing through several layers will differ whether it is an odd or an even layer. This will be referred to as the odd-even effect and it will be shown on the results.

Note that an upper "central" and a lower "bottom" slab are needed to instrument the

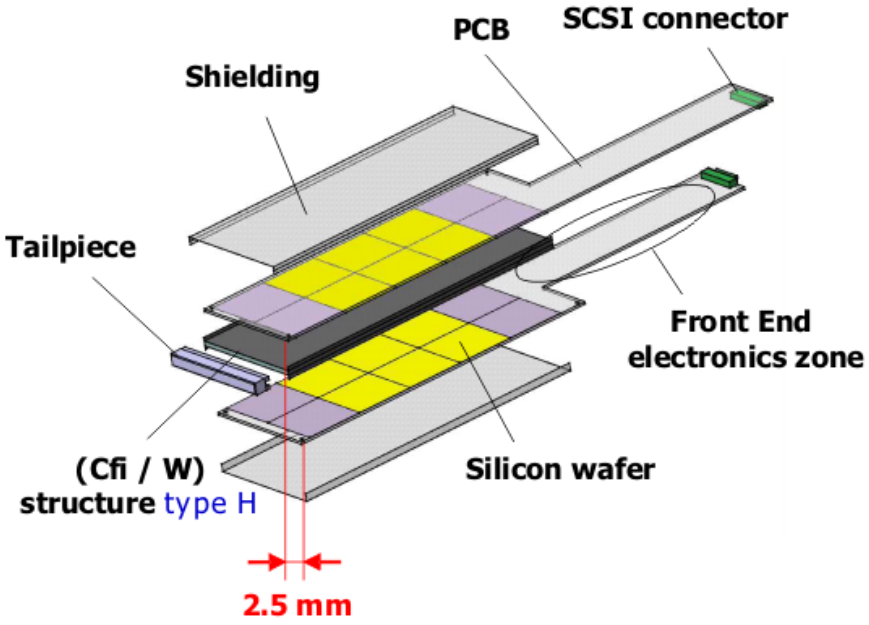

(a) Schematic view of a slab.

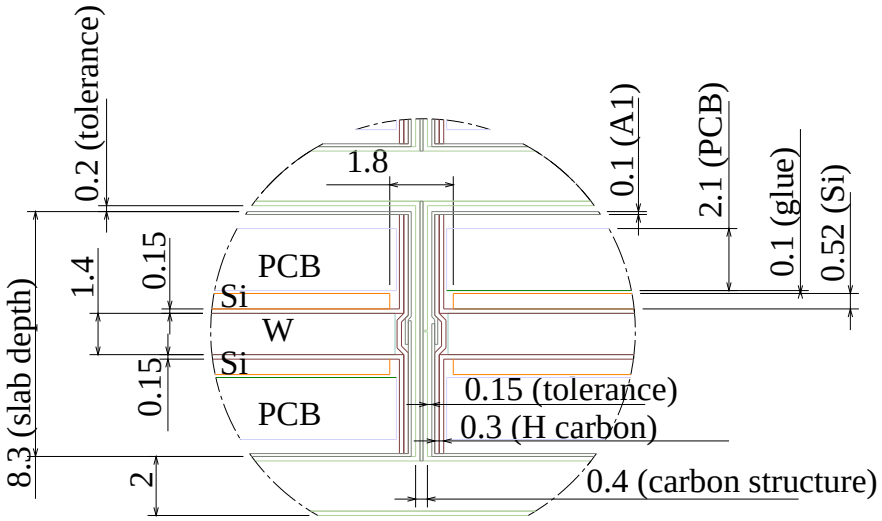

(b) Detailed transverse view of a slab. One passive tungsten layer is sandwiched between two active silicon layers. The upper silicon layer is preceded by a large amount of passive material (glue, the PCB, aluminum, the carbon structure as well as a tungsten layer), the lower one only by one tungsten layer. Dimensions are in mm.

Figure 3.2: Pictures of a detector unit (slab) used in the SiW ECAL, taken from [RYH+08, AKR+09]

matrix of 3 × 3 wafers in a layer (see Fig. 3.1).

In addition, each detection layer is translated in one direction from one slab to another, as shown Fig. 3.3. This staggering between slabs permits to reduce overlapping passive areas. These passive areas occur because of guard rings surrounding each silicon wafer in addition to the larger passive area located between the central and bottom slabs.

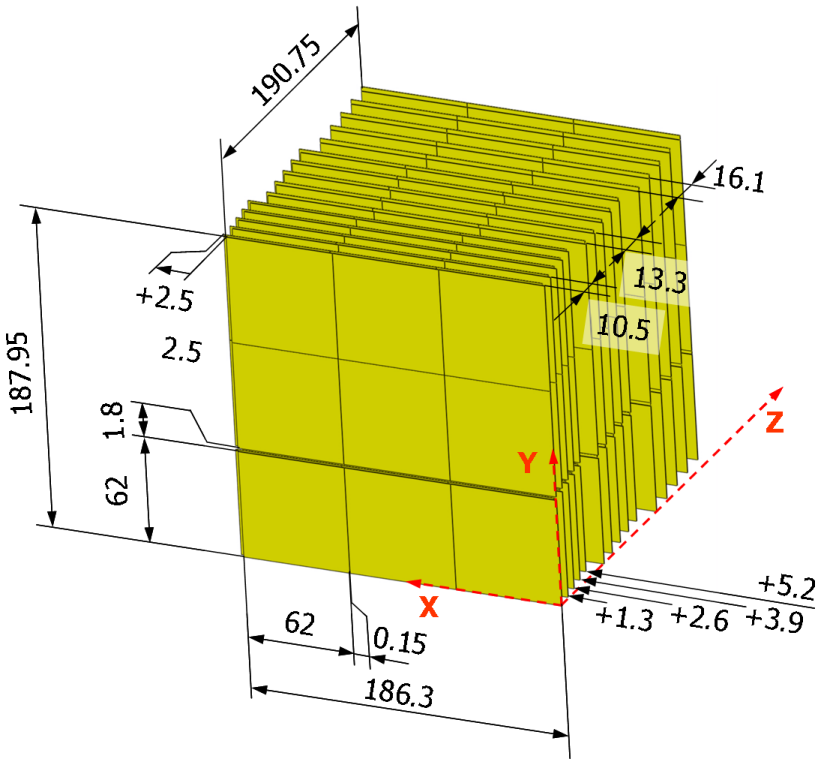

Figure 3.3: Details of passive areas and layer offsets (staggering) between silicon layers. Offsets are indicated with single-headed arrows. Distances are in mm. Picture taken from [RYH+08]

Using data collected with electron beams with energies ranging from 6 GeV to 45 GeV, the linearity and resolution of this calorimeter to electrons were estimated [AKR+09]. The linearity is better than 1% while the relative energy resolution is estimated to be $\sigma_E/E = (16.53 \pm 0.14(\text{stat}) \pm 0.4(\text{syst}))/\sqrt{E(\text{GeV})} \oplus (1.07 \pm 0.07(\text{stat}) \pm 0.1(\text{syst}))$ (%).

3.3 An example of hadrons in jets

Typical energies of hadrons, especially charged pions in a top pair event start at around 1 GeV until 100 GeV, as pictured Fig. 3.4.

On average, 40 pions of energy larger than 1 GeV can be found per top pair event,

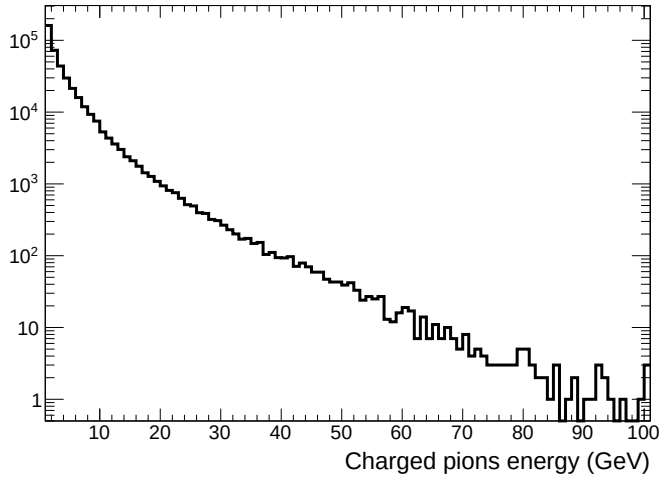

Figure 3.4: Distribution of the energy of charged pions, with an energy above 1 GeV, produced in generating 10000 $t\bar{t}$ events. More than 90% of these pions have an energy below 10 GeV.

out of which 90% have an energy smaller than 10 GeV. In order for the calorimeters to support actively the energy measurements, it is important to investigate and understand the behavior of such hadrons.

Chapter 4

Analysis of test beam data

4.1 Description of the beam line

Test beams were conducted in May and July 2008 at the Fermilab Test Beam Facility [FTB] at FNAL which provides a beam of particles ($e^{\pm}$, p, μ^{-}, $\pi^{\pm}$) at energies ranging from 1 GeV to 120 GeV. The ECAL was placed in front of the other CALICE prototypes: an analogue HCAL and a TailCatcher (TCMT) [AKR+10a].

The scheme of this setup is shown Fig. 4.1. The coordinate system is right handed with the z axis pointing in the direction of the beam.

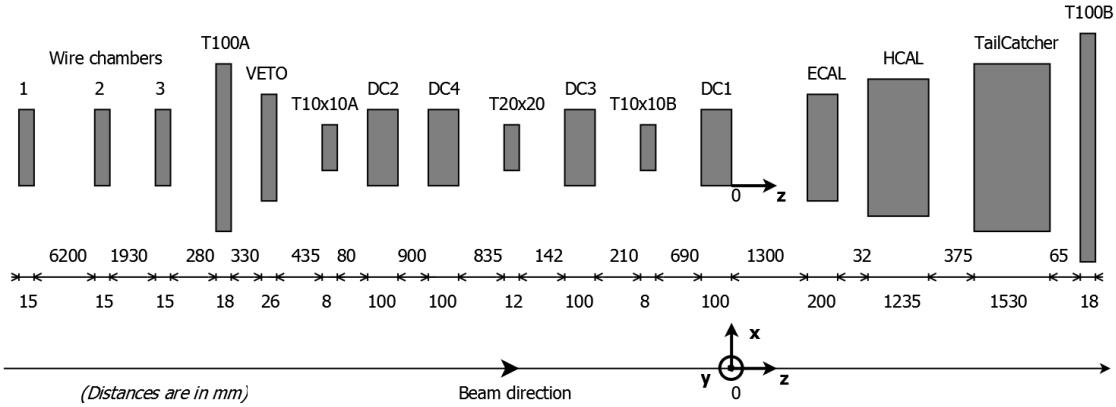

Figure 4.1: The beam line at FNAL. Distances are in mm.

The primary beam consists of high energy protons of 120 GeV. It is targeted to create the secondary particles. Magnets and collimators are used to select the desired momentum and reduce the momentum spread of the beam. At this point, the beam is a mixture of secondaries with the selected momentum. Pure event samples require to select and identify correctly single particles entering the detectors.

For this purpose, the beam line is instrumented with a Cherenkov detector used to identify particles. It is a gaseous detector which collects Cherenkov light emitted by particles passing through it. By adjusting the pressure, one varies the refractive index

of the gas, thus particles of a given velocity β are identified (recall that the angle θ_C of the emitted Cherenkov light is given by $\cos\theta_C = 1/\beta n$). Since the momentum is already known, the mass and identity of the particle is deduced.

The transverse beam spread can lead to particles not hitting the targeted detectors. To ensure that the particle will enter the detector, after what the event will be recorded, scintillators were used to reject particles and to trigger events.

Wire chambers and drift chambers are also part of the beam line. They are used in combination to extrapolate precisely the path of the particle entering the detectors. This information was not available when this analysis was conducted, what forces to use the ECAL as a tracker for entering particles, as it will be shown in 4.3.2.

The analyzed data consists of runs with π^-. Events are triggered using the scintillator counters and electron contamination is reduced by using the Cherenkov detector. The energies of the primary particles are 2, 4, 6, 8 and 10 GeV. Higher energies were studied in [AKR$^+$10b] with an overlap at 8 and 10 GeV with the study presented here.

4.2 Simulation with various GEANT4 physics lists

Due to the complicated nature of hadronic interactions a precise description of hadronic showers in simulations is difficult to realize. Several models called physics lists are proposed and the high granularity of the SiW ECAL offers unprecedented means to discriminate among them. To compare the test beam data with these models, Monte Carlo simulations were done within the MOKKA framework [Mok] which provides the geometry interface to GEANT4 [Gea, AAA$^+$03]. The physics lists used are briefly reviewed here (for more details, see [G4l, AAA$^+$06] and [UAF$^+$09]).

- QGSP_BERT: combines the Bertini model BERT at low energies, making a transition to the Low Energy Parametrized model (LEP) between 9.5 GeV and 9.9 GeV and a further one at energies between 12 and 25 GeV, to the Quark-Gluon-String Precompound model (QGSP). It is used for LHC calorimeters and will be used as reference for this study.
- QGS_BIC: the Binary cascade model (BIC) is used at low energies below 1.2 GeV and for re-scattering of secondaries, then LEP in the intermediate region until 12 GeV and QGS at higher energies.
- QGSP_BIC: uses the BIC model but not for pions for which LEP is used and without re-scattering of secondaries, then LEP below 12 GeV and QGSP above are used.
- LHEP: combines the physics lists LEP below 55 GeV and HEP above 25 GeV, the transition region being thus 25 GeV to 55 GeV.
- FTFP_BERT: uses BERT below 5 GeV and the Fritiof model FTFP above 4 GeV.

The validity regions for the subcomponents of the introduced models are summarized in Table 4.1.

The CALICE software [Cal] (v02-00) was used for both, data reconstruction and digitization. This comprises the GEANT4 version 9.3 used for simulations. The starting point of a primary particle is positioned 160 m upstream of the ECAL surface.

E (GeV)	2	4	6	8	10
QGSP_BERT	BERT				BERT + LEP
QGS_BIC	LEP + BIC (secondaries)				
QGSP_BIC	LEP				
LHEP	LEP				
FTFP_BERT	BERT	FTFP			

Table 4.1: Model used for hadronic interactions depending on the physics list and energy of the interacting particle.

4.3 Event selection

The cells of the ECAL have been already calibrated in units of MIP. [1] This represents the equivalent charge collected by the Si pads when a minimum ionizing particle passes through it and deposits the energy corresponding to the minimum of ionization.

A pure sample of single pions is needed for the precise comparison of test beam data and their Monte Carlo simulations. To select good events, the following steps are applied in this order.

- A threshold of 0.6 MIP is chosen to remove noisy hits. This corresponds to three times the noise level, thus not harming the physical results.
- A hit is called isolated if all of the 26 cells in the surrounding cube are empty. Isolated hits are discarded.
- The total number of hits in the ECAL is required to be at least 25 to remove particles which hit the ECAL at a large angle, and which would thus create signals outside the detection acceptance.
- The barycenters $\bar{x}$ and $\bar{y}$ of the hits are calculated:

$$\bar{x} = \frac{\sum_{\text{hits}} x_{\text{hit}}\, E_{\text{hit}}}{\sum_{\text{hits}} E_{\text{hit}}} \text{ and } \bar{y} = \frac{\sum_{\text{hits}} y_{\text{hit}}\, E_{\text{hit}}}{\sum_{\text{hits}} E_{\text{hit}}} \tag{4.1}$$

  Requirements are -50 mm $< \bar{x} <$ 50 mm and -50 mm $< \bar{y} <$ 50 mm to reduce lateral shower leakage.
- In some events, the wafer in the middle of the bottom part in the 29th layer is showing more than 8 hits whereas no activity is seen around. It is a known problem and the solution adopted here is to remove these events. A fraction of 0.3% of the events suffer also from noise in other layers even after offline corrections. These events are discarded as well.
- Pions are selected using the Cherenkov counters.

1. Note: the unit "MIP" is written in capital letters while a minimum ionizing particle is written "mip".

Despite these event selections, there are still impurities, for example muons, which are treated in a second step. Contamination from electrons however is found to be smaller than 1% at 2 GeV and negligible at other energies, according to a Monte Carlo study.

4.3.1 Muon rejection

Muons, which velocity is rather close to the pion one for a given momentum, may still contaminate the selected sample of events.

The pion selection using Cherenkov counters is refined by counting the number of hits in ECAL, HCAL and TCMT to reduce this muon contamination. Using a Monte Carlo sample of muons, the following cuts on these numbers derived from Fig. 4.2 are chosen for muon rejection.

$$N_{\mathrm{ECAL}} < 50 \ , \ 30 < N_{\mathrm{HCAL}} < 70 \ , \ 10 < N_{\mathrm{TCMT}} < 35 \tag{4.2}$$

If an event passes these requirements, it is regarded as a muon, thus rejected.

Using these muon simulations and pion simulations, the rates of remaining muons and rejected pions after the selection are summarized in Table 4.2. At 2 GeV, the total energy loss being about 1.4 GeV in the ECAL and HCAL, the muons give fewer counts in the TCMT. The conditions need to be slightly changed to match these fewer counts with $N_{\mathrm{TCMT}} > 5$. This change is taken into account in Table 4.2 and in the following study. Using these cuts on the data, the initial contamination from muons in the beam is deduced and shown too, assuming that the particles selected at this stage consist only of muons and pions.

E (GeV)	2	4	6	8	10
Remaining muons (%)	2.0	0.4	0.4	0.5	1.0
Rejected pions (%)	8.7	3.0	2.7	2.3	0.9
Initial muon contamination (%)	12.6	4.2	2.3	0.9	1.9

Table 4.2: Rates of remaining muons and rejected pions with cuts on muons. (Simulation study) The cuts against muons were applied to the data to deduce the initial rate of muons in the beam.

4.3.2 Multiple particles

During the data taking period, events with several particles entering the ECAL were seen, despite the selections applied. To prevent effects of multiple particles entering the ECAL, an algorithm of track finding was developed. This algorithm is used to count the number of particles entering the ECAL and select events with only one.

To count the number of entering tracks, the hits in the six first layers of the ECAL are used. Clusters of nearby hits are created and fit with straight lines. One particle is defined by a cluster of at least 3 cells.

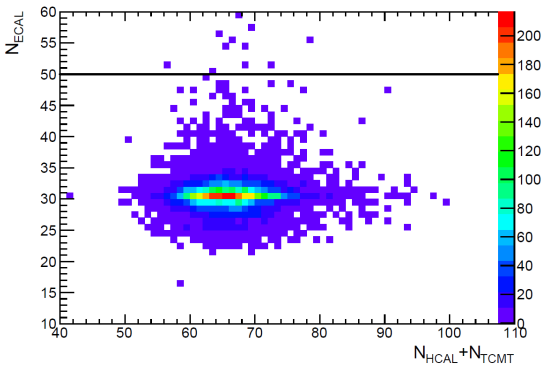

(a) Histogram showing the number of hits in the ECAL versus the total number of hits in the HCAL and TCMT for events of 10 GeV muons.

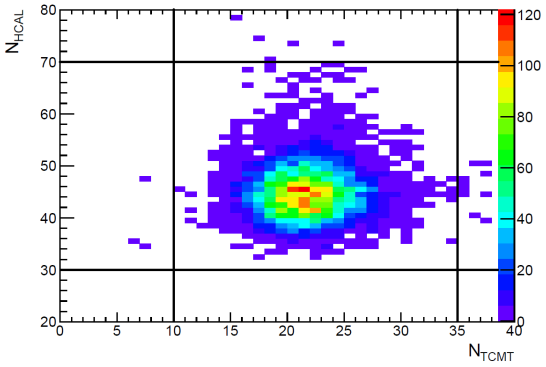

(b) Histogram showing the number of hits in the HCAL versus the number of hits in the TCMT for simulated events of 10 GeV muons.

Figure 4.2: Histograms of the number of hits found in the three calorimeters for events with 10 GeV simulated muons, with the corresponding cuts indicated. The cuts for muons are then deduced. They are chosen to be energy independent, apart from 2 GeV where a small change is needed.

The algorithm introduces a distance criterion d_{th} which is calculated from the three dimensional distance of cells carrying a signal. For a given distance $d < d_{th}$ cells are merged into a cluster. Otherwise they seed a new cluster. For this study the algorithm is applied to the first six layers to identify particles entering the SiW ECAL and avoid regions where the signals created by the particles merge due to their interaction in the calorimeter volume. Finally, the algorithm only accepts clusters with more than three hits. The separation power and hence the optimal value of d_{th} depends on the actual cell size but also of the shifts introduced by the staggering of the calorimeter layers.

The value of d_{th} is optimized with the help of a simulation study. For this in each

case two muons of 10 GeV from simulated beams incident on the SiW ECAL surface with a width of $\sigma_x = 7.4\,\text{mm}$ in x-direction and of $\sigma_y = 4.5\,\text{mm}$ in y-direction are randomly overlaid. The result is shown in Fig. 4.3. For a value of $d_{th} = 12\,\text{mm}$, 80% of the muons can be successfully separated. Toward larger values, hits from different particles are merged into the same clusters. Therefore the separation power decreases. The sharp drop off toward smaller values of d_{th} is consistent with the lateral cell size of $1 \times 1\ \text{cm}^2$. In the following the value of $d_{th} = 12\,\text{mm}$ is chosen to identify single particle events.

This method is used to define the primary track in the ECAL (see Sec. 5.1).

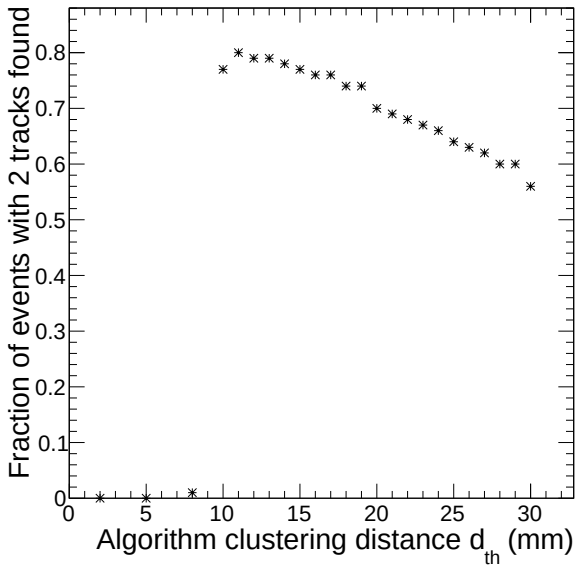

Figure 4.3: Efficiency to separate two randomly overlaid 10 GeV muon tracks. It is shown for different separation distances allowed between two hits d_{th}, below which they are merged into a single cluster.

4.3.3 Selected events

After these selection criteria are applied, the remaining number of measured events is given Table 4.3. The numbers at all energies ensure small statistical fluctuations.

E (GeV)	2	4	6	8	10
Events	10925	79296	52396	147876	346148

Table 4.3: Number of events remaining after all the selection criteria are applied to the data.

As a by-product of the selection, an estimate of the number of particles entering the

ECAL can be deduced and is shown Fig. 4.4.

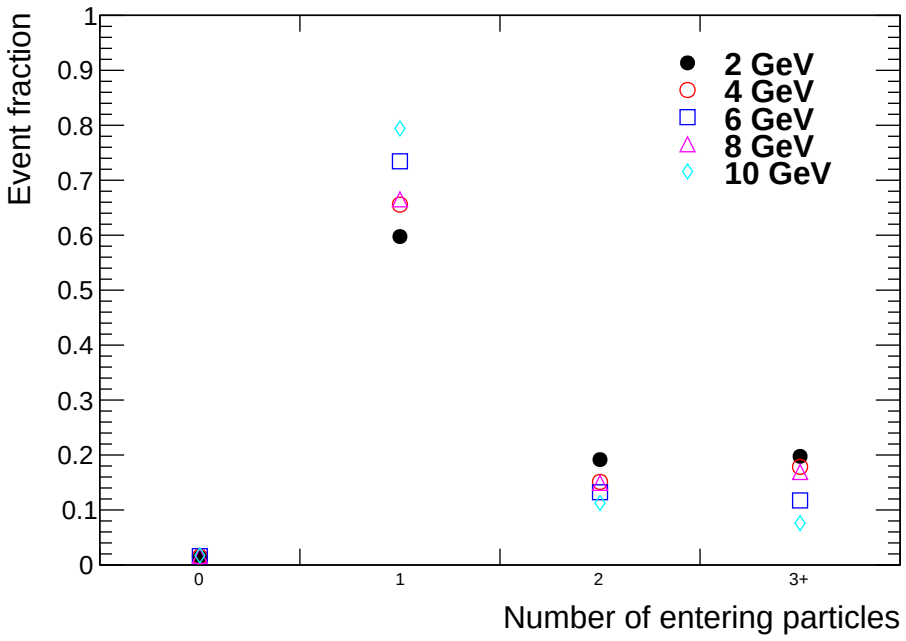

Figure 4.4: Number of entering particles in the ECAL at the beam energies of 2, 4, 6, 8 and 10 GeV, after selection criteria are applied.

Chapter 5

Classification of hadronic events

The destiny of a primary particle impinging on the SiW ECAL can be twofold. Either the particle passes the ECAL as an ionizing particle or it undergoes interactions which lead to the creation of secondary particles. The latter case is illustrated in Fig. 5.1. This figure suggests that each event may be subdivided into three parts. First there is a primary track in the beginning of the ECAL. Second, the interaction occurs. Third, secondaries emerge from the interaction region.

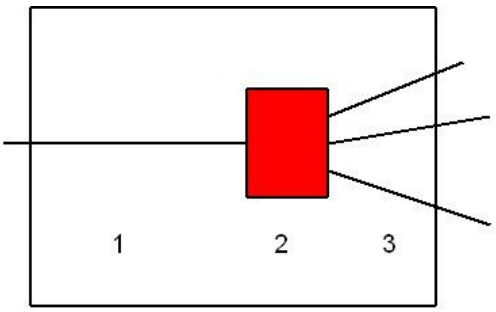

Figure 5.1: Generic picture of a typical hadronic interaction. 1: a primary track. 2: area of interaction. 3: secondaries emerge from the interaction zone.

The method mentioned Sec. 4.3.2 to find tracks entering the ECAL is employed to define the position and direction of the primary track. The next step is to find the start of the shower when an interaction occurs.

An algorithm is developed in order to find the interaction layer of pions in the SiW ECAL at the energies of this study. The following section describes the procedure it follows. In a next step (Sec. 5.2), four types of events are classified thanks to the granularity of the ECAL. The optimization of the algorithm is presented in Sec. 5.3, after what the efficiency to find an interaction is found to be of 62% at 2 GeV and up to 83% at 10 GeV.

5.1 Finding an interaction in the ECAL

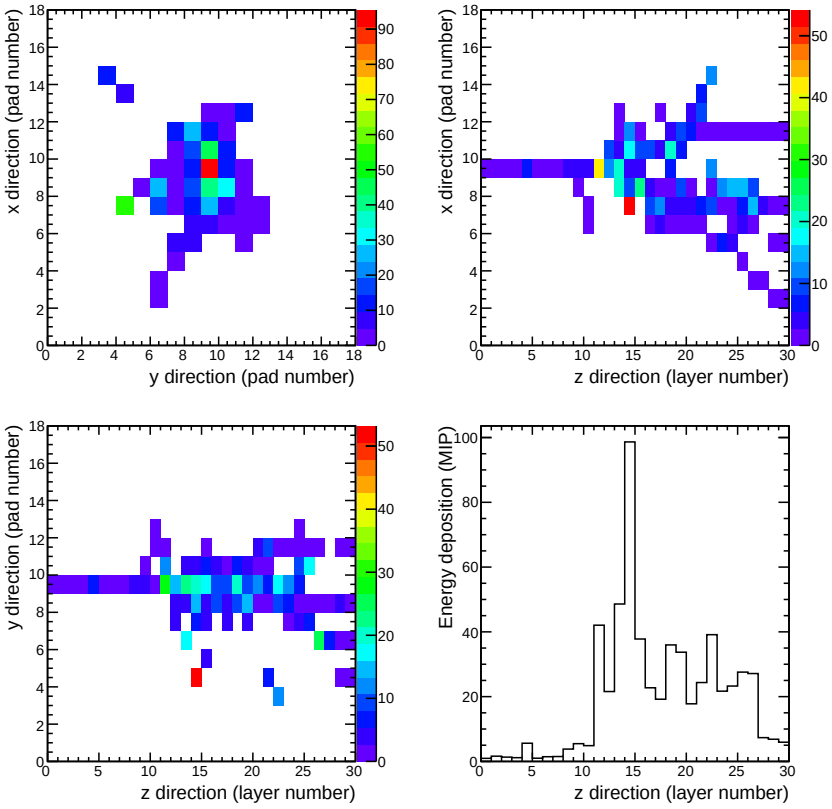

Figure 5.2: Display of a hadronic interaction in a test beam event for a pion with an incident kinetic energy of 10 GeV. These are 2D energy weighted profiles of a hadronic interaction in the ECAL: the window on the top left is a projection in the x-y plane of the energy deposited, the one on the top right is the very same projection on the x-z plane and the one on the bottom left is for the y-z plane. The bottom right histogram shows the energy deposition in each layer. Units are cell index in x and y and layer number in z. All start from 0. The energy unit is in MIP.

A typical event featuring a large number of secondaries is displayed in Fig. 5.2. The longitudinal profile can be seen in the bottom right histogram. The deposited energy is significantly increasing, layer 11. This layer is obviously the interaction layer. This is also supported by the lateral view of the event as shown on the other parts of Fig. 5.2. This condition of interaction can be written:

$$E_i > \text{Ecut and } E_{i+1} > \text{Ecut and } E_{i+2} > \text{Ecut (MIP)} \tag{5.1}$$

where E_i is the energy deposited in layer i (in MIP). That is, a cut (Ecut) is applied on the deposited energy in each layer. If three consecutive layers have an energy higher

than this fixed Ecut, the interaction layer is the first of these (layer i). This interaction reflects inelastic scattering of pions in the tungsten absorber.

However this simple cut is not sufficient to find all interactions. Particularly at small hadron energies e.g. 2 GeV, shower fluctuations are expected to be strong and a large fraction of non-interacting events may be accepted if Ecut is chosen to be too small. On the other hand, interactions may be missed for too high values of Ecut. In order to account for fluctuations in the energy deposition, the two new variables F and F' are introduced. They are defined by:

$$F = \frac{E_i + E_{i+1}}{E_{i-1} + E_{i-2}} \quad \text{and} \quad F' = \frac{E_{i+1} + E_{i+2}}{E_{i-1} + E_{i-2}} \tag{5.2}$$

They measure a relative increase of energy deposition after a given layer i and the following $i+1$. The fact that two consecutive layers are grouped together makes the variables less sensitive to fluctuations in the energy deposition when identifying interacting events.

A new threshold value Fcut is proposed. If both, F and F', fulfill the condition:

$$F > \text{Fcut and } F' > \text{Fcut} \tag{5.3}$$

the energy deposition is not considered mip-like anymore and layer i is defined to be the interaction layer. The recognition of interacting events benefits from this other criterion. This is confirmed in Table 5.1. It shows the fraction of interacting events found by using criterion 5.1 only with Ecut = 10 MIPs, and the fraction added when refining the selection using F and F' with Fcut=4.

E (GeV)	f_E (Ecut = 10 MIPs)	$f_{F/E}$ (Fcut = 4)
2	14.3%	26.0%
4	39.6%	20.9%
6	57.9%	15.2%
8	69.1%	11.9%
10	72%	14.9%

Table 5.1: Table showing the fraction of interacting events found by using criterion 5.1 (f_E) and those added by using criterion 5.3 ($f_{F/E}$).

Among the events found using 5.3, new topologies leading to a smaller number of secondaries appear, such as the example shown Fig. 5.3. This event features a local increase of energy. This event would have been rejected by Eq. 5.1. It is recovered by the refinement of the analysis using the introduced variables F and F'. The frequency of this type of events with respect to others will be discussed further down.

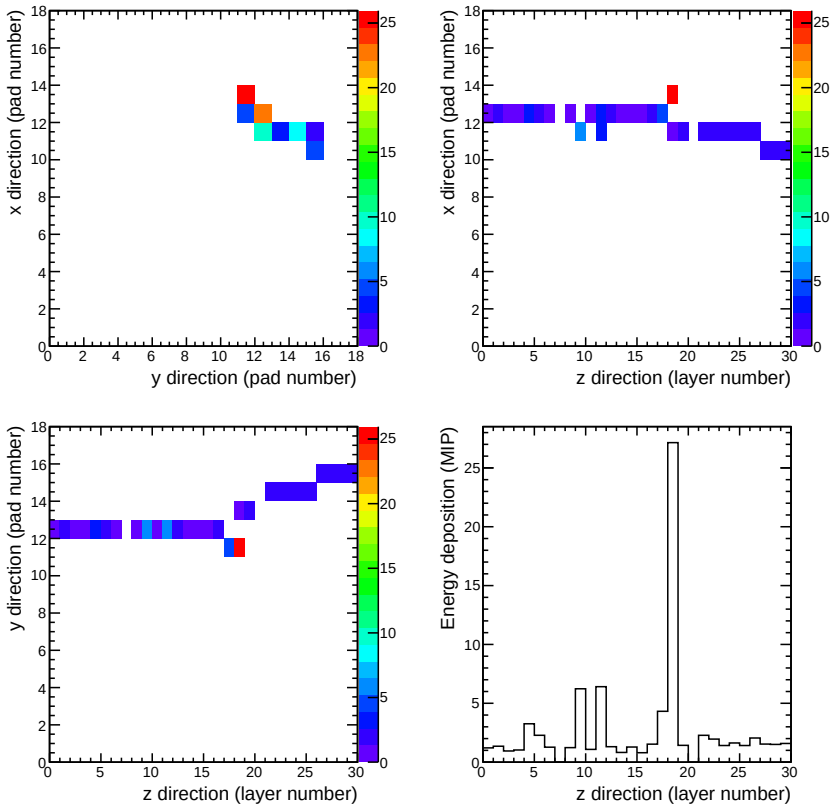

Figure 5.3: Display of a hadronic interaction in the ECAL for a pion with an incident kinetic energy of 2 GeV (test beam event).

5.2 Classification of the interactions

The algorithm to find interactions in the ECAL has been defined and uses two criteria. As pointed out before, different types of interactions are visible, depending on the criteria used. Four kinds of events are proposed.

The interactions passing Eq. 5.1 will be called "FireBall". These interactions are typically inelastic hadronic interactions followed by an internuclear cascade. In the case of other events passing Eq. 5.3, there are two possibilities.

– The relative increase might continue which is defined by:

$$\frac{E_{i+2} + E_{i+3}}{E_{i-1} + E_{i-2}} > \text{Fcut} \tag{5.4}$$

One has to make sure that this increase is not an artifact caused by a backscattered particle. In this latter case, the relative increase of energy would be caused by the presence of this particle, whose track is several cells away from the primary track. To make sure that the increase is really caused by the start of an hadronic

interaction, one asks for the sum of the energies in the cell of the extrapolated primary track and in the 8 cells around in the reported layer i ($E_{\text{around},i}$) to satisfy:

$$\frac{E_{\text{around},i}}{E_i} > 0.5 \tag{5.5}$$

This ensures that the increase of energy was caused near the path of the track and not by a track away from the initial mip. This interaction will again be called a "FireBall" and may be regarded as an inelastic reaction.

– In the second case, the relative increase stops in the fourth layer ($i + 3$). This is defined by:

$$\frac{E_{i+2} + E_{i+3}}{E_{i-1} + E_{i-2}} < \text{Fcut} \tag{5.6}$$

If the relative increase extends only over a couple of layers, it is localized and will be classified as "Pointlike". This is the case of Fig. 5.3 where most of the released energy is localized in a couple of cells.
Due to this presence of highly ionizing particles, "Pointlike" events can be regarded as an opportunity to study details of the short range component of a hadronic shower and are therefore a kind of zoom into that part of the shower. These events might be the result of the evaporation phase of a spallation reaction. The primary particle did not transfer enough energy to the nucleus to release secondaries. Rather the energy is only distributed among the nucleons and excess energy is evaporated in form of invisible neutrons and ionizing charged particles.
As a consequence of this definition, some δ-rays will enter this class. The background expected from δ-rays is studied with simulated muons. The resulting fraction of simulated muon events passing the Pointlike criterion is given in Table 5.2.

E (GeV)	2	4	6	8	10
Rate of δ-rays	2.7%	3.7%	4.0%	3.9%	4.1%

Table 5.2: Rates of δ-rays, estimated to be the fraction of "Pointlike" events found in Monte Carlo simulations of muons. Since the mass of the muon and of the pion are very close, their behavior in terms of electromagnetic interactions can be regarded as very similar.

The remaining events that did not pass those criteria will be considered as non interacting events.

Since the criteria rely on the knowledge of energy deposition in several consecutive layers, some events are discarded: those in which the interaction occurs in the three first and three last layers, see Chap. 6.

Discussion of events for which no interaction is identified

Events where no interaction is found may be separated further into two classes. An example of the latter type is shown in Fig. 5.4, where a scattered particle is clearly seen.

This last kind of event will be classified as a non interacting event for neither Eq. 5.1 nor Eq. 5.3 are satisfied. Indeed, the energy deposition is rather small in consecutive layers, and despite the obvious energy fluctuations seen in the longitudinal profile, pairs of layers do not show any large increase in energy. These events are most likely elastic scattering with negligible nuclear breakup.

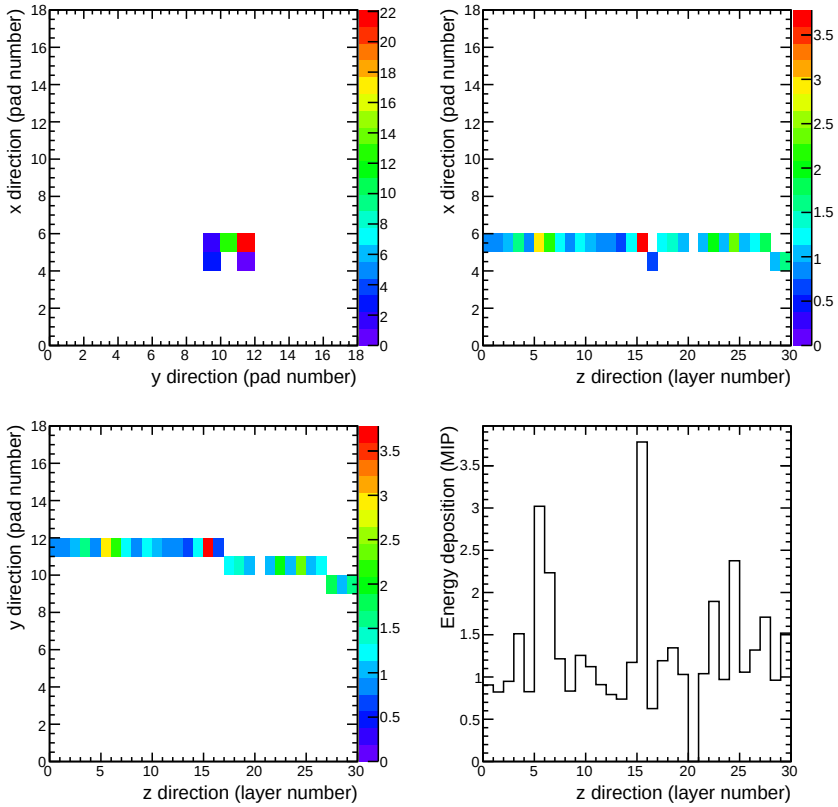

Figure 5.4: Display of a test beam data event at 2 GeV with an elastic scattering. Despite some energy fluctuations, it does not fulfill Eq. 5.1 and Eq. 5.3 and the track has changed direction in the ECAL. This event is of the type "Scattered".

A scattered particle is identified by requiring a lateral distance of at least two pixels between the incoming track and the end of the outgoing track. If the event satisfies this requirement, it will classified as "Scattered". If it is not, it is put in a class called "MIP" which will represent particles which did not undergo any sizable interaction or deviation. Future studies will cluster the outgoing track and measure the angle with respect to the primary track.

5.3 Optimization of the selection criteria

A procedure to find interactions and classify four event types has been presented. It relies on the two parameters Ecut and Fcut which are to be optimized for the algorithm to be as efficient as possible. To do this, Monte Carlo simulations are employed with samples of pions at different energies.

The interaction point of the incoming hadron is defined by the known endpoint of its trajectory given in the simulation. The optimization proceeds in two steps: Ecut is first optimized to find a maximal number of interactions with a reported layer as close as possible to the true interaction layer. Fcut is optimized afterward to find more interactions with small energy deposited but without migration of elastic scattering reactions (or mips).

Events with sizable deposited energy are now defined and separated from the others, and optimization criteria and method are given below.

5.3.1 Interacting and non interacting events

An "interacting event" is defined in the following way.

First, only events with an interaction point inside the ECAL are considered. For these events, the average energy per hit is calculated for each layer:

$$e_{\text{layer}} = \frac{E_{\text{layer}}}{N_{\text{layer}}} \tag{5.7}$$

where E_{layer} denotes the energy in the layer, and N_{layer} denotes the corresponding number of hits.

Second, deducing from the endpoint the interaction layer k, the corresponding distribution is shown in Fig. 5.5 for all energies, featuring the energy per hit for each layer e_i divided by the energy per hit in the last layer before interaction, e_{k-1}. This plot suggests that interacting events in the Monte Carlo be selected using:

$$e_{\text{k}} \geq 1.2\, e_{\text{k-1}} \tag{5.8}$$

It has the clear physical meaning that the energy deposited after the interaction should be higher than before. This reflects the idea that the parameters Ecut and Fcut will be optimized to find events of the type "FireBall" and "Pointlike" i.e. where an interaction occurred.

"Non interacting" events are complementary: those where the particle did not interact in the ECAL volume or those rejected by Eq. 5.8. This definition of non interacting events not only includes mips but also events with elastic scattering. The events of the "MIP" and "Scattered" classes should thus belong to the non interacting events.

The following results of the optimization method are not affected by a small change of the value 1.2 that defines interacting events: this cut range can be varied from 1 to 2 for all energies.

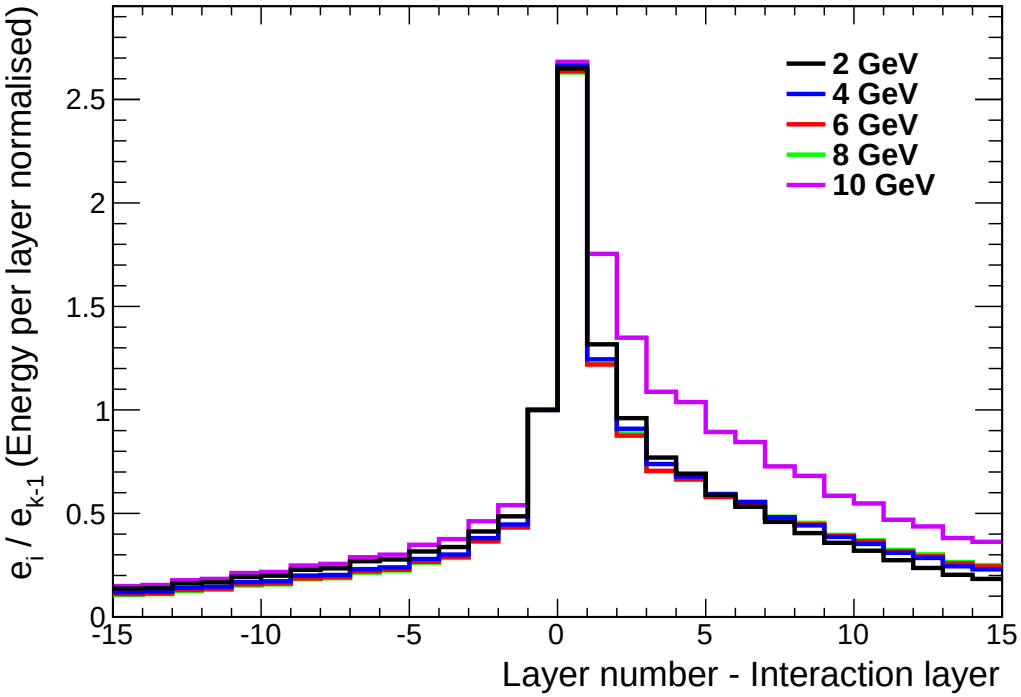

Figure 5.5: The averaged energy per hit in each layer for all energies, divided by the energy per hit in the last layer before interaction $(k-1)$. It is centered around the interaction layer (thus layer 0) and each bin is normalized by its number of counts. (Simulation study)

5.3.2 Variables used

This separation between interacting and non interacting events is used to define the following variables which are used to optimize the cuts.

- **Standard deviation σ**
  The difference between the reconstructed layer and the true interaction layer should be minimal. Thus, the interesting quantity is the standard deviation of this difference. It is obtained by fitting with a gaussian the distribution of *reconstructed layer - true layer* in a range of ± 5 layers around 0. It is calculated with interacting events only.
  $$\sigma = \sigma_{\text{gaussian fit}}(\text{reconstructed layer} - \text{true layer}) \tag{5.9}$$
- **Interaction fraction I_f**
  The interaction fraction I_f is defined by the rate of events where an interaction was found by the algorithm among interacting events:
  $$I_f = \frac{\text{Number of interactions found}}{\text{Number of interacting events}} \tag{5.10}$$

It is to be maximal.

– **Purity with non interacting events P**
The last variable measures the purity P of the algorithm. This is defined by the number of non interacting events identified by the algorithm among the number of non interacting events, i.e.:

$$P = \frac{\text{Number of non interacting events returned}}{\text{Number of non interacting events}} \tag{5.11}$$

The evolution of these three quantities when the cuts are varied led to the following proposal for optimizing the cuts.

5.3.3 Optimization of Ecut and Fcut

Ecut In a first step, Ecut is varied between 1 and 20 MIPs by steps of 1 unit, with the resulting evolution in standard deviation and interaction fraction shown Fig. 5.6 for 10 GeV (a) and 2 GeV (b), while Fcut is kept constant at 6.

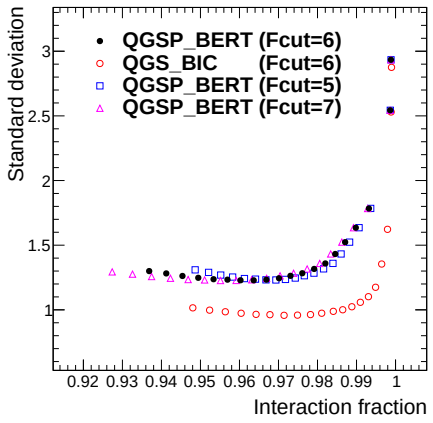

(a) Ecut optimization at 10 GeV.

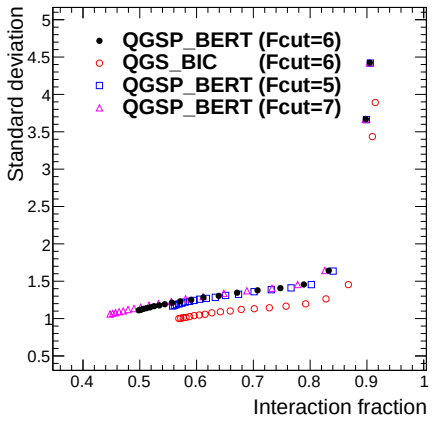

(b) Ecut optimization at 2 GeV.

Figure 5.6: Graphs showing the standard deviation (in units of layer) versus the interaction fraction. The dots are the results of the algorithm with a fixed Fcut (Fcut = 6). The full black dots are for QGSP_BERT and the open red ones for QGS_BIC. The squares represent a change in Fcut: Fcut = 7 (full violet) and Fcut = 5 (open blue) with QGSP_BERT. The energy cut (Ecut) is varied from 1 to 20 MIPs in steps of 1 MIP. The effect of choosing several Fcut values is also shown and does not alter the optimization of Ecut.

For small values of Ecut the algorithm interprets already small energy fluctuations as interactions. Due to this arbitrariness of the identification the standard deviation is naturally very large and the interaction fraction is close to 1. Toward larger values of Ecut the algorithm gets more accurate in identifying the interaction. This leads to a

decrease in the standard deviation. At the same time the interaction fraction remains close to 100%. If Ecut is further increased the algorithms tends to return layers in which the shower has already developed which explains the shallow minimum in Fig. 5.6(a).

For the following optimization process the absolute minimum of the standard deviation is defined as σ_{min} and the maximum of the interaction fraction is defined as $I_{f,max}$, with its corresponding standard deviation σ_{max} which defines $\Delta\sigma = \sigma_{max} - \sigma_{min}$.

To find an optimal value of Ecut, limits on its standard deviation σ and interaction fraction I_f are gradually increased and decreased by using:

$$\begin{array}{rcccl} \sigma(n) & = & \sigma_{min} & + & 0.01n \cdot \Delta\sigma \\ I_f(n) & = & I_{f,max} & - & 0.01n \end{array} \tag{5.12}$$

such that

$$\sigma < \sigma(n) \text{ and } I_f > I_f(n) \tag{5.13}$$

The smallest value of n that permits to find a value of Ecut defines this optimum. In case of several values of Ecut found, the smallest is kept, in favor of a larger interaction fraction.

Figure 5.6(b) shows the the evolution of the standard deviation and the interaction fraction for pions with an energy of 2 GeV. At small energies the distribution does not transit by a minimum as the energy of the secondaries is comparatively small and subject to fluctuations. Still, the same algorithm as developed for larger energies can be used to find the optimal value of Ecut.

The interaction fraction does not reach a 100% level, especially at small energies. This supports again the need for a second criterion, represented by Fcut, to find all of the interactions.

Fcut The introduced value of Fcut is optimized with the help of the purity P as defined in Eq. 5.11 and the interaction fraction. For a constant Ecut of 10 MIPs, Fcut is varied in steps of 0.5 between 1 and 10. The evolution of the purity for pions with an energy of 10 GeV and 2 GeV is shown in Fig. 5.7. For small values of Fcut, a lot of interactions are found which gives the largest interaction fraction, but some fake interactions due to fluctuations are found too, associated with a worse purity. When Fcut is increased, the rate of interactions found decreases and the fake interactions tend to decrease as well thus increasing the purity up to the maximal value P_{max}.

When choosing the optimal value of Fcut the emphasis is put on maintaining a high purity. The optimal value of Fcut is given by the first value for which $P > 0.95 \cdot P_{max}$.

As shown in Figs. 5.6 and 5.7 the optimization is carried out for the two physics lists QGSP_BERT and QGS_BIC . While the actual values of interaction fraction, standard deviation and purity are different, the resulting optimal values are independent of the physics list. This indicates the general applicability of the introduced algorithm.

5.3.4 Results of the optimization

The Table 5.3 shows the optimal values of Ecut and Fcut for different energies. The values for Ecut are energy dependent as expected while the optimal values for Fcut do

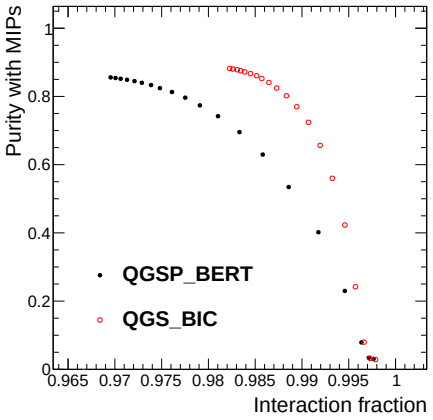

(a) Fcut optimization at 10 GeV with fixed Ecut. (Ecut = 8 MIPs)

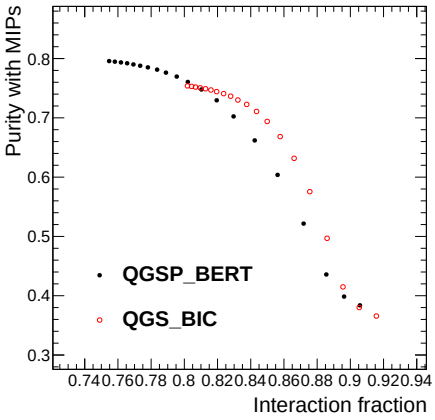

(b) Fcut optimization at 2 GeV with fixed Ecut. (Ecut = 3 MIPs)

Figure 5.7: Graph showing purity versus the interaction fraction. Here Ecut is fixed and different values for Fcut are chosen from 1 to 10 by steps in 0.5. The full dots are for QGSP_BERT and the open red ones for QGS_BIC.

not vary much with energy. In the following the values for Ecut are used as given in the table while Fcut=6 is chosen for all considered energies.

List	QGSP_BERT		QGS_BIC	
E (GeV)	Ecut (MIP)	Fcut	Ecut (MIP)	Fcut
2	3	5	3	5
4	4	6	4	5.5
6	7	6	7	6
8	9	6	7	6
10	8	6.5	7	6

Table 5.3: Cuts used at each energy. They are almost energy independent from 6 to 10 GeV. Since the optimal value for Fcut has a small effect on the efficiencies, a common value of 6 was fixed in the following study.

An example of the correlation between the interaction layer as found by the algorithm and the true interaction layer is given for an energy of 6 GeV in Fig. 5.8. The optimized values of the cuts are chosen. The interaction layer reported by the algorithm is in good agreement with the true one. There are more counts in the odd than in the even layers in the simulation. This is due to the odd-even layer effect mentioned Sec. 3.2.

With these values for Ecut and Fcut, the efficiency η over all interacting events to find the interaction layer in ± 1 layer around the true layer and ± 2 layers around is computed.

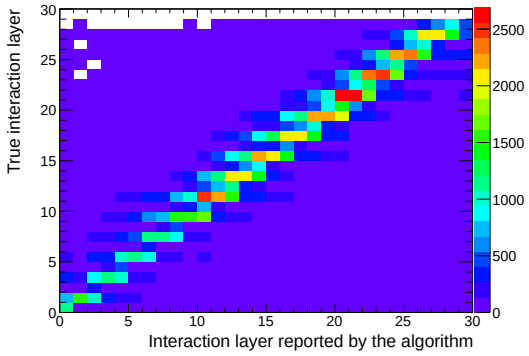

Figure 5.8: Correlation between the true interaction layer as given by the Monte Carlo record and the interaction layer found by the algorithm at 6 GeV.

The result is given in Table 5.4. It shows that the efficiency is always larger than 62% where as expected higher efficiencies are obtained for the higher energies. The results for the wider range can be compared with the "3 out of 4" method, i.e. η_{3-4} with a cut at 10 MIPs like in [AKR$^+$10b].

E (GeV)	$\eta_{\pm1}$	$\eta_{\pm2}$	$\eta_{3-4,\pm2}$
2	0.54	0.62	0.22
4	0.58	0.67	0.51
6	0.62	0.72	0.64
8	0.64	0.75	0.69
10	0.74	0.83	0.78

Table 5.4: Efficiency η to find the interaction at each considered energy with the algorithm within ±1 layer, ±2 layers, compared with the "3 out of 4" method [AKR$^+$10b], i.e. η_{3-4}. Only interacting events are considered.

All samples used are made with QGSP_BERT. It demonstrates that toward small energies the cut scenario presented in this article results in significantly higher efficiencies compared with the simpler method which gets sufficient as the energy increases. The "3 out of 4" method is indeed sufficient at higher energies where most interactions are of the "FireBall" class while at smaller energies, the relative importance of the other classes defined becomes higher.

Chapter 6

Results

The events are classified according to the criteria introduced Chap. 5 and compared with the Monte Carlo predictions by means of their rate, shower radius and longitudinal shower profiles. For a given physics list, the evolution of each profile with respect to the energy is shown. Then at 2 GeV and 8 GeV differences between each physics lists studied are shown.

6.1 Rates of interaction types

The rates of interaction types are defined by the number of events for a given class, divided by the total number of events. Fig. 6.1 shows the rates of interactions for different energies.

The frequency of "Fireball" events in the data is always about 55% nearly independant of the energy. If corrected for the efficiency of finding an interaction, the frequency would increase slightly towards small energies. The observed dependency is compatible with the behaviour of the π-proton cross section [Nak10] as one of the main underlying scattering processes. The events of type "Pointlike" consitute a complementary fraction of inelastic events. When corrected for δ-rays, their frequency is about 4% at small energies and tend towards zero at higher energies. The frequency of both classes for inelastic events is well reproduced by all physics lists which confirms that the total inelastic cross sections are well implemented into the physics lists. This is on the other hand expected since all physics lists implement the underlying π-nucleon scattering at least for the first stage of the intranuclear processes.

For charged pions with kinetic energies above about 1 GeV, the elastic π-proton scattering cross section is expected to be suppressed with respect to the inelastic part [Nak10]. This suppression is observed in the data and well reproduced by all physics lists. The frequency of the events of type "Scattered" classes account for about 5% of the events. The slight increase towards small energies is broadly compatible with the expected behaviour of the elastic π-proton cross section [Nak10].

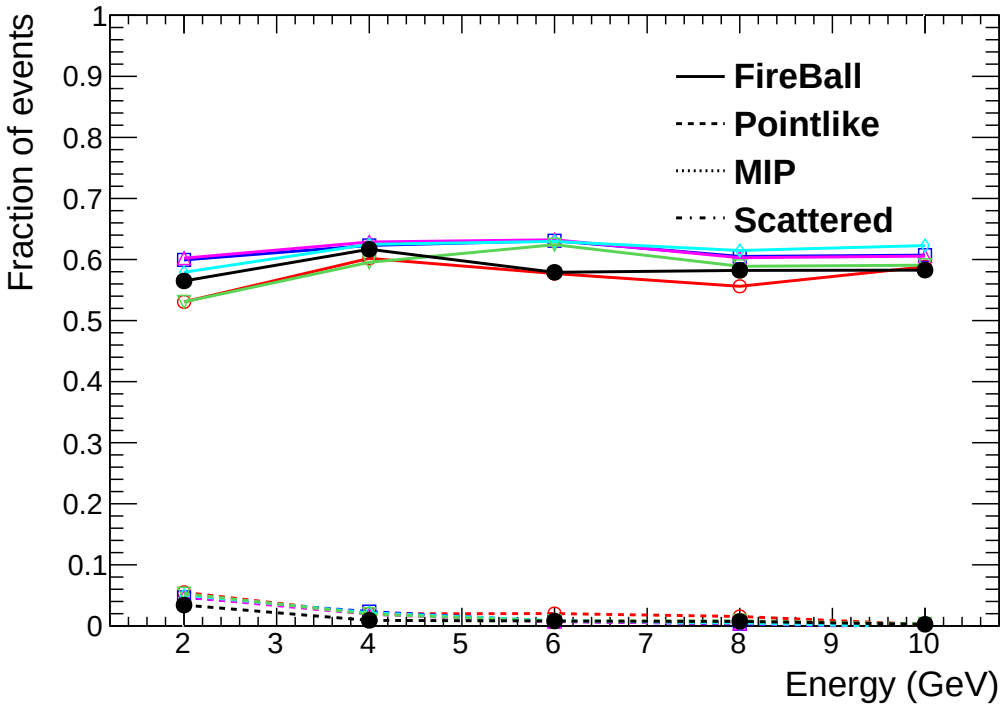

(a) Interaction classes

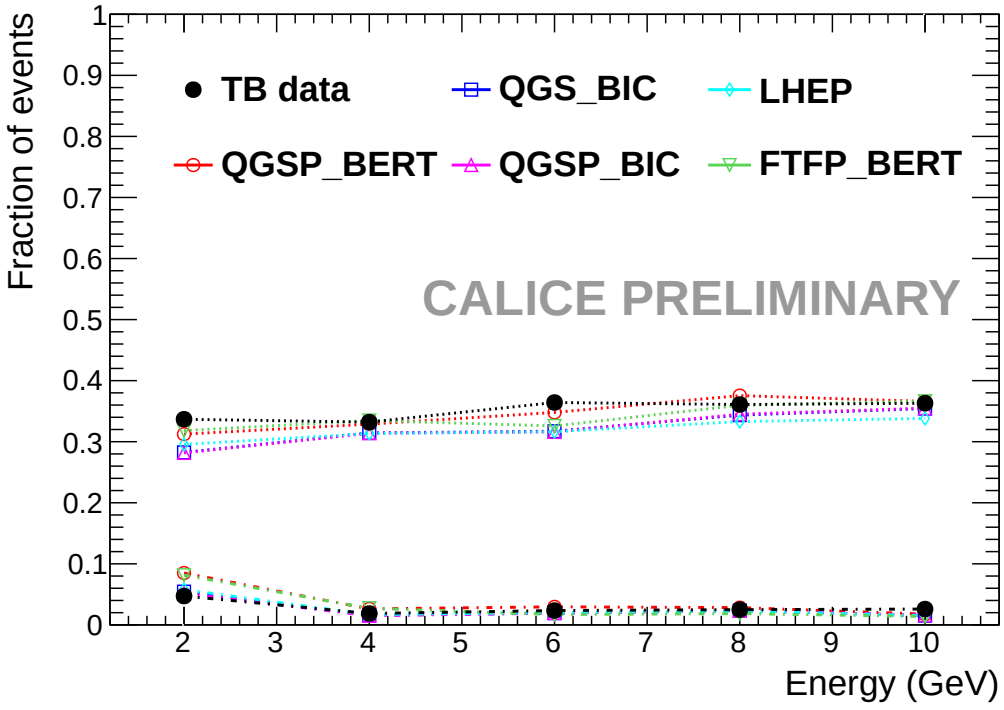

(b) Non interaction classes

Figure 6.1: Rates of interactions with various physics lists and energies from 2 GeV to 10 GeV. The two graphs in (a) comprise fractions of events with an interaction seen, namely the "FireBall" and "Pointlike" classes, resulting in an interaction layer reported by the algorithm. The two graphs in (b) comprise fractions of events with no interaction seen, the "MIP" and "Scattered" classes.

6.2 Lateral extension of the showers

A measure of the transversal extension of the final state of the four event types is the shower radius. The shower radius is defined by:

$$\mathrm{R_E} = \sqrt{\sigma^2_{\mathrm{E,x}} + \sigma^2_{\mathrm{E,y}}} \tag{6.1}$$

where e.g.

$$\sigma^2_{\mathrm{E,x}} = \frac{\sum\limits_{\mathrm{hits}} x^2_{\mathrm{hit}} E_{\mathrm{hit}}}{\sum\limits_{\mathrm{hits}} E_{\mathrm{hit}}} - \left(\frac{\sum\limits_{\mathrm{hits}} x_{\mathrm{hit}} E_{\mathrm{hit}}}{\sum\limits_{\mathrm{hits}} E_{\mathrm{hit}}} \right)^2 \tag{6.2}$$

and the same for y. For the calculation of the observables, only hits in the interaction layer and all subsequent layers are taken into account.

In order to define in the same way a measure of the radius of non interacting events, i.e. interactions where no interaction point could be found, the width $\mathrm{R_E}$ is calculated by summing over all hits in the ECAL.

The profiles shown Fig. 6.2 contain each event at energies from 2 GeV up to 10 GeV. Two distinct maxima are visible: a sharp one around 5 mm and a broader one at larger values. The first one is the one expected for mips that pass through the ECAL in straight line, the second being the one of the interacting hadrons which contribute to the large radii in the distribution.

For energies smaller than 6 GeV small radii up to about 35 mm are well reproduced by the simulation. Toward higher energies, the transition region between the two maxima is less well described by the simulation. At all energies the simulation does not describe the region of large shower radii. The showers seem to be on average broader in the simulation. The description gets however somehow better at the highest energy of 10 GeV.

Using the classification introduced in Chap. 5, it is possible to separate the contribution of each event type. As shown in Fig. 6.3 at 8 GeV, the hadron peak is seen in the events classified as "FireBall". The classes of type "Pointlike" and "Scattered" populate the transition region. Finally, the mip peak is associated with events classified as "MIP" events.

It can be seen in Fig. 6.3 for "Fireball" events that the data undershoot the simulation using QGSP_BERT at large radii which is in agreement with the observation in Figure 6.2. At small radii the situation is inverted, the data exceed the simulation. An excess in the measured radii with respect to the simulation can also be observed for the "Pointlike" events. This observation indicates a deficiency of the simulation to reproduce correctly the topology of weakly populated final states. Note also that naturally there are migrations between the event classes "Fireball" and "Pointlike" and that the migrating events populate the distribution at small radii. This allows for the conclusion that the disagreement in "Fireball" and "Pointlike" at small radii are most presumably of the same origin.

The disagreement visible for the "Scattered" and "Pointlike" event types confirms the result that the simulation does not reproduce correctly weakly populated final states.

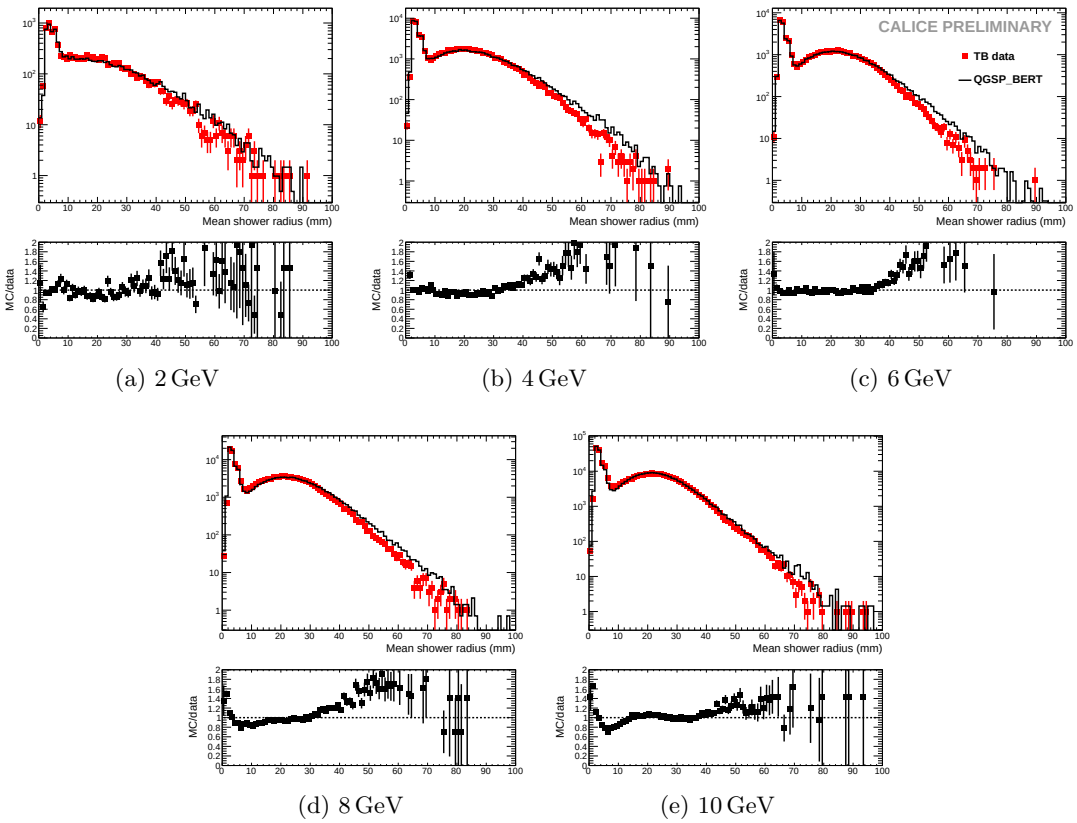

(a) 2 GeV (b) 4 GeV (c) 6 GeV

(d) 8 GeV (e) 10 GeV

Figure 6.2: Mean shower radius: the top view features the comparison between test beam data (points with error bars) and QGSP_BERT (solid histograms) for each energy. The bottom view shows the ratio of test beam over Monte Carlo data and is limited to the range $[0, 2]$. The Monte Carlo data have been normalized to the number of data events for comparison.

Finally, the disagreement for the "MIP" event type is not expected and currently not completely understood. It might be caused by "Pointlike" events which migrate into the sample of mip events as the disagreement is most prominent at radii corresponding to the maximum seen in the distribution of the "Pointlike" event types. Misalignment effects are also under study.

The events of type "Pointlike" and "Scattered" are compared in Figure. 6.4 with simulations based on the FTFP_BERT physics list. For convenience the comparison with the QGSP_BERT is shown also in the figure. Both distributions are slightly better described by the FTFP_BERT physics list.

The Fig. 6.5 presents the same comparison as Fig. 6.3 but now for pions with an energy of 2 GeV. Though conclusions are weakened by the smaller statistics, the distributions at these small energies are broadly reproduced by the simulation. This is

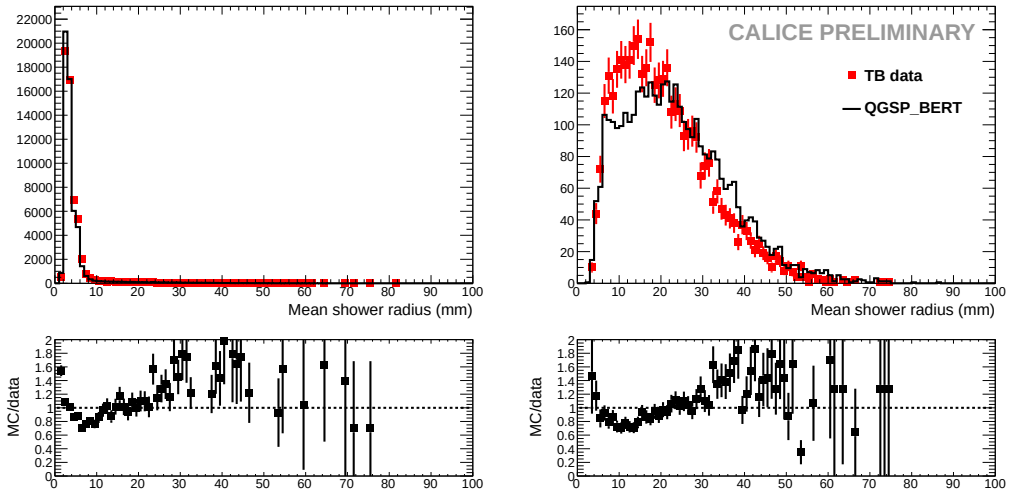

(a) “MIP”

(b) “Scattered”

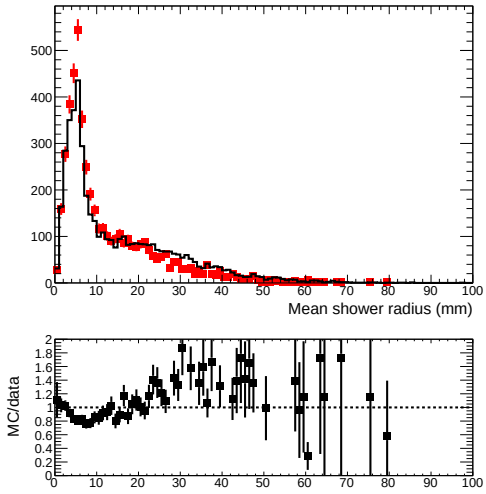

(c) “Pointlike”

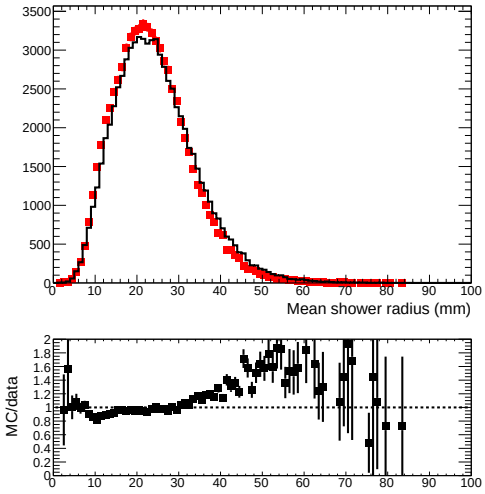

(d) “FireBall”

Figure 6.3: Mean shower radius: the top view features the comparison between test beam data (points with error bars) and QGSP_BERT (solid histograms) at 8 GeV with each class separated. The bottom view shows the ratio of test beam over Monte Carlo data and is limited to the range $[0, 2]$. The Monte Carlo have been normalized to the number of data events for each class. (a) and (b) show non interacting events while (c) and (d) show events with an interaction found. The apparently large difference in (b) comes from the larger uncertainties as well as from the physics list itself.

particularly true for the events of type “Fireball” with the same tendency for the events of type “Pointlike”. Note, that for pions with an energy 2 GeV the distribution for events

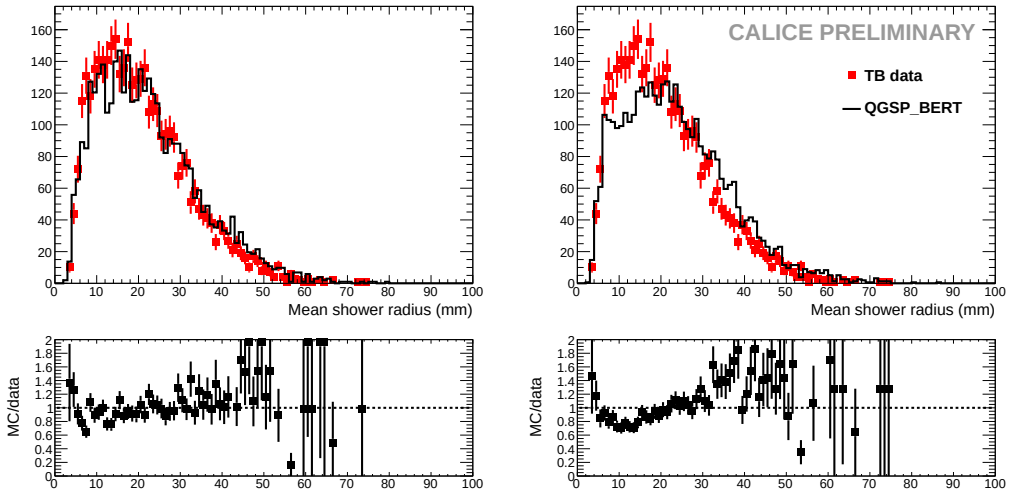

(a) "Scattered" – FTFP_BERT

(b) "Scattered" – QGSP_BERT

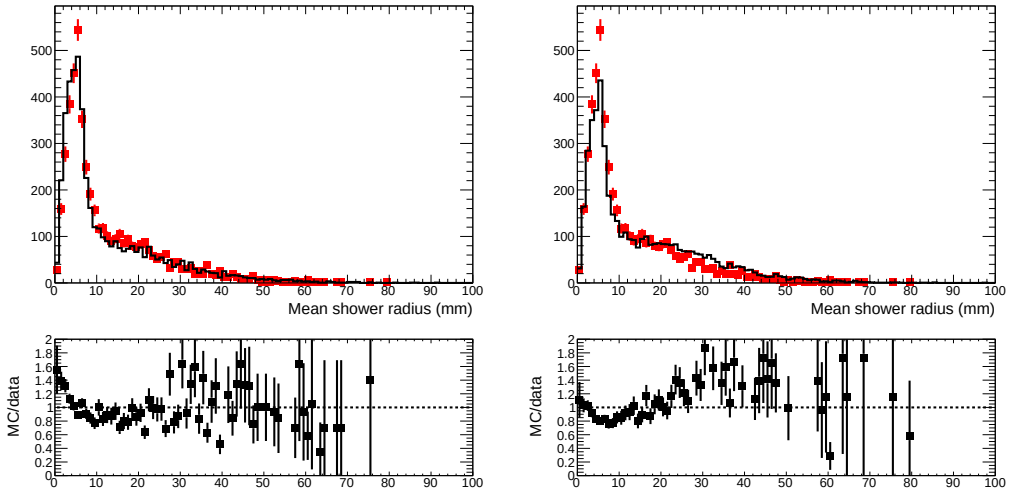

(c) "Pointlike" – FTFP_BERT

(d) "Pointlike" – QGSP_BERT

Figure 6.4: Mean shower radius: the top view features the comparison between test beam data (points with error bars) and QGSP_BERT (solid histogram, left plots) and FTFP_BERT (solid histogram, right plots) at 8 GeV for the "Scattered" class (top plots) and "Pointlike" class (bottom plots), where the Monte Carlo data have been normalized to the number of data events. The bottom view shows the ratio of test beam over Monte Carlo data and is limited to the range $[0, 2]$. The difference seems to come from the physics list itself since FTFP_BERT describes correctly the behavior, but the statistical uncertainties are to be taken into account and the differences seen with QGSP_BERT may still be acceptable.

of type “MIP” is also better described than for pions with an energy of 8 GeV.

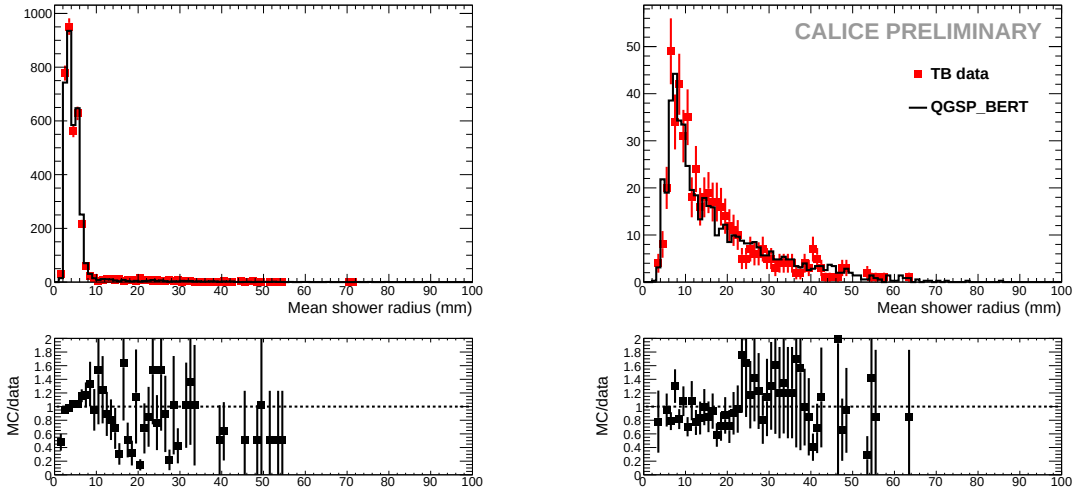

(a) “MIP”

(b) “Scattered”

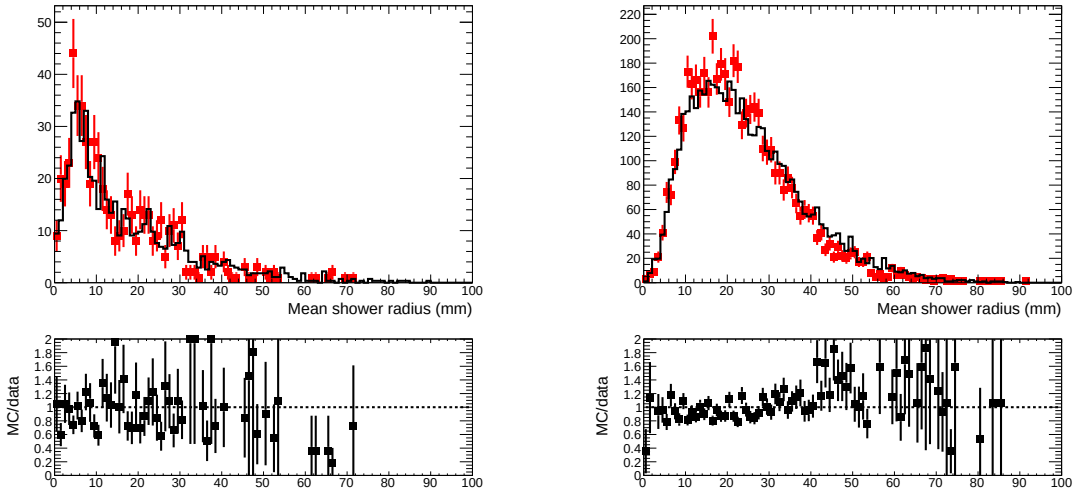

(c) “Pointlike”

(d) “FireBall”

Figure 6.5: Mean shower radius: the top view features the comparison between test beam data (points with error bars) and QGSP_BERT (solid histograms) at 2 GeV with each class separated, for which the Monte Carlo data have been normalized to the number of data events. The bottom view shows the ratio of test beam over Monte Carlo data and is limited to the range $[0, 2]$. The statistics is reduced at 2 GeV and the efficiency of the algorithm is worse. Nevertheless the Monte Carlo are still in good agreement with the test beam data. (b) and (c) seem to come from the similar physics processes, as is expected at this small energy.

6.3 Longitudinal profiles

The longitudinal profiles are defined as introduced in [AKR+10b]. The longitudinal profile is given as a function of *pseudolayers* in order to account for the different sampling fractions in the ECAL. There is a one to one correspondence between real layers and *pseudolayers* in the first module. On the contrary, each layer in the second module has been subdivided in two *pseudolayers* and layers of the third module have been subdivided into three *pseudolayers*. The energy is then linearly interpolated within the pseudolayers between the energy in the previous layer and the energy in the considered layer.

The longitudinal shower profile given in the following histograms starts always from the found interaction layer. All interactions found between the three first and the three last layers are considered. In case of non-interacting events, the longitudinal profile is calculated from the first detector layer.

Fig. 6.6 shows the profiles as defined above for all selected events. The data are compared with a detector simulation based on the QGSP_BERT physics list. Here and in the following histograms are normalized bin per bin since each event does not count in the same way, especially in the last pseudolayers which will be less hit.

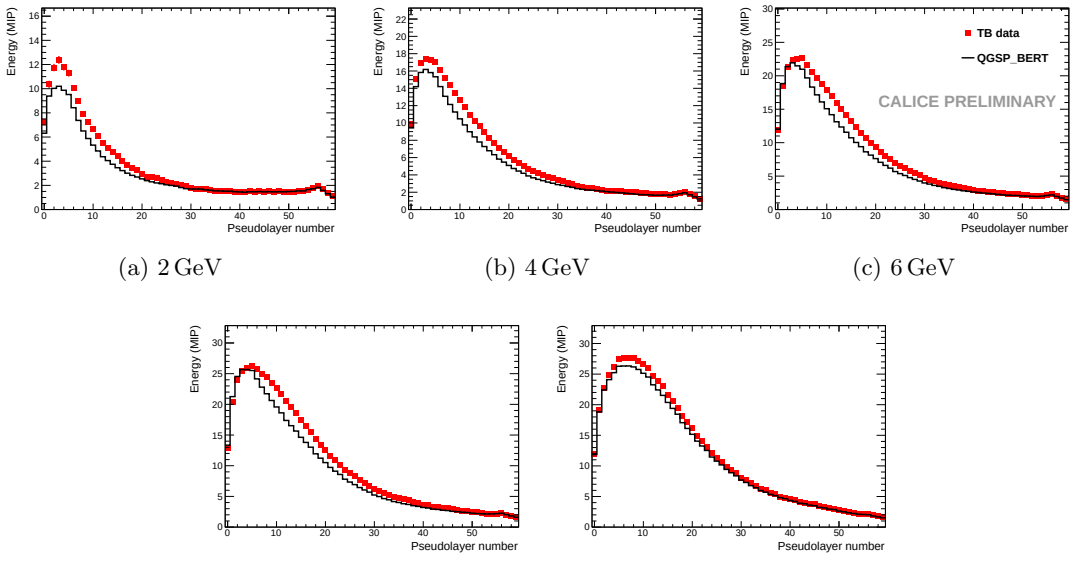

(a) 2 GeV (b) 4 GeV (c) 6 GeV

(d) 8 GeV (e) 10 GeV

Figure 6.6: Total longitudinal profiles for all event types: comparison between test beam data (points with error bars) and QGSP_BERT (solid histograms) for each energy, taking every event into account. The energy is always underestimated by the physics list but the agreement improves above 6 GeV.

The profiles are broadly reproduced by the simulation. The maximum in early layers is created mainly by the events of type "FireBall". Some profiles feature a small second maximum which is caused by events which are classified as MIPs but interact late in the

detector. For a more detailed discussion of the longitudinal profiles the different event types will be used in the following.

6.4 Longitudinal profiles per class of events

For the comparison of data and Monte Carlo in terms of the introduced event classes, those in which an interaction could have been identified, i.e. "FireBall" and "Pointlike" are of primary interest. An example of "MIP" and "Scattered" profile is given for QGSP_BERT, Sec. 6.4.3.

For simulated events, the energy contributions for each bin will be decomposed according to the identity of the secondary particle responsible for the energy deposition. In blue, all contributions from electrons and positrons are summed. In green, contributions from protons can be seen. In red, contributions of pions that is, mip-like particles, are drawn. Finally, the violet histograms are contribution from other particles. The black histogram representing the total is shown for direct comparison with the real data points.

6.4.1 "FireBall" events

Due to their comparatively high frequency, events of type "FireBall" dominate the total profiles of Fig. 6.6. In Fig. 6.7, the "FireBall" events are shown for the Bertini-based models (QGSP_BERT and FTFP_BERT) and LEP based models at 2 GeV. None of the models give a satisfactory description of the data. In Bertini based models, the largest contribution to the profile comes from protons but the energy in the shower maximum is slightly underestimated. In other models using the LEP model, the component labeled "others", which contains heavy nuclei, is dominant in the first layers and the energy in the shower maximum is overestimated. The models based on the Bertini cascade lead to a slightly better description of the tail of the longitudinal profiles. In this case it looks as if the smaller proton component in case of the LEP physics is responsible for the difference in the simulated distributions.

The Fig. 6.8 shows the corresponding distributions at 8 GeV. Again no satisfactory description of the entire profile can be achieved. The region around the maximum is better approximated by the QGSP_BERT and FTFP_BERT physics lists. On the other hand the tails are better described by the QGSP_BIC physics list. Here again the difference between the lists in the contribution from the proton component of the shower is striking.

6.4.2 "Pointlike" events

The "Pointlike" events as shown Fig. 6.9 and Fig. 6.10 feature a strong peak at early layers and then a sharp drop off after 6 pseudolayers. This sharp drop is partially due to the chosen cut scenario but reflects also the short travel distance of highly ionizing particles. It is remarkable that the height of the peak is almost the same at both energies. This indicates that at both energies the same mechanism is responsible for these kind of events.

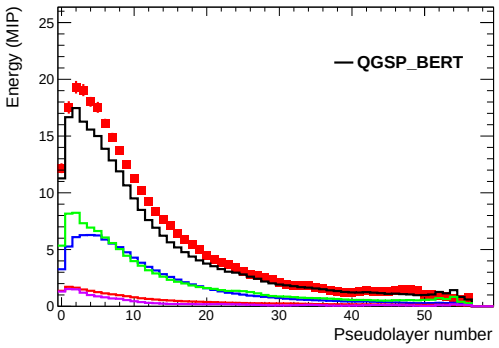

(a) BERT : valid for QGSP_BERT (shown here) and FTFP_BERT

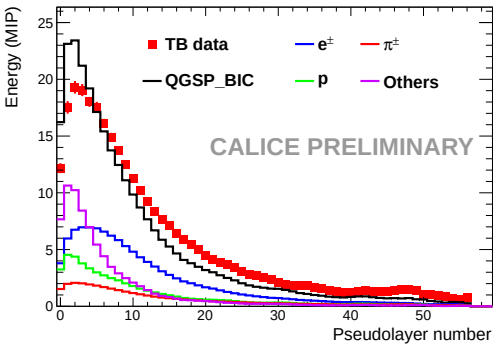

(b) LEP : valid for QGSP_BIC (shown here), QGS_BIC and LHEP

Figure 6.7: Longitudinal profiles: comparison between test beam data (points with error bars) and QGSP_BERT and QGSP_BIC lists (solid histograms) at 2 GeV for selected "FireBall" events.

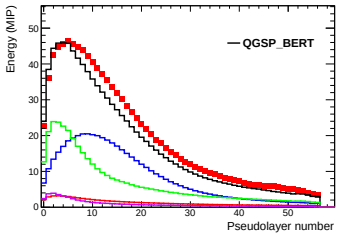

(a) QGSP_BERT featuring the BERT model

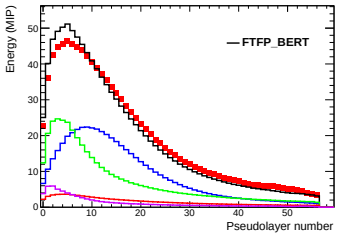

(b) FTFP_BERT

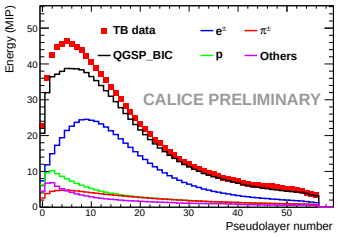

(c) QGSP_BIC featuring the LEP model

Figure 6.8: Longitudinal profiles: comparison between test beam data (points with error bars) and QGSP_BERT, FTFP_BERT, QGSP_BIC lists (solid histograms) at 8 GeV for selected "FireBall" events.

As shown in Fig. 6.9 at 2 GeV this particular class of events favors the BERT physics list which features a dominant proton component. The LEP physics list overshoot the measured spectra. This list realizes a large part of the energy deposition by particle labeled as "others", namely nuclei with $A > 1$.

At 8 GeV, see Fig. 6.10, the Pointlike events are relatively well modeled by both, the FTFP_BERT and the QGSP_BERT physics list. Differences in the predictions are due to the different energy depositions by heavy nuclei labeled as "others" in Fig. 6.10. The list QGSP_BIC based on the LEP model fails completely to reproduce the measured spectrum. In contrast to the situation at 2 GeV the energy deposition by heavy nuclei is drastically smaller. On the other hand none of the other components gets enhanced.

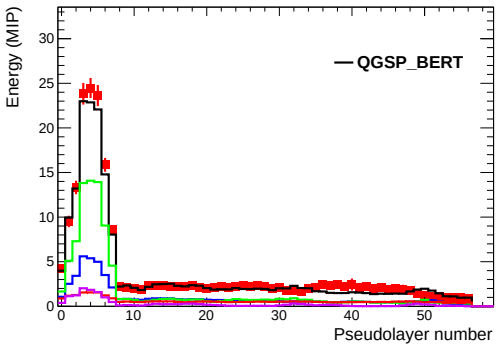

(a) BERT : valid for QGSP_BERT (shown here) and FTFP_BERT

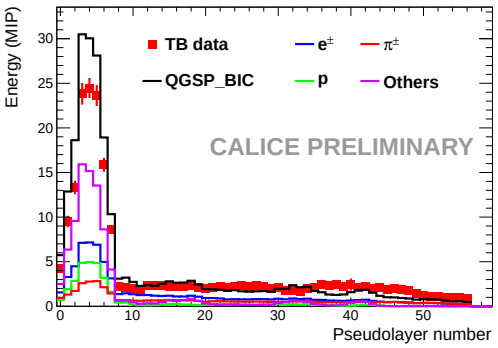

(b) LEP : valid for QGSP_BIC (shown here), QGS_BIC and LEP

Figure 6.9: Longitudinal profiles: comparison between test beam data (points with error bars) and QGSP_BERT, QGSP_BIC lists (solid histograms) at 2 GeV for selected "Pointlike" events.

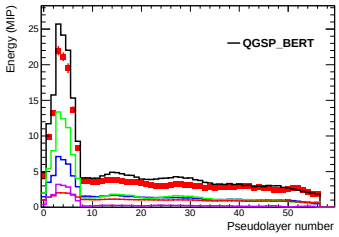

(a) BERT, used by QGSP_BERT

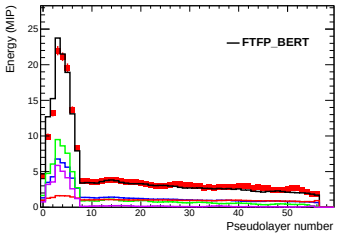

(b) FTFP_BERT

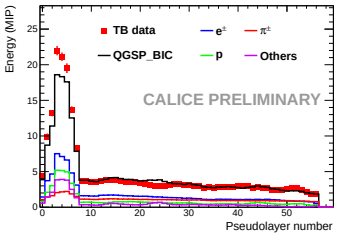

(c) LEP, used by QGSP_BIC (shown here), QGS_BIC and LEP

Figure 6.10: Longitudinal profiles: comparison between test beam data (points with error bars) and QGSP_BERT, FTFP_BERT and QGSP_BIC lists (solid histograms) at 8 GeV for selected "Pointlike" events.

6.4.3 Longitudinal profiles for "MIP" and "Scattered" events

For completeness, the longitudinal profiles obtained for events with no interaction found is shown Fig. 6.11. The physics list is QGSP_BERT.

For the "MIP" part, no discrepancy is seen. An increase in the energy deposition in the last *pseudolayers*. Having a look at the proton content which is representative for the start of showers as seen Sec. 6.4.1, one can infer that this comes from events where the interaction was not found and thus enter the "MIP" class. Since the interaction occurs in the last layers of the ECAL, it is clearly due to the algorithm which cannot find interactions in the two last layers.

A particular alternated structure is seen for the electromagnetic subcomponent while

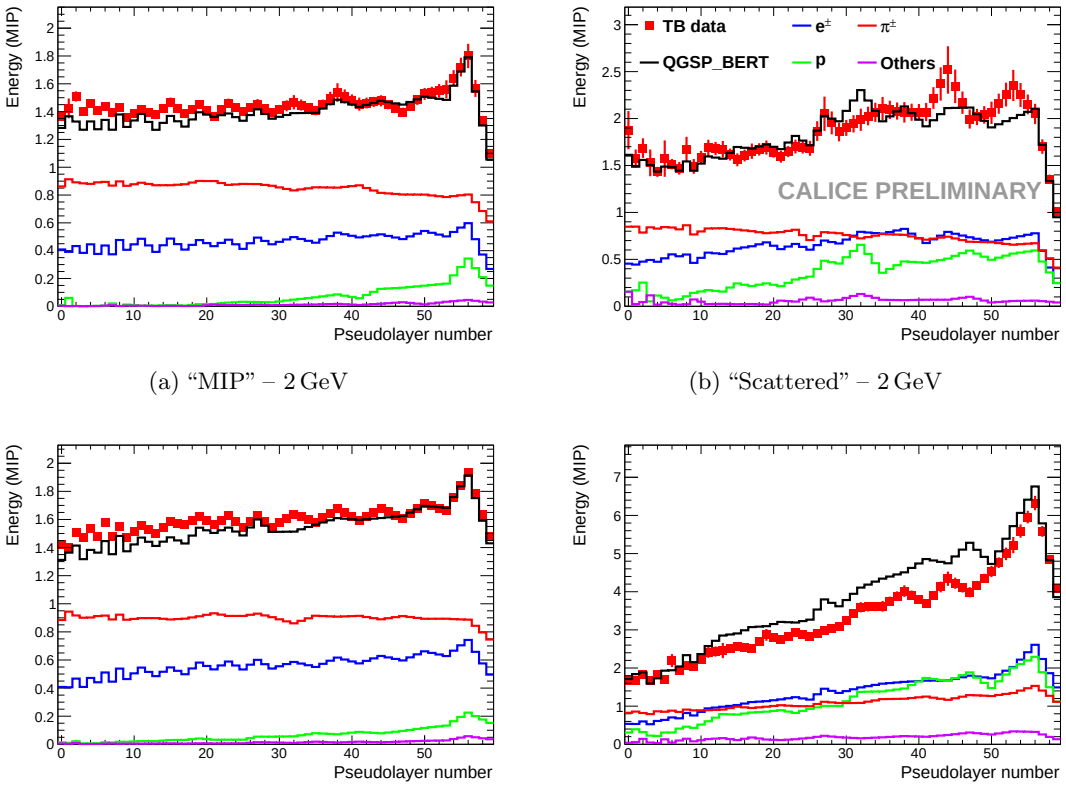

(a) "MIP" – 2 GeV

(b) "Scattered" – 2 GeV

(c) "MIP" – 8 GeV

(d) "Scattered" – 8 GeV

Figure 6.11: Longitudinal profiles: comparison between test beam data (points with error bars) and QGSP_BERT (solid histogram) at 2 GeV and 8 GeV for the two classes with no interaction found.

the pion one is almost flat. This is an odd-even layer effect due to the alternated structure of the layers, seen Sec. 3.2.

The longitudinal profile for the "Scattered" events gather events missed by the cuts but still contain information on interactions with low energy deposition. Due to the loose energy cut at 2 GeV of Ecut = 3 MIPs, it is not likely that interacting events will be a large part of this class, see Fig. 6.11 (b), apart from later interactions which needed a further cut to remove noise. On the contrary, since the cut at 8 GeV is tighter (Ecut = 10 MIPs), more interacting events that have not been found will be left. The deposited energy increases with increasing detector depth. This is plausible since an interaction at larger depth is more likely to be missed than an interaction occurring in early layers.

6.5 Summary, conclusions and outlook

A deep understanding of hadronic showers is of general interest and naturally supports the future development of particle flow algorithms for detectors at a future linear collider. This study demonstrates the outstanding potential of the CALICE SiW ECAL to obtain a detailed image of hadronic cascades. The data obtained in test beams with pions of an energy between 2-10 GeV are compared with Monte Carlo predictions employing different physics lists as contained in the simulation toolkit GEANT4. The start of the hadronic shower can be reconstructed to an accuracy of better than two layers with an efficiency between 62% and 83% depending on the energy of the primary particle. A classification of the reaction which the pions undergo in the calorimeter volume is realized. Currently, it is possible to distinguish between mip-like events, elastic scattering events, spallation reactions and inelastic reactions. The quality of the description of the data varies with the energy of the primary particle and the chosen physics lists. None of the chosen physics lists can describe the entire set of data. Models based on the Bertini cascade, i.e. QGSP_BERT and FTFP_BERT tend to be closer to the data than e.g. the LEP based physics lists.

The next step will be to classify inelastic reactions in terms of shower topology. This comprises the determination of size and energy density of the interaction region as well as the measurements of tracks emerging from the interaction region. These steps will exploit further particularly the lateral granularity of the ECAL. They may form a solid base for the development or the improvement of particle flow algorithms.

Future studies have to include the HCAL to see the full development of the showers and prepare robust clustering algorithms based on the high granularity of the calorimeters.

Part II

Top pair production at the ILC

This part of the thesis describes mainly a simulation study of top quark production at the ILC at a center-of-mass energy $\sqrt{s} = 500\,\text{GeV}$ and an integrated luminosity of $\mathcal{L} = 500\,\text{fb}^{-1}$ using a detailed simulation of the ILD detector.

The study focuses on the top quark to Z boson couplings, that can significantly differ from the SM ones, in particular in the context of extra-dimensional models. An example of these models is emphasized in Chap. 7. The characteristics of the semileptonic decay channel of the top pairs is presented Chap. 8 and the design of the International Large Detector (ILD) is presented Chap. 9. Relevant detector performances for this analysis are checked in Chap. 10 and resulting figures on the measurement accuracies are derived from the semileptonic top reconstruction, Chap. 11.

Chapter 7

A composite top scenario

The Higgs field was introduced in Sec. 1.2 to provide a mechanism in the SM to generate the masses of gauge bosons and fermions. However, these masses are left as free parameters and an explanation for their hierarchies is still to be found.

An extension of the SM was proposed in 1999 by L. Randall and R. Sundrum [RS99b, RS99a]. By adding one dimension to space with a so-called "warped" metric, they show that it is possible to accommodate the bosonic hierarchies, from the Planck mass, down to the electroweak scale. The virtue of this warped extra-dimension is that it addresses the fermionic hierarchy too, as explained Sec. 7.1.

A modified Randall-Sundrum scenario is presented in Sec. 7.2. It is very appealing since it provides a possible explanation for the deviation of the A_{FB}^b measurement at LEP, using the mixing features of extra gauge bosons. It is of particular interest for experiments: not only does it suggest that new particles in the TeV mass range can be discovered at the LHC but it also predicts important consequences for the top quark, measurable at the ILC.

7.1 The warped model of five dimensions

Five dimensional models were firstly proposed by O. Kaluza and T. Klein independently for the unification of electromagnetism and gravity [CFA87]. Due to the compactness of the fifth dimension of finite size, the wave functions of all particles can be decomposed on an orthogonal basis in the fifth dimension which decouples from the four others with an infinite sum over the so-called Kaluza-Klein modes, with the zero mode representing the SM particles.

The Randall-Sundrum model of warped extra-dimensions adds a fifth dimension to the four dimensional SM and uses a warped metric such that:

$$ds^2 = e^{-2kR\phi}\eta_{\mu\nu}dx^\mu dx^\nu - R^2 d\phi^2 = \frac{1}{(kz)^2}(\eta_{\mu\nu}dx^\mu dx^\nu - dz^2) \tag{7.1}$$

where $\eta_{\mu\nu}$ is the 3+1 Minkowski metric and the fifth dimension is represented by ϕ, $y = R\phi$ or $z = e^{ky}/k$ depending on the authors. The gravity is embedded between an

infrared (IR) four dimensional brane where the SM fields lie ($z_{\rm IR} = \Lambda_{\rm IR} = L \sim 1/TeV$, or $\phi = \pi$) and an ultraviolet (UV) brane ($z_{\rm UV} = 1/k \sim 1/M_{\rm Pl}$, or $\phi = 0$). The gravitons propagate in the space between the two branes (the bulk). The five dimensional space is an Anti deSiter (AdS) space and $1/k$ represents its curvature radius.

In order to solve the gauge-hierarchy problem, the Higgs is confined on the IR brane. On the IR brane, the metric reads $g_{\mu\nu,IR} = \eta_{\mu\nu} e^{-2kR\pi}$. The corresponding Einstein-Hilbert action with the associated metric reads:

$$\begin{aligned} \mathcal{L}_H &= \sqrt{det(-g)}(g^{\mu\nu,IR}\partial_\mu\phi^\dagger\partial_\nu\phi - \mu^2\phi^\dagger\phi - \lambda(\phi^\dagger\phi)^2) \\ &= e^{-4kR\pi}(\eta^{\mu\nu}e^{2kR\pi}\partial_\mu\phi^\dagger\partial_\nu\phi - \mu^2\phi^\dagger\phi - \lambda(\phi^\dagger\phi)^2) \end{aligned} \tag{7.2}$$

The Higgs field can be redefined by $\phi \to \phi e^{-kR\pi}$ and $\mu \to \mu e^{-kR\pi}$ too. Recall that all of the SM masses are proportional to the vacuum expectation value v of the Higgs field $v = \sqrt{\frac{-\mu^2}{\lambda}}$ following Eq. 1.13, which is thus changed by $v \to v e^{-kR\pi}$. After electroweak symmetry breaking, this exponential "warping" factor modifies not only gauge bosons, which explains the bosonic hierarchy between $M_{\rm Pl}$ and $\Lambda_{\rm IR}$, but also fermions. The physical mass scales get redshifted from the UV brane to the IR brane via this warping factor.

7.1.1 Geometrical localization of fermions in 5D

The 5D bulk masses of the fermions can be written ck where the parameter $c \sim \mathcal{O}(1)$ is a localization parameter that specifies the wave-function in the fifth dimension and can be fixed for each fermion. See e.g. [Bou10] for a detailed study.

All of the fermions in 5D have a profile in the fifth dimension that is given by this c parameter. Left-handed and right-handed fermions which do not belong to the same representations may thus have different profiles along the fifth dimension. The four dimensional parameters (e.g. Yukawa couplings) are given by an integration over the fifth dimension of the five dimensional Lagrangian.

The mass of a SM fermion, i.e. the zero Kaluza-Klein mode, is still given via Yukawa coupling to the Higgs boson, e.g. Eq. 1.15, thus by the overlaps of the right-handed and left-handed zero mode wave-functions on the IR brane, where the Higgs is localized. Some typical wave-functions are illustrated in Fig. 7.1 and show the difference between light and heavy fermions. In the model, the light fermions are situated close to the UV brane while the heavier fermions are closer to the IR brane.

7.1.2 The duality with 4D conformal field theories (CFT)

Five dimensional Randall-Sundrum models are actually dual to strongly coupled four dimensional theories, via the AdS/CFT correspondence [Mal99]. While the four dimensional CFT theory cannot be calculated because of the strong values of the couplings, its five dimension AdS dual is calculable using the perturbative theory.

The theory is able to regularize the $W_L W_L$ scattering process. To do this it uses composite bound states, equivalent to the ρ in QCD which regularizes $\pi\pi$ scattering am-

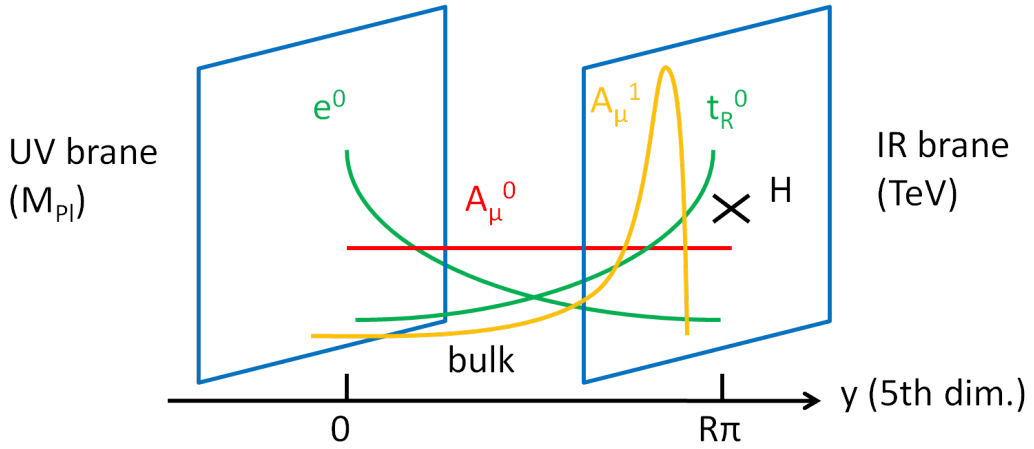

Figure 7.1: A schematic view of wave-functions in the fifth dimension. Fermions (e, t) are accommodated, depending on their mass, near the UV brane or near the IR one where the Higgs boson (H) is localized. Their profile resembles that of an exponential while SM bosons (A_μ^0) have flat profiles but their first KK excitation (A_μ^1) is localized near the IR brane.

plitude. These bound states are dual to the Kaluza-Klein modes appearing in the context of a fifth dimension and could thus even lead to models without Higgs as in [CGPT04].

The models considered here use composite Higgs boson and top quark and are similar to Technicolor models.

7.2 Some implications on phenomenology

The model presented in [DMR07] proposes to enhance the gauge structure in the bulk to $SU(2)_L \times SU(2)_R \times U(1)_X$ which has a Z' (from $SU(2)_R$) without zero mode. Masses of the first Kaluza-Klein modes of the gauge bosons matching the electroweak precision measurements can be of a few TeV as shown in [ADMS03]. There are mixing of the Z boson to its Kaluza-Klein modes, as well as Z-Z' mixing which modify the couplings with the fermions with respect to the standard model bosons. These couplings of Z to fermions are modified by:

$$\frac{\Delta Q_Z^{f_{L/R}}}{Q_Z^{f_{L/R}}} = \frac{M_Z^2}{(0.4 M_{KK})^2}\left[1 + \frac{1}{4F(c_{f_{L/R}})}(1 - \frac{1}{kR\pi}) + \frac{g_{Z'}^2 Q_{Z'}^{f_{L/R}} Q_{Z'}^H}{g_Z^2 Q_Z^{f_{L/R}} Q_Z^H}\right] F(c_{f_{L/R}}) \qquad (7.3)$$

with the F function given in [DMR07]. The first part of its right hand side corresponds to the mixing of the Z boson to its Kaluza-Klein modes while the second part (with $g_{Z'}^2$ in the numerator) corresponds to Z-Z' mixing. A typical diagram of this mixing effect is shown for the top quark Fig. 7.2

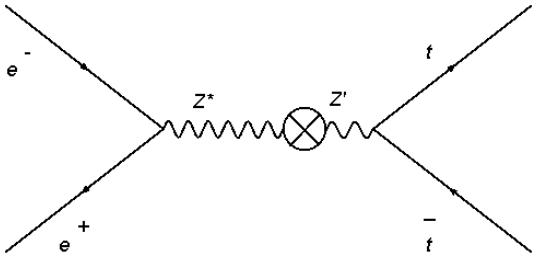

Figure 7.2: Feynman diagram of $Z - Z'$ mixing inducing a change in the $Zt_R\bar{t}_R$ and $Zt_L\bar{t}_L$ couplings. $Z - Z_{KK}$ mixing also exists.

One possibility of this setup is to understand the deviation measured by LEP in the bottom sector on A_{FB}^b while the cross-section tends to agree with the SM predictions.

Using the third generation of quarks, one is left with three mass parameters: c_{b_R}, c_{t_R} for the five dimensional masses of the right-handed bottom and top quark, and $c_{b_L} = c_{t_L}$ which follows from $SU(2)_L$ invariance. One needs to reproduce the masses m_b and m_{top} but also preserve the cross-section of $e^+e^- \to b\bar{b}$ measured precisely at LEP. It is possible to adjust c_{b_R} and c_{b_L} while remaining in the acceptance of LEP measurements and change the values foreseen for A_{FB}^b [DMR07].

Eq. 7.3 allows for deviations of the top couplings to the Z boson too, via Z_{KK} and Z' mixing. These modifications of the $Zt_L\bar{t}_L$ coupling $Q_Z^{t_L}$ can be of -1% while the $Zt_R\bar{t}_R$ coupling $Q_Z^{t_R}$ could change by -34% and the polarised asymmetry of top pair production $A_{LR}^{0,t}$ would drop from 36.7% to approximately -30% at the ILC.

Various models implement the idea of Randall-Sundrum, like those by Djouadi [DMR07], Hosotani [HM05], Gherghetta [CGS10] or Carena [CPSW06]. Their predicted deviations from the SM of the left and right top couplings to the Z boson are indicated Fig. 7.3 and a few per-mil precision on each couplings would allow to separate among them unambiguously. This feature puts forward the top quark studies at the ILC.

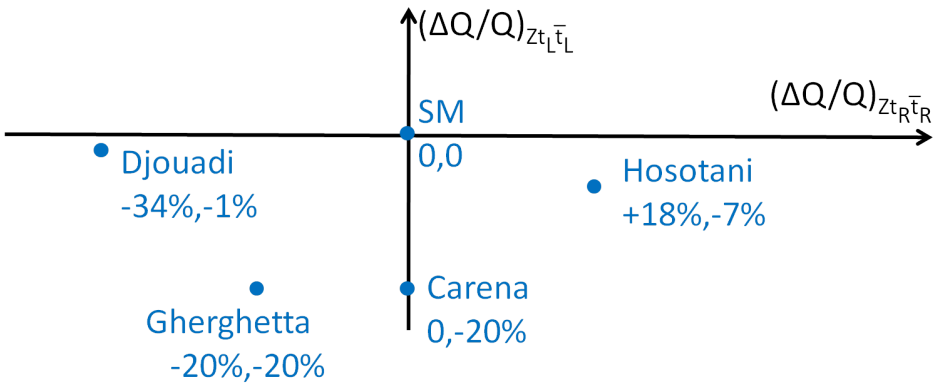

Figure 7.3: The relative deviations of $Zt_L\bar{t}_L$ and $Zt_R\bar{t}_R$ couplings in various realizations of a warped extra-dimension. The names refer to the references given in the text.

Chapter 8

Top study at the ILC

The large mass of the top quark is equivalent to a larger decay width and a short lifetime of about $0.5 \cdot 10^{-24}$ s. This suppresses hadronization before decay and therefore the spin information is preserved in its decay products [B$^+$86, SP92]. It decays dominantly via $t \to bW^+$. The pair production process $e^+e^- \to t\bar{t}$ thus lead to three final states: the full hadronic (46.2%) where the two W bosons decay into jets, the semileptonic (43.5%) where one W decays into jets and the other into a charged lepton and a neutrino, and the full leptonic (10.3%) where both W bosons decay into leptons. The top quark production cross-sections along with its backgrounds are presented in Sec. 8.1.

The final states in the detector are thus six jets including two b jets (jets originating from a bottom quarks) in the full hadronic channel, four jets including two b jets, one charged lepton and missing energy in the semileptonic channel, two b jets, two charged leptons and missing energy in the full leptonic channel. These complex final state of the top quark with jets and leptons provides an excellent benchmark to test the detector properties as well as theoretical models.

A detailed study of top pair production at the ILC reported a signal selection efficiency of 87.5% with a background rejection efficiency of 99.8% in the semileptonic decay channel and 91.7% signal selection efficiency with 99.4% background rejection efficiency in the full hadronic channel (see [Top]). The study used a multivariate likelihood method to select signal events and veto background ones. The main motivation was to measure the top mass, which was done after kinematic fitting.

The present study aims to derive the sensitivities to the $Zt_R\bar{t}_R$ and $Zt_L\bar{t}_L$ couplings via precision measurements of several observables that will be described Sec. 8.2 at the ILC with an energy in the center-of-mass $\sqrt{s} = 500\,\text{GeV}$ and an integrated luminosity $\mathcal{L} = 500\,\text{fb}^{-1}$. It is driven by the extra-dimensional models presented in Chap. 7 which foresee large deviations of their values $Q_Z^{t_R}$ and $Q_Z^{t_L}$.

8.1 Cross-sections for the top study

For a given polarization of the electrons (P) and the positrons (P'), the cross-section of any channel at the ILC reads [MPAA$^+$08]:

$$\begin{aligned}\sigma_{P,P'} = \; & \frac{1}{4}[(1+P)(1+P')\sigma_{R,R} + (1-P)(1+P')\sigma_{L,R} \\ & +(1-P)(1-P')\sigma_{L,L} + (1+P)(1-P')\sigma_{R,L}]\end{aligned} \tag{8.1}$$

with the notations R/L for +/- 100% longitudinally polarised electrons or positrons. A null polarisation thus stands for unpolarised beams.

In the limit $m_e/E \to 0$, valid here since $E = 250\,\text{GeV}$, $\sigma_{L,L} = \sigma_{R,R} = 0$ at tree level: $e^-_L e^+_L$ and $e^-_R e^+_R$ do not couple to photons and Z bosons due to helicity conservation. The cross-section reduces to:

$$\sigma_{P,P'} = \frac{1}{4}\left[(1-PP')(\sigma_{L,R}+\sigma_{R,L}) + (P-P')(\sigma_{R,L}-\sigma_{L,R})\right] \tag{8.2}$$

Two polarization states are needed to measure the cross-sections $\sigma_{L,R}$ and $\sigma_{R,L}$. The two configuration could equally share the luminosity while leading to larger statistics as far as statistical errors are concerned. The one with a predominantly left-handed electron and a right-handed positron (-|P|,|P'|) and the opposite (|P|,-|P'|) are preferred.

8.1.1 Top quark differential cross-section

The scattering angle θ is defined with respect to the direction of the initial electron and that of the top quark produced. For a given polarization, the differential top production cross-section in the center-of-mass frame reads, using 8.2 and [PS96]:

$$\begin{aligned}\left(\frac{d\sigma(e^-e^+ \to t\bar{t})}{d\cos\theta}\right)_{P,P'} = & \left(\frac{3\pi\alpha^2}{2s}\beta\right) \times \\ & \{(1-PP')\left[Q_1(1+\beta^2\cos^2\theta) + Q_2(1-\beta^2) + Q_3(2\beta\cos\theta)\right] \\ & + (P-P')\left[Q'_1(1+\beta^2\cos^2\theta) + Q'_2(1-\beta^2) + Q'_3(2\beta\cos\theta)\right]\}\end{aligned} \tag{8.3}$$

where β is the top velocity, $\sqrt{s}$ is the energy in the center-of-mass frame, and the $Q_i^{(\prime)}$ quantities are defined by:

$$\begin{aligned} Q_1^{(\prime)} &= \tfrac{1}{4}\left\{\left[|Q_{RR}|^2 + |Q_{RL}|^2\right] + (-)\left[|Q_{LR}|^2 + |Q_{LL}|^2\right]\right\} \\ Q_2^{(\prime)} &= \tfrac{1}{2}\mathcal{R}e\left[Q_{RR}Q^*_{RL} + (-)Q_{LR}Q^*_{LL}\right] \\ Q_3^{(\prime)} &= \tfrac{1}{4}\left\{\left[|Q_{RR}|^2 - |Q_{RL}|^2\right] + (-)\left[|Q_{LR}|^2 + |Q_{LL}|^2\right]\right\} \end{aligned} \tag{8.4}$$

and

$$\begin{aligned} Q_{IJ} &= Q^e_\gamma Q^t_\gamma + \frac{Q^{e_I}_Z Q^{t_J}_Z}{\sin^2\theta_W\cos^2\theta_W}\frac{s}{(s-M_Z^2)+iM_Z\Gamma_Z} \quad \text{(I,J = R,L)} \\ Q^t_\gamma &= Q^t = \tfrac{2}{3} \quad \text{(electric charge of the top quark)} \\ Q_Z^{t_{L/R}} &= I_3^L - Q^t\sin^2\theta_W \text{ (with } I_3^L = \tfrac{1}{2}/0 \text{ for a left/right-handed top quark)} \end{aligned} \tag{8.5}$$

The focus is here on the couplings of the Z boson to a right/left-handed top and left/right-handed anti-top $Q_Z^{t_{R/L}}$ defined in 8.5 which are the same than in Chap. 7.

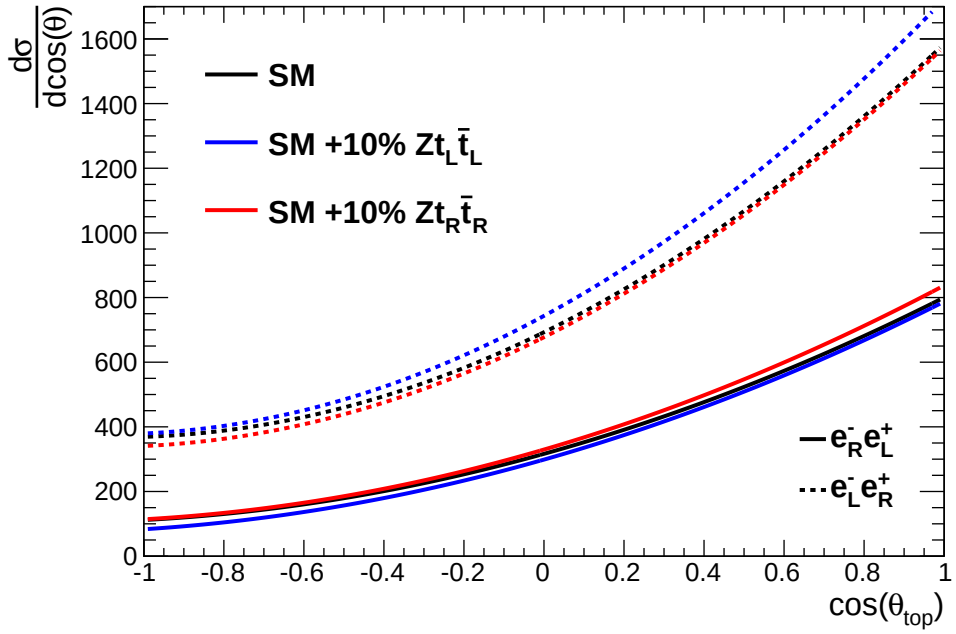

Figure 8.1: Differential cross-section of top production with fully polarized electrons and positrons at $\sqrt{s} = 500\,\text{GeV}$. The polar angle θ is defined between the top quark and the electron beam direction in the center-of-mass frame. The SM (black) is shown along with scenarios with $\Delta Q_Z^{t_L}/Q_Z^{t_L} = +10\%$ (blue) and $\Delta Q_Z^{t_R}/Q_Z^{t_R} = +10\%$ (red).

These quantities can be varied and the resulting differential cross-sections are shown in Fig. 8.1 as a function of the polar angle θ of the top quark, as given by Eq. 8.3.

It suggests that the top forward region, i.e. where $\cos\theta_{\text{top}} > 0$, is sensitive to the $Zt_L\bar{t}_L$ coupling in the case of an incident beam with left-handed electrons and right-handed positrons. A set of meaningful observables for the study of the Z to top couplings is discussed in Sec. 8.2.

8.1.2 Highest cross-sections at the ILC

The unpolarized cross-section for standard model processes are shown Fig. 8.2. The values of relevant processes at tree-level are summarized in Table 8.1 comprising also the fully polarized cross-sections with the resulting left-right asymmetry A^0_{LR}.[1] For a given process, this polarized asymmetry A^0_{LR} with 100% polarisations is defined by:

$$A^0_{LR} = \frac{\sigma_{L,R} - \sigma_{R,L}}{\sigma_{L,R} + \sigma_{R,L}} \tag{8.6}$$

1. An $e^-_L e^+_R$ configuration corresponds to P=-1,P'=+1, i.e. $\sigma_{L,R}$ and $e^-_R e^+_L$ to P=+1,P'=-1, i.e. $\sigma_{R,L}$.

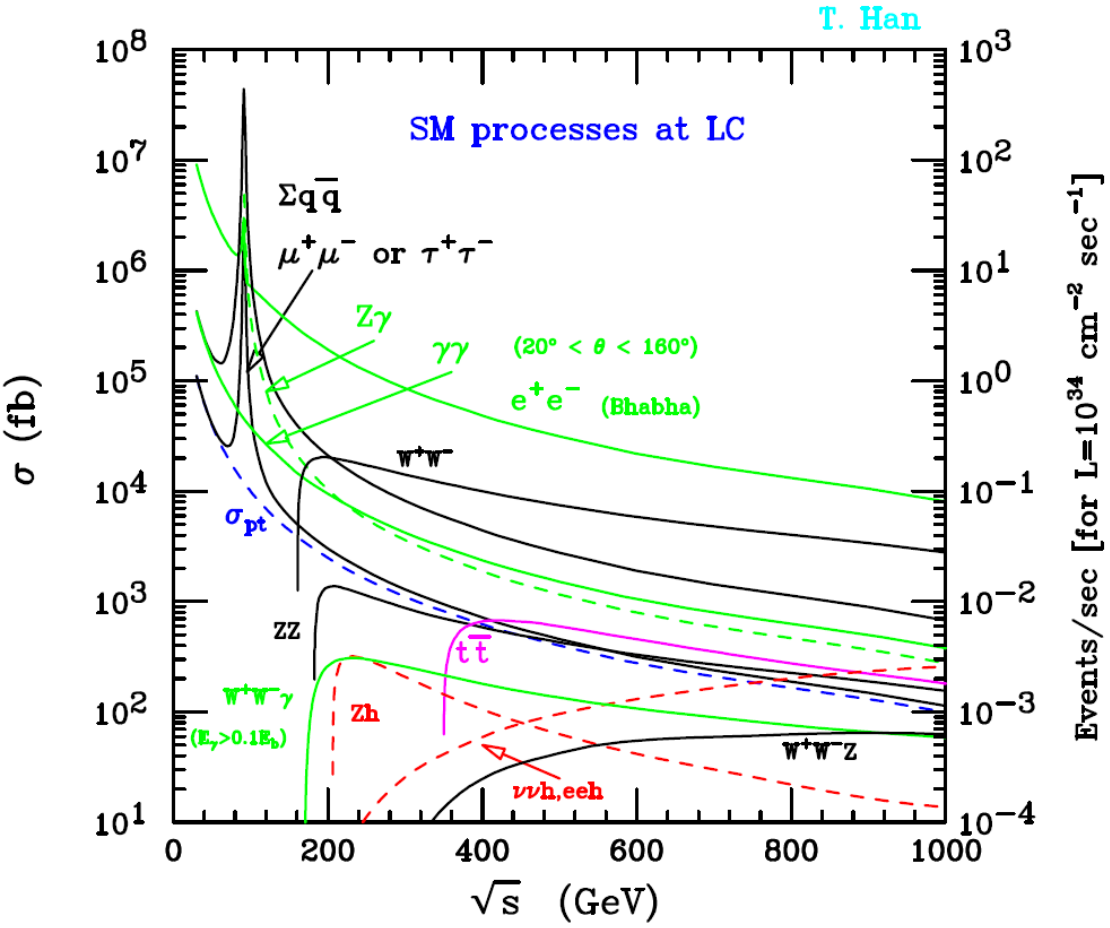

Figure 8.2: Cross-sections of SM processes at the linear collider as a function of the energy in the center-of-mass $\sqrt{s}$ of the e^+e^- pair. Picture taken from [Han06].

The left-right asymmetries are very contrasted from one process to another i.e. the cross-sections with one configuration of the polarizations are not in the same ratio in the opposite configuration. As a consequence, when studying the top quark production, the contamination of each background will be different, depending on the initial polarizations.

8.1.3 Event generation

To simulate the SM processes mentioned above, the Whizard event generator is used [Whi, KOR07, Ohl00]. It computes tree-level matrix elements and after integration and evaluation of all observables generates events to be used in the detector simulation. It treats the polarization in initial and final states.

The hadronization process is done by Pythia 6.205 [SLM01, Pyt] and the full simu-

Channel	Unpolarized (fb)	$e^-_L e^+_R$ (fb)	$e^-_R e^+_L$ (fb)	A^0_{LR} (%)
$\mu\mu$	456	969	854	6.3
uu+cc+ss+dd	2208	6032	2793	36.7
$t\bar{t}$	572	1564	724	36.7
$b\bar{b}$	372	1212	276	62.9
Zγ	11185	25500	19126	14.2
WW	6603	26000	150	98.8
ZZ	422	1106	582	31.0
ZWW	40	151	8.7	89
ZZZ	1.1	3.2	1.22	45

Table 8.1: Unpolarized and 100% polarised cross-sections of the main channels at the ILC with their corresponding left-right asymmetry A^0_{LR}. Figures are given at $\sqrt{s} = 500\,\text{GeV}$. [Ric]

lation is done within the Mokka framework (see also 4.2).

Whizard deals with multi-fermionic process. Processes leading to the same final states are summed up. Top quarks, W or Z bosons are not explicit in the final states of Whizard. But leptons and the five other quarks are present in the final states.

The top quark decays will be of the form $bl\nu$, with $l = e, \mu, \tau$ or bqq' with $q, q' = u, d, s, c$.[2] ZWW with $Z \to b\bar{b}$ is actually the major background for top pair production and its unpolarized cross-section is about 1% that of the top (see figures Table 8.1). This final state cannot be distinguished from those of the top quarks since both are the same at the parton level thus generated the same way by Whizard.

To distinguish among them, a cut is proposed at the parton level to check the consistency with the expected cross-sections of ZWW. The reconstruction at the parton level of the two top masses is shown Fig. 8.3(a) and the invariant $b\bar{b}$ mass after selection cuts is shown in Fig. 8.3(b) for an $e^-_L e^+_R$ configuration.

The top pair events are selected either by a square cut on the two top masses at $5\,\Gamma_{\text{top}}$, or by a combined cut on the distance to the two top masses at $15\,\Gamma_{\text{top}}$. It is summarized in:

$$\begin{array}{ll} & |M(bqq') - M_{\text{top}}| < 5\,\Gamma_{\text{top}} \\ \text{or} & |M(bl\nu) - M_{\text{top}}| < 5\,\Gamma_{\text{top}} \\ \text{or} & \sqrt{(M(bqq') - M_{\text{top}})^2 + (M(bl\nu) - M_{\text{top}})^2} < 15\,\Gamma_{\text{top}} \end{array} \tag{8.7}$$

where M_{top} =174 GeV and Γ_{top} =1.51 GeV. This cut selects the regions with the most prominent number of events.

As a cross-check, the ZWW background clearly shows the Z mass peak in Fig. 8.3(b), proving that the interference term between both channels is negligible. The ratio of separated ZWW events and selected $t\bar{t}$ events is 1.6%, compatible with the expected ratio from Table 8.1 of 1.4% for an $e^-_L e^+_R$ configuration.

2. The bars for antiparticles will not be added from now unless being needed for comprehension.

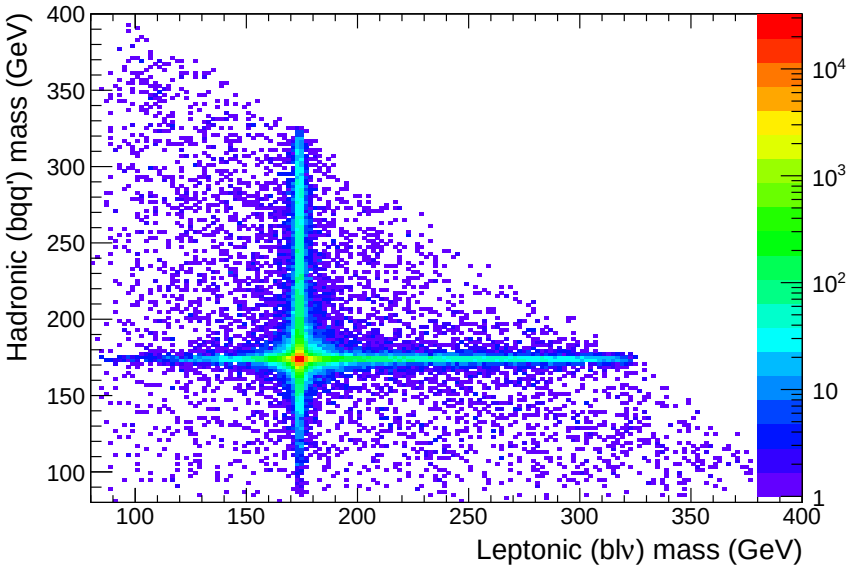

(a) Top masses at the partonic level : $M(bqq')$ vs $M(bl\nu)$. The peaks and tails of the top quarks can be identified and events outside are selected to be ZWW events.

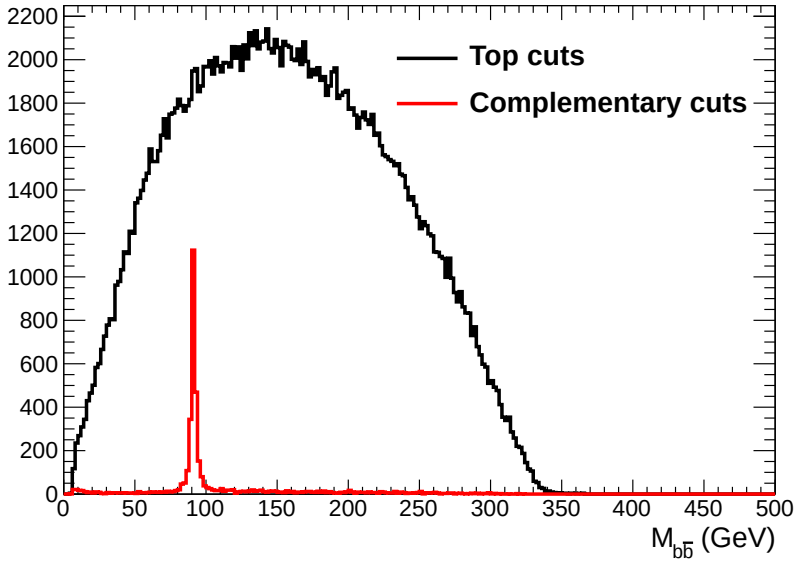

(b) Invariant $b\bar{b}$ mass at the partonic level after ZWW cuts. ZWW is well controlled by seeing the mass peak of the Z boson.

Figure 8.3: Variables used to discriminate at the parton level $tt \to bqq'bl\nu$ and $ZWW \to bbqq'l\nu$.

Since the left-right asymmetry is different between the top channels and ZWW, the only solution left here is to subtract in the end the contribution of this background in order to recover the desired asymmetry.

8.2 Experimental measurements

The semileptonic decay mode of the top pair is of interest because of its large fraction of 43.5% of total top events and the unambiguous determination of the charges. A schematic view of this process is shown Fig. 8.4. The W from the first top (t_1) decays into a lepton l and a neutrino ν via $t_1 \to b_1 W_1 \to b_1 l\nu$. The second top ($t_2$) decays hadronically $t_2 \to b_2 W_2 \to b_2 q\bar{q}'$. Since the lepton l carries the charge of W_1, the charge of t_1 is of the same sign. Which means that $Q(t_2) = \frac{2}{3}Q(l)$. During the study, it has been proved that the sign error on such reconstructed lepton is smaller than 0.1%. Hence t_2 can always be distinguished between a top and an anti-top quark. If one assumes charge conservation, there is no ambiguity on the charge of t_2.

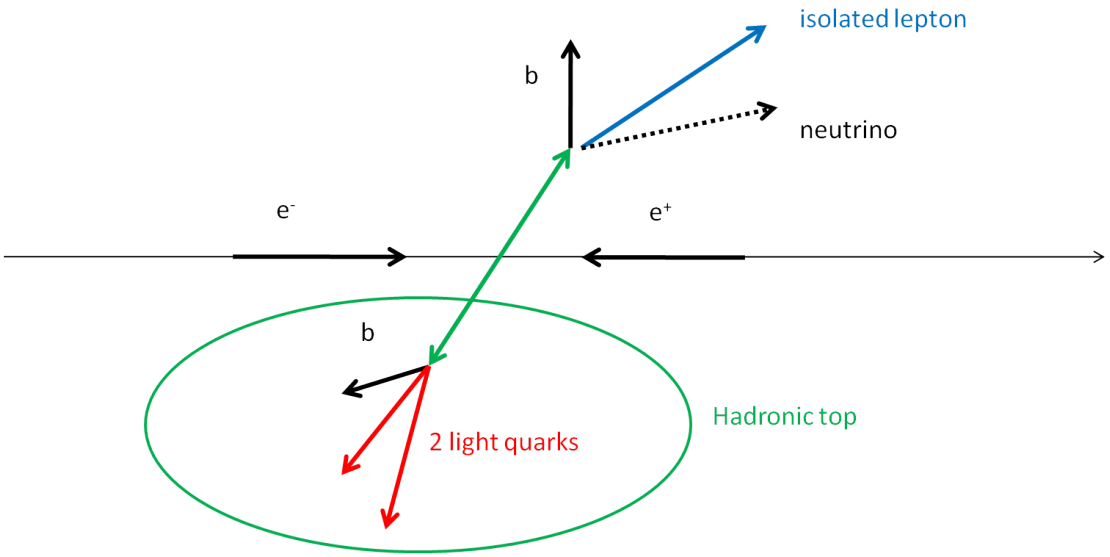

Figure 8.4: Picture of the semileptonic top decay. The strategy proposed is to reconstruct the hadronically decaying top quark and use the lepton to know its charge.

The event structure is the following: one lepton and four jets, out of which two are b jets and the two others come from a W.

Note that in the following study, only electron and muon channels will be considered as a signal for semileptonic top decays. The tau channel is left for future studies but with around 35% branching ratio to final states with electrons and muons, several events will be added to the previously defined signal. Taking this into consideration, the measurable fraction of top pair events in this analysis is rather 34% of the total top pairs produced.

8.2.1 Observables of interest

The favored observables for the top pairs are their left-right polarization asymmetry $A_{LR}^{0,t}$ and forward-backward asymmetry A_{FB}^{t}. The polarized asymmetry A_{LR}^{t} can be measured using all the decay channels of the top quark, while the forward-backward asymmetry A_{FB}^{t} requires the knowledge of the charge of the top quark. This study is made only for the semileptonic final state.

Left-right asymmetry A_{LR}^{t} The use of polarized electron beams allows to measure the polarized asymmetry of a process. A general expression for this asymmetry A_{LR}^{t} with the polarizations P and P' is:

$$\begin{aligned} A_{LR}^{t} &= \frac{\sigma_{-|P|,|P'|} - \sigma_{|P|,-|P'|}}{\sigma_{-|P|,|P'|} + \sigma_{|P|,-|P'|}} \\ &= P_{\text{eff}}\, A_{LR}^{0,t} \end{aligned} \tag{8.8}$$

It is related to the left-right asymmetry with 100% polarised beams for top pair events, $A_{LR}^{0,t}$, as defined in 8.6 and the quantity $P_{\text{eff}} = (|P| + |P'|)/(1 + |P||P'|)$ which is called the effective polarisation. In the best case, where $|P| = |P'| = 100\%$, the left-right asymmetry $A_{LR}^{0,t}$ is recovered.

Note that the statistical uncertainty on such an asymmetry A measured with a total of N events is given by:

$$\Delta A = \sqrt{\frac{1 - A^2}{N}} \tag{8.9}$$

where the number of measured events N with the polarizations P and P' is related to the number of events N^0 in the ideal case where $|P| = |P'| = 100\%$ by $N = N^0(1 + |P||P'|)/2$.

The precision on $A_{LR}^{0,t}$ in 8.8 not only will be given by that of A_{LR}^{t} but it is also dependent on the precision on P_{eff} via:

$$\left(\frac{\Delta A_{LR}^{0,t}}{A_{LR}^{0,t}}\right)^2 = \left(\frac{\Delta A_{LR}^{t}}{A_{LR}^{t}}\right)^2 + \left(\frac{\Delta P_{\text{eff}}}{P_{\text{eff}}}\right)^2 \tag{8.10}$$

where the independence between the measurement of A_{LR}^{t} done with top pair events and P_{eff} done with polarimeters and refined by W pair events ensures the quadratic sum between both relative uncertainties.

Using previous results of [AAA$^+$10, Top] mentioned in the introduction of this chapter, the relative uncertainty on the measured left-right asymmetry can be as good as 0.4%. This requires that $\Delta P_{\text{eff}}/P_{\text{eff}} < 0.2\%$, in order not to be affected by this uncertainty.

Forward-backward asymmetry A^t_{FB} The forward-backward asymmetry for the process $e^+e^- \to t\bar{t}$, A^t_{FB}, is defined by:

$$A^t_{FB} = \frac{\sigma(\cos\theta_t > 0) - \sigma(\cos\theta_t < 0)}{\sigma(\cos\theta_t > 0) + \sigma(\cos\theta_t < 0)} \tag{8.11}$$

with θ_t the top polar angle with respect to the initial direction of the electron and $\sigma(\cos\theta_t \lessgtr 0) = \int_{\cos\theta_t \lessgtr 0} \frac{d\sigma(e^-e^+ \to t\bar{t})}{d\cos\theta_t} d\cos\theta_t$ where the sum has been made over the two configurations of polarization.

This requires that the charge of the top quark be known. In this process involving only two particles in the center-of-mass frame, a forward anti-top $\bar{t}$ (with $\cos\theta_{\bar{t}} > 0$) will contribute to the backward part ($\cos\theta_t < 0$). In this study, this charge is deduced from that of the lepton of the semileptonic decay of the top pair.

If an equal luminosity is spent in the configurations $(|P|, -|P'|)$ and $(-|P|, |P'|)$, the forward-backward asymmetry is independent of the polarization (by computing it with Eq. 8.3, the factors $(1 - PP')$ vanish), only the number of measured events will differ as for A^t_{LR}. This asymmetry was already estimated in [AAA$^+$10, Top], using the full hadronic decay channel, where the charge of the top was given by that of one b jet. The result is $A^t_{FB} = 0.334 \pm 0.0079$, that is, a 2% relative uncertainty. However, the efficiency of charge identification of a b jet is 28% with a 75% purity, while the misidentification of the charge of a lepton is less than 0.1% with an efficiency better than 85% as will be shown in this study.

Another possibility is to use polarized forward-backward asymmetries, i.e. forward-backward asymmetries measured in both configurations of polarization: A^t_{FB,e_R} when the electron beam is mostly right-handed (P>0) and A^t_{FB,e_L} when it is mostly left-handed. 2% relative uncertainties were found for both polarised asymmetries in [DNP10] but this uses the charge identification of the b jet too. Using the semileptonic final state to deduce the charge of the top quark is an advantage compared to these methods, and can lead to a relative precision of 0.5%.

8.2.2 Expected sensitivities of the observables

The relative sensitivities are linearized with small values of the deviation of the Z to left and right-handed top quark couplings $\Delta Q_Z^{t_{R/L}}/Q_Z^{t_{R/L}}$ and given in Eq. 8.12. These sensitivities are derived from formulas 8.3 and 8.4.

$$\begin{aligned} \Delta A^{0,t}_{LR}/A^{0,t}_{LR} &= 1.43(\Delta Q_Z^{t_L}/Q_Z^{t_L}) - 0.74(\Delta Q_Z^{t_R}/Q_Z^{t_R}) \\ \Delta A^t_{FB}/A^t_{FB} &= 0.39(\Delta Q_Z^{t_L}/Q_Z^{t_L}) + 0.29(\Delta Q_Z^{t_R}/Q_Z^{t_R}) \end{aligned} \tag{8.12}$$

Using the actual values of $\Delta A_{LR}/A_{LR} \approx 0.4\%$ and $\Delta A^t_{FB}/A^t_{FB} \approx 2\%$, one could reach precisions of 2.2% on $\Delta Q_Z^{t_L}/Q_Z^{t_L}$ and 3.9% on $\Delta Q_Z^{t_R}/Q_Z^{t_R}$, mainly limited by the uncertainty on the forward-backward asymmetry. The aim of this study is to improve this uncertainty by relying on the semileptonic final state of the top quark pairs.

8.2.3 Complementary observables from the lepton

In addition to the top quark angular distribution, one can use its decay products and, e.g. define asymmetries with leptons either in the top rest system or in the laboratory system. It has been shown [PR96a, PR00, PR96b, Rin00, GRS06] that energy and angular distributions of this lepton can give a direct access to anomalous tbW vertex and CP violation in the production process. It is interesting in the context of top measurement since it does not require to reconstruct the top quark, only the lepton, which is much simpler, efficient and less contaminated.

A quantity of interest is the lepton forward-backward asymmetry A^l_{FB}, defined in as in Eq. 8.11 with now the forward ($\cos\theta_l > 0$) and backward ($\cos\theta_l < 0$) regions defined for the polar angle of the lepton with respect to the direction of the initial electron.

On the course of this study, an other quantity became of interest:

$$D^l = \frac{\sigma^l_{F,e_R} - \sigma^l_{B,e_L}}{\sigma^l_{F,e_R} + \sigma^l_{B,e_L}} \tag{8.13}$$

It can be called the lepton disymmetry and relates changes in the forward region with right-handed electrons and in the backward region using left-handed electrons.

The sensitivities to these observables are derived from [PR96a].

$$\begin{array}{rcl} \Delta A^l_{FB}/A^l_{FB} & = & -0.99(\Delta Q^{t_L}_Z/Q^{t_L}_Z) + 1.70(\Delta Q^{t_R}_Z/Q^{t_R}_Z) \\ \Delta D^l/D^l & = & 2.44(\Delta Q^{t_L}_Z/Q^{t_L}_Z) - 1.64(\Delta Q^{t_R}_Z/Q^{t_R}_Z) \end{array} \tag{8.14}$$

All of these quantities have statistical uncertainties proportional to $1/\sqrt{N}$, where N is the total number of measured events. It is crucial in the following analysis to ensure a maximal selection efficiency of the signal.

8.2.4 Consideration of the backgrounds

The highest cross-sections of the physical processes at the ILC were given Sec. 8.1. In view of these figures and the topology of the semileptonic decay mode studied, preliminary considerations for the backgrounds can lead the next steps of the analysis.

Other top final states One of the main background to this top pair production analysis is the top itself in other decay modes. In particular if because of misidentification or contaminations in the lepton selection, some leptons are found and kept in the full hadronic final state.

This could be the case since typically around 10% of bottom mesons decay into a charged lepton plus additional particles. However they should be embedded in a jet rather than isolated like the lepton of the top decay.

Fully hadronic top decay modes constitute 46.2% of all top pair decay modes and it is thus of the same order than the semileptonic mode. Due to its very similar final state at the parton level, a non negligible fraction of this channel may enter the selections and bias the observables considered in this study.

The full leptonic decay channel of the top pairs is another major background for semileptonic studies. Indeed, one lepton can be found and enter the selections for the semileptonic top. Too much missing energy may be involved and it could be a way to reject these events, as well as finding incoherent W and top masses.

A problem will arise if the second lepton is a τ decaying hadronically, forming a jet structure. However it should be discriminated from a real jet for it contains fewer tracks.

W pairs The W pair background is 10 times larger than the top pair production. It is very forward peaked since it involves mainly a neutrino exchange in the t-channel. This process is to be checked carefully and strongly suppressed, since any contamination at the 1% level leads to 10% impurities in the top events selected.

Only its semileptonic final state contains a lepton from a W boson but this must be strongly reduced by the identification of b jets .

Negligible backgrounds As seen from Fig. 8.2, the processes involving a t-channel diagram are the largest cross-sections. In particular, the Bhabha scattering ($e^+e^- \to e^+e^-$) is two orders of magnitude above the top pair production. However, the topology of such events is rather simple and leads either to very forward electrons which may not be measured, or two energetic and well identified electrons.

The sum of all di-lepton channels is larger than the top pair production cross-section. However, the topology is again clearer: due to these highly energetic leptons, the events will appear as back-to-back di-jets. In the case of a gluon emission for quarks, the jets are still expected not to contain a lepton faking that of a W.

The cross-sections of Zγ and $\gamma\gamma$ channels are both up to 5 times larger than that of the top pair but should again lead to simpler topologies.

The ZZ background is comparable in cross-section with top pair events, but the major decay channel that can fake the top pair topology is: $e^+e^- \to ZZ \to b\bar{b}\tau^+\tau^-$, with one tau lepton decaying into jets and the other into leptons. The branching ratio of these processes is thus $Br(Z \to b\bar{b}) \times Br(Z \to \tau^+\tau^-) \times 2 \times Br(\tau \to \text{hadrons}) \times Br(\tau \to \text{leptons}) \approx 0.2\%$, which appears to be negligible at this level.

Finally, the ZWW background with $Z \to b\bar{b}$ was discussed above and is to be subtracted from the signal.

Chapter 9

Description of the International Large Detector

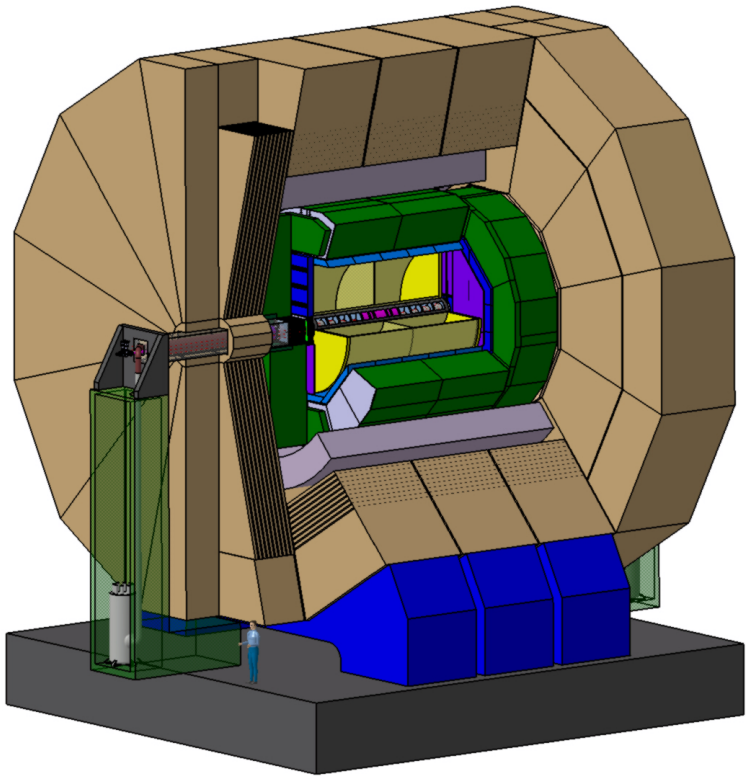

Figure 9.1: View of the ILD detector. At the center, the interaction region (red) surrounded by the tracking system (yellow). The ECAL (blue) and HCAL (green) are placed inside the coil (purple) and the iron (brown) ensures the return of the magnetic field. Picture taken from [AAA+10].

Physical processes called reference reactions have been defined by a worldwide study review [FPR] to be used as a basis for detector performance studies at a linear collider. In particular, studying the Higgs-strahlung process ($e^+e^- \to ZH$) as well as W and top pair production ($e^+e^- \to W^+W^-$, $e^+e^- \to t\bar{t}$) are recommended to guide the design of the detector. This chapter presents elements that drive the choices for the subdetector parameters for the International Linear Detector (ILD), starting from the description of the final states of these reference reactions.

9.1 Physics driven design

The reference reactions contain particles in the final state which stable decay product will give charged leptons, neutrinos and jets as a result of hadronic final states. Figures of the branching ratios of the Z and W bosons shown Table 9.1 indicate that jets (mostly two jets, "di-jets") are produced in almost 70% of the cases.

Particle	Decay mode	Branching ratio
t	bW	$\approx 100\%$
W	lν	10.80%
W	hadrons	67.60%
Z	l^+l^-	3.36%
Z	invisible	20.00%
Z	hadrons	69.91%

Table 9.1: Major branching ratios of the top quark, W and Z bosons [Nak10]. l indicates each type of lepton (e, μ, τ), not sum over them.

The jet energy resolution should be good enough to separate the hadronic decays of the W and Z bosons, which masses are close by 10 GeV. This will be done using the particle flow approach which will be described below and is an important challenge at the ILC. In addition, charged leptons are measured using the tracking systems. Final states containing neutrinos lead to missing energy. The detector has to be 4π-hermetic.

9.1.1 The particle flow technique

As pointed out above, 70% of the decays of the W and Z bosons lead to jets in the final state. The reconstruction of invariant di-jet masses is essential to identify them. The di-jet mass resolution should thus be comparable to their natural decay widths. This requires the jet energy resolution $\Delta E_{\text{jet}}/E_{\text{jet}}$ to be about 3-4% over the entire jet energy range above 45 GeV i.e. around $30\%/\sqrt{E_{\text{jet}}}$ for jet energies below 100 GeV. This is more than a factor of two with respect to LEP which achieved a resolution of about $60\%/\sqrt{E_{\text{jet}}}$.

Traditionally, the energy of a jet is measured by the calorimeters. However this energy can be decomposed into approximately 65% of contributions from charged particles, 26%

from photons and 9% from neutral hadrons. A fraction of around 1% of the energy can be carried by neutrinos present in jets from charm and bottom quarks but will not be discussed here. Moreover the tracking system which measures the momentum of charged particles is usually much more accurate than the energy measurement of the calorimeters. It is therefore more attractive to measure the majority of the energy carried by charged particles with the tracking system, while the calorimeters measure only the energy of neutral particles. This is the paradigm of particle flow.

To corroborate the previous assertion, we give an example of jet energy resolution. At the ILC, the requirement on jet energy resolution implies that the charged particles be measured in the tracker with a momentum resolution σ_{1/p_T} of about $2 \times 10^{-5}\,\mathrm{GeV}^{-1}$. The energy resolution of the calorimeters σ_E/E is expected to be better than $15\%/\sqrt{E}$ in the ECAL and better than $50\%/\sqrt{E}$ in the HCAL, with E in GeV.

Assuming these resolutions we want to show the impact on the jet energy resolution $\Delta E_{\mathrm{jet}}/E_{\mathrm{jet}}$. Following the previous prescription that charged (ch) tracks constitute 65% of the energy and are measured in the tracking system, while 26% energy contributions of photons (γ) and 9% of neutral hadrons (h^0) are measured in the ECAL and HCAL, this simple jet energy resolution reads:

$$\begin{aligned}(\Delta E_{\mathrm{jet}})^2 &= (\Delta E_{ch})^2 + (\Delta E_{\gamma})^2 + (\Delta E_{h^0})^2 \\ &\approx 4.5 \times 10^{-12} E_{jet}^4 + 30 \times 10^{-3} E_{jet}\end{aligned} \tag{9.1}$$

The numbers show that the jet energy resolution is dominated by the second term on the right-hand side coming from the calorimters up to several hundreds of GeV. Neglecting the first term coming from the tracking system, the jet energy resolution can be estimated:

$$\Delta E_{\mathrm{jet}}/E_{\mathrm{jet}} \sim \frac{17\%}{\sqrt{E\ (\mathrm{GeV})}} \tag{9.2}$$

The required precision is reached. With a perfect particle flow algorithm, each charged particle is reconstructed with the combination of a track and energy depositions in the calorimeters and the left ones come from neutral particles. To this aim the detector must be optimized for the separation the various energy depositions in the calorimeters.

The use of a strong magnetic field and a large radius is favored to separate depositions of charged particles from neutral ones. The calorimeters must be made of dense material to reduce the lateral size of the showers thus separate them best and prevent their overlapping. This geometric separation of the showers also requires a fine granularity of the calorimeters in order for dedicated algorithms to cluster unambiguously the contributions by energy deposition of all particles. A limiting factor of the particle flow, called "confusion", is due to overlapping showers [Tho09].

A realistic study as shown in [AAA$^+$10] leads to 3.8% jet energy resolution in the 40-400 GeV jet energy range. At the ILC with 500 GeV energy in the center-of-mass frame, typical jet energies are below 250 GeV. The jet energy resolution is $\Delta E_{\mathrm{jet}}/E_{\mathrm{jet}} < 3\%$ which reaches the goal set from the constraint to separate the W and Z bosons.

9.1.2 Flavor tagging

Another important challenge for an ILC detector is to tag heavy flavored jets. These jets are products of the decay followed by hadronization of a bottom or charmed meson, originating from a bottom or charm quark in the final state of the process. This so-called B and C tagging is crucial, especially in the context of top quark identification but also for Higgs decays ($H \to b\bar{b}$ and $H \to c\bar{c}$). Typical lifetimes τ of bottom or charmed mesons are of approximately 10^{-12} s ($c\tau \approx 300\,\mu m$). The decay products are thus displaced from the primary interaction point of the e^+e^- pair by several hundreds of μm. Finding the production and decay point is done by extrapolating charged tracks and defining vertexes from which several tracks emerge. The so-called primary vertex, that is the primary interaction point, is usually the one from which the majority of tracks emerge. In establishing whether a track comes from it, one defines an impact parameter which is the distance of closest approach of the track and the primary vertex. If the impact parameter is significantly larger than its experimental resolution, a secondary vertex is created and the distance between production and decay points can be deduced. This measurement is essential to tag heavy flavored jets and used in combination with other variables of the jet [XHJHD01, Haw]. Reconstructing the charge of the bottom meson is also a goal of the detector but not for this study. It has been used for instance in [Top, DNP10].

9.2 Choice for the subdetectors

The ILD is a detector which fulfills the previous requirements. To reach a maximal angular coverage, the detector is composed of a central region (barrel) and endcaps which are instrumented by forward devices. It is shown Fig. 9.1 and in the lateral quadrant Fig. 9.2 with its principal subdetectors.

- The vertex detector is a multi-layer (three double layers) Si-pixel detector to measure the impact parameters. The figure of merit to reconstruct the primary, secondary and even tertiary vertexes of a decay chain is the impact parameter resolution. Its resolution goal is $\sigma_{IP} = 5\,\mu m \oplus \frac{10}{p(\mathrm{GeV})\sin^k\theta}\,\mu m$, where $k = 3/2$ for the $r-\phi$ and $k = 5/2$ for the $r-z$ projection [Bat10]. The first term in the resolution is the asymptotic impact parameter resolution which depends on the radii of the inner and outer layers and the single point resolution. The second term comes from multiple scattering due to the material traversed by the particles, where the material budget between the interaction point and the first measured point is expected to be a few per-mil of radiation length (the double ladders account for $0.16\%\,X_0$). The first layer of the vertex detector should be as close as possible to the interaction point: fixed on the beampipe. The radius of the beampipe is of 14.5 mm with the first layer fixed at 16 mm.
- The main tracker is a time projection chamber (TPC) which allows for redundancy in measuring the tracks: up to 224 points per track. To ensure full hermiticity for track reconstruction, inner and outer Si-strip tracking layers are located at the

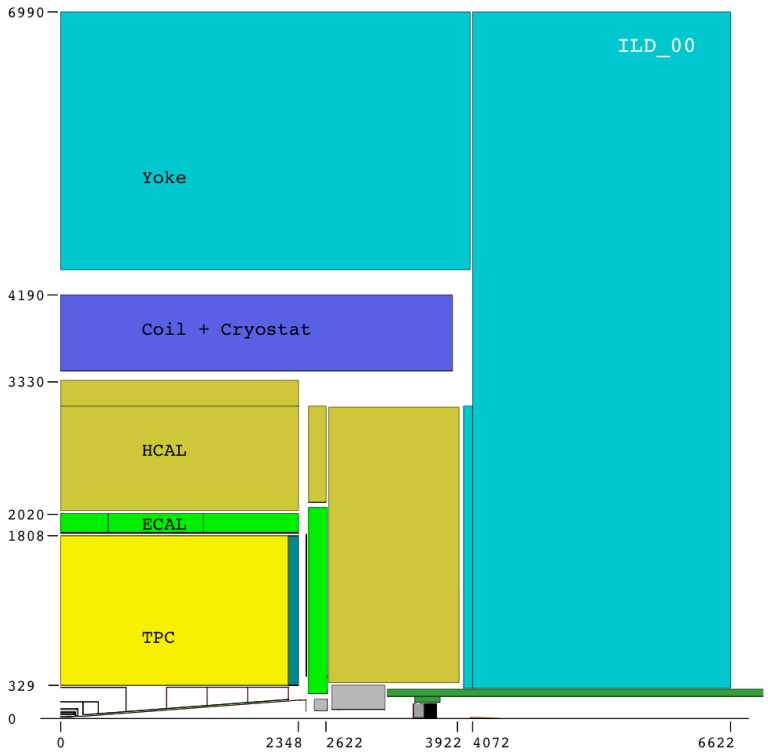

Figure 9.2: Lateral view (quadrant) of the ILD detector. Figure taken from [AAA+10]

borders of the TPC (SIT, SET, ETD) as well as a forward tracking device (FTD) made of Si-pixel and Si-strip disks. Reconstructing a track is thus possible down to polar angles of about 7°, as shown Fig. 9.3. The momentum resolution of a track can be as good as $\sigma_{1/p_T} \approx 2 \times 10^{-5}\,\mathrm{GeV}^{-1}$ by combining the TPC and all Si tracking devices.

– The electromagnetic and hadronic calorimeters are placed inside the magnet surrounding the detector which provides an axial magnetic field of 3.5 T. The calorimeters need a high granularity, the one used in this thesis is that of the ILD baseline: $0.5 \times 0.5\,\mathrm{cm}^2$ for the transverse cell size of the ECAL and $3 \times 3\,\mathrm{cm}^2$ for the HCAL. They are also segmented in depth of 30 layers for the ECAL and 48 layers for the HCAL.
– Other very forward calorimeters (LumiCAL, BCAL, LHCAL) extend the coverage of the detector to almost 4π and measure the luminosity and quality of the colliding beams.

As discussed above, the physics has driven the choices of parameters for the subdetector systems. It was also the case for the main geometrical parameters of the ILD that have been selected on a performance basis of the Pandora Particle Flow Algorithm [Tho09] (PandoraPFA) in the ILD Letter Of Intent [AAA+10]. They are summarized in Table 9.2.

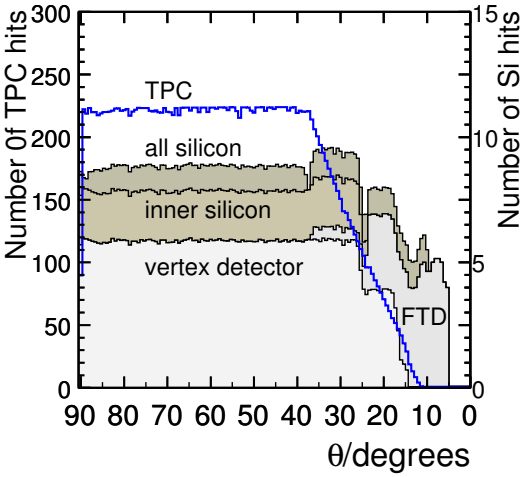

Figure 9.3: Average tracker hits for simulated tracks in the ILD detector as a function of the polar angle θ. Figure taken from [AAA+10]

B field (T)		3.5
Beampipe R_{min}		14.5
Vertex Detector	Geometry	ladders
	Layers	3 doublets
	R_{min}	16.0
Barrel SIT	Layers	2 cylinders
	Radii	165, 309
TPC drift region	R_{min}	395
	R_{max}	1739
	z_{max}	2247.5
TPC pad rows		224
ECAL barrel	R_{min}	1847.4
	Layers	20+9
	Total X_0	23.6
ECAL endcap z_{min}		2450
HCAL barrel	Layers	48
	R_{max}	3330
λ_{int} (ECAL+HCAL)		6.86

Table 9.2: *The geometrical parameters of the ILD detector used. Distances are shown in units of mm.*

Chapter 10

Detector studies

This chapter reviews important performances of the detector regarding top pair production at the ILC. The study of this thesis concerns mainly semileptonic top decays. Emphasis is put here on the performances of B tagging, tracking of leptons and a hermetic detector.

In all the following study, the simulated samples used are those used for the Letter Of Intent of the ILD. After event generation in Whizard, the full simulation of the response of the detector is done with Mokka. Particles are reconstructed using the Pandora PFA algorithm [Tho09] as "particle flow objects". Jets are reconstructed by using the Durham algorithm for jet clustering [CDO+91].

10.1 B tagging

Identifying a top event relies mainly on the presence of bottom hadrons. An algorithm of B tagging is used event per event to tag jets originating from bottom hadrons. B tagging at the ILC is done by the LCFIVertex algorithm [BDG+09]. The B tag value is the output of a neural network and is attached to a jet. It takes a value between 0 and 1, and is the likeness of the jet to originate from a bottom hadron.

To calculate the B tag value of a jet, it is necessary to reconstruct its vertex of origin. For bottom mesons, this will correspond to a secondary vertex with respect to the vertex of primary interaction and their decay length can be deduced. The neural network which calculates the B tag value uses a set of variables defined in [Haw, XHJHD01]. Two powerful inputs, apart from the decay length, are the joint likelihood in the $r-\phi$ and $r-z$ projections, for all tracks in the jet to have originated from the primary vertex. They depend on the respective significances of the impact parameters in $r-\phi$ and $r-z$ of all tracks in the jet. The resolution of the impact parameter pointed out Chap. 9 is thus of crucial importance.

Additional tagging of charmed hadrons will not be considered in this analysis.

The neural network is trained on samples of $Z \to u\bar{u}, d\bar{d}, s\bar{s}, c\bar{c}$ for background and $Z \to b\bar{b}$ pairs for signal [Wal09]. This event structure is more simple than for top pair

events which feature more jets in their final state. For this case, a dedicated study has been done to understand the efficiency and the purity of the B tagging algorithm.

10.1.1 B tagging in a multi-jet environment: purity and efficiency

The process $e^+e^- \to t\bar{t}$ leads to a multi-jet final state. The semileptonic top decay channel contains four jets, out of which two are bottom jets. These jets should be identified with a large B tag value.

Using the Monte Carlo information, the reconstructed lepton of the semileptonic decay is subtracted from the simulated event. One is left with the hadronic decay products of the top pair. The Durham algorithm [CDO+91] is used to find four jets, the B tagging algorithm is applied and associates a B tag value to each jet, while information on the origin of the jet (bottom hadron or not) is kept to define efficiency and purity of the B tagging.

The reconstructed jets may be of two kinds "true b jet" or "light jet" depending if they originate from a bottom hadron or not. A "b jet" is defined if, given a cut on the B tag value $B_{\text{tag}}^{\text{cut}}$, its B tag value B_{tag} is larger than that (i.e. $B_{\text{tag}} > B_{\text{tag}}^{\text{cut}}$). The efficiency ϵ_b of the B tagging and contamination c_b by light jets are defined by:

$$\begin{array}{rcl} \epsilon_b & = & \frac{N_{\text{b jets}}}{N_{\text{true b jets}}} \\ c_b & = & \frac{N_{\text{light jets}}}{N_{\text{b jets}}} \end{array} \tag{10.1}$$

One could also use the purity $P_b = 1 - c_b$.

As in top pair decays, bottom quarks always come in pairs, only one jet with a large B tag value is enough to conclude that two true b jets are present. However, it has been shown during this study that using a combined requirement on the two highest B tag values increases the purity of the selected sample (see Chap. 11).

The jets with the highest and second highest B tag value have been checked. The performances of the B tagging is shown Fig. 10.1. Using a cut $B_{\text{tag1}}^{\text{cut}} = 0.8$, the efficiency is $\epsilon_{b1} = 86.2\%$ for the jet of highest B tag value with a contamination $c_{b1} = 0.7\%$. Using a cut $B_{\text{tag2}}^{\text{cut}} = 0.3$ for the second, the efficiency to retain a true b jet is $\epsilon_{b2} = 63.4\%$ with a contamination $c_{b2} = 6.2\%$ from light jets.

Candidate b jets are reconstructed isotropically as shown Fig. 10.2: the mean highest B tag value is 0.89 and the second highest is 0.54. This shows the quality of b jet reconstruction even at small polar angles.

10.1.2 Inefficiencies of the B tagging

The second highest B tag values are worse than the highest and show the limitations of the algorithm (0.54 in average and 0.89). Further investigation showed that 50.4% of true b jets with a decay length $d < 300\,\mu m$ have a B tag value $B_{\text{tag}} < 0.3$ as shown Fig. 10.3, which seems to be a limit of the detector coming from short traveling distances of the bottom mesons while only 17.0% of such bottom jets feature a B tag value $B_{\text{tag}} >$

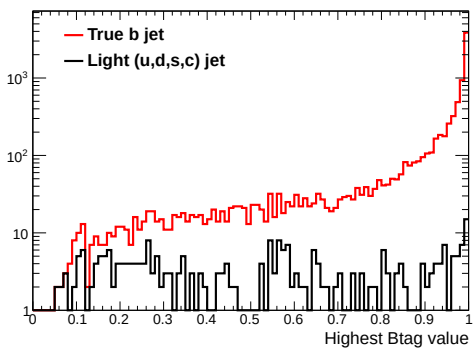

(a) Highest Btag found in each event.

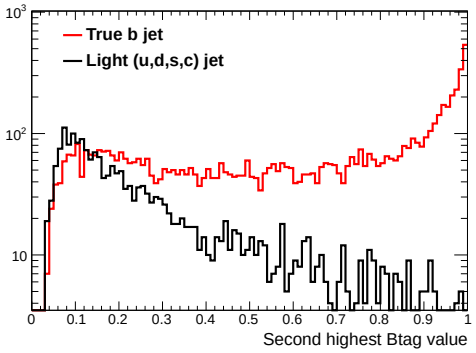

(b) Second highest Btag found in each event.

Figure 10.1: Distributions of the two highest B tag values among the four reconstructed jets in semileptonic top events. Contamination from light jets is 0.7% for the jt with highest B tag value, using $B_{\text{tag1}} > 0.8$. The jet with the second highest B tag value is contaminated by 6.2% of light jets for $B_{\text{tag2}} > 0.3$.

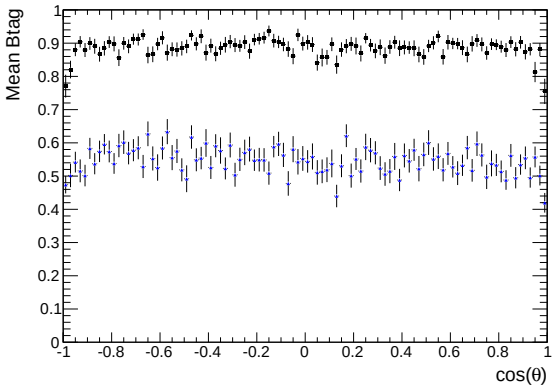

Figure 10.2: The angular distribution of the averaged highest B tag value and second highest B tag value.

0.8. The ideal case would be to have the first layer of the vertex detector as close as possible to the interaction point but it is limited to the size of the beampipe.

10.2 Tracking

The large tracker of the ILD is its TPC, as described Chap. 9. The TPC is a gaseous cylindrical detector, with at its end two anodes and a cathode in the central part to create an electric field inside the chamber. Charged particles passing through it ionize the medium and due to the electric field, electrons and ions migrate to the instrumented electrodes. This permits the reconstruction of charged tracks present in each event.

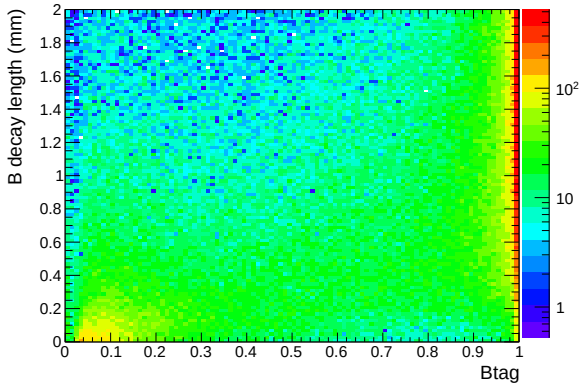

Figure 10.3: The second highest B tag value for true bottom jets with respect to the decay length of their originating hadron for values smaller than 2 mm. A large proportion of particles decaying early ($d < 0.3\,mm$) is badly tagged.

Since the tracking system is placed inside a coil producing a 3.5 T magnetic field along the longitudinal direction, particles will have a curved trajectory. Each track can thus be fitted by a helix to derive their momentum (it is rigorously a spiral since particles loose energy in the TPC but this effect is typically small and not yet taken into account in the fit). The most important parameters are the radius of curvature ω and the dip angle λ defined by the angle between the transverse plane and the momentum $\vec{p}$ of the particle (see [RCF] and [Krä06]).

$$p = \frac{Bq}{\omega}(1 + \tan^2 \lambda)^{1/2} \tag{10.2}$$

where B is the magnetic field and q is the electron charge magnitude, using $Bq = 1.05 \times 10^{-3}$, to express ω in mm and p in GeV.

The fit also gives the covariance matrix of all measured parameters of the spiral, in particular between ω and $\tan\lambda$. One can deduce the error on the momentum reconstruction using:

$$\left(\frac{\Delta p}{p}\right)^2 = \left(\frac{\Delta\omega}{\omega}\right)^2 + \left(\frac{\tan\lambda}{1+\tan^2\lambda}\right)^2 (\Delta\tan\lambda)^2 - \frac{2}{\omega}\frac{\tan\lambda}{1+\tan^2\lambda} Cov(\omega, \tan\lambda) \tag{10.3}$$

The requirements for the TPC were defined in terms of transverse momentum p_T, defined by $p_T = Bq/\omega$ with the corresponding error $(\Delta p/p)^2 = (\Delta\omega/\omega)^2$. The uncertainty on the transverse momentum of reconstructed tracks is shown Fig. 10.4 as a function of their momenta and of the angle. It is shown only for the reconstructed leptons in the semileptonic decay of the top quark.

Using the Monte Carlo information on the lepton from the semileptonic decay, it can be compared to its reconstructed track. The angular distribution Fig. 10.5 shows the ratio of reconstructed lepton tracks among all leptons. It features an average of 87% of

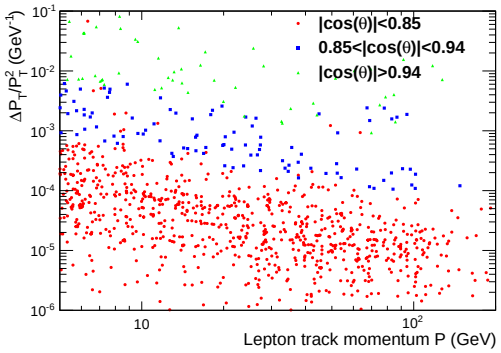

(a) Transverse momentum resolution as a function of the total momentum. Different angular parts of the detector are identified and agree with the precisions expected.

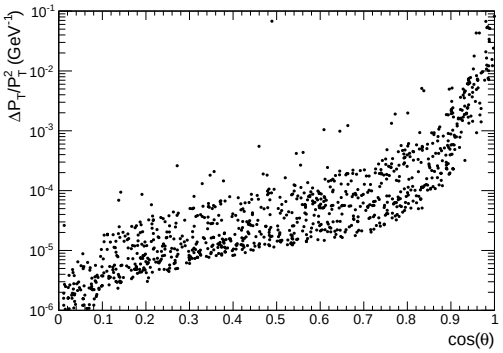

(b) Transverse momentum resolution as a function of the $cos(\theta)$ of the track. It degrades when the tracks are closer to the beam axis.

Figure 10.4: $\Delta p_T/p_T^2$ for lepton tracks using the whole tracking system. $|\cos\theta| < 0.85$ ($\theta \approx 31^\circ$) corresponds to the barrel region and includes all the tracking devices but the FTD, while $|\cos\theta| > 0.94$ ($\theta \approx 20^\circ$) includes mostly the FTD.

well reconstructed leptons. The very forward areas, at $|\cos(\theta)| > 0.98$ ($\theta \approx 11^\circ$), are less instrumented and lead to less measurements of the very forward tracks. The first and last bins of the graph thus show a 67% reconstruction efficiency.

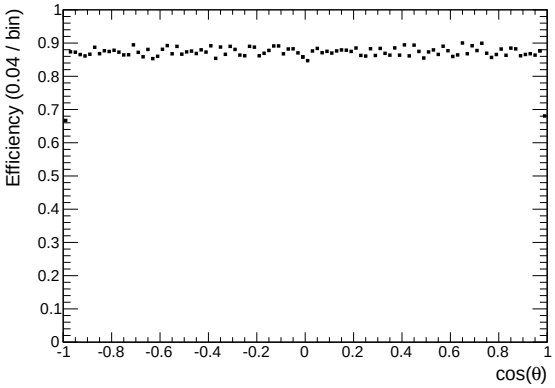

Figure 10.5: The angular dependence of the efficiency to reconstruct the lepton.

The detector is able to reconstruct almost isotropically charged leptons with the desired accuracy, as well as b jets, in the context of the semileptonic decay of top pairs.

Chapter 11

Reconstruction of the top quark from the semileptonic decay channel

The previous chapters introduced relevant observables for the study of the top quark, with particular focus on some Randall-Sundrum models. To identify semileptonic top decays, the two main ingredients are the B tagging and lepton reconstruction, which have been checked at the detector's level Chap. 10. We continue the analysis with a specific lepton identification that will be developed in Sec. 11.1. It is used for the reconstruction of semileptonic events from top pairs, and the measurement of the observables suggested Chap. 8 is given with particular emphasis on their uncertainty.

The strategy is to reconstruct the top which decays into hadrons. The charged lepton from the W which decays into leptons is identified, as well as two b jets out of the four jets. The two non-b jets will form the W which decayed into hadrons and a choice between two combinations has to be made between the two b jets to reconstruct the top quark. The sign of its charge is known, thanks to the lepton, and observables like the forward-backward asymmetry can be reconstructed.

11.1 Lepton identification

The first step is to identify charged leptons in each event. Each charged particle reconstructed by the particle flow algorithm consists of a track with momentum P and a cluster of deposited energy in the calorimeters E_{calo}. This energy can be divided in the one deposited in the ECAL E_{ecal} and the one deposited in the HCAL. Fig. 11.1 features the ratios E_{calo}/P and $E_{\text{ecal}}/E_{\text{calo}}$ for electrons (red), muons (blue) and other charged hadrons (particles are differentiated thanks to the Monte Carlo). It shows that muons and electrons cover different regions in contrast to the other particles. This suggests the following cuts to identify them.

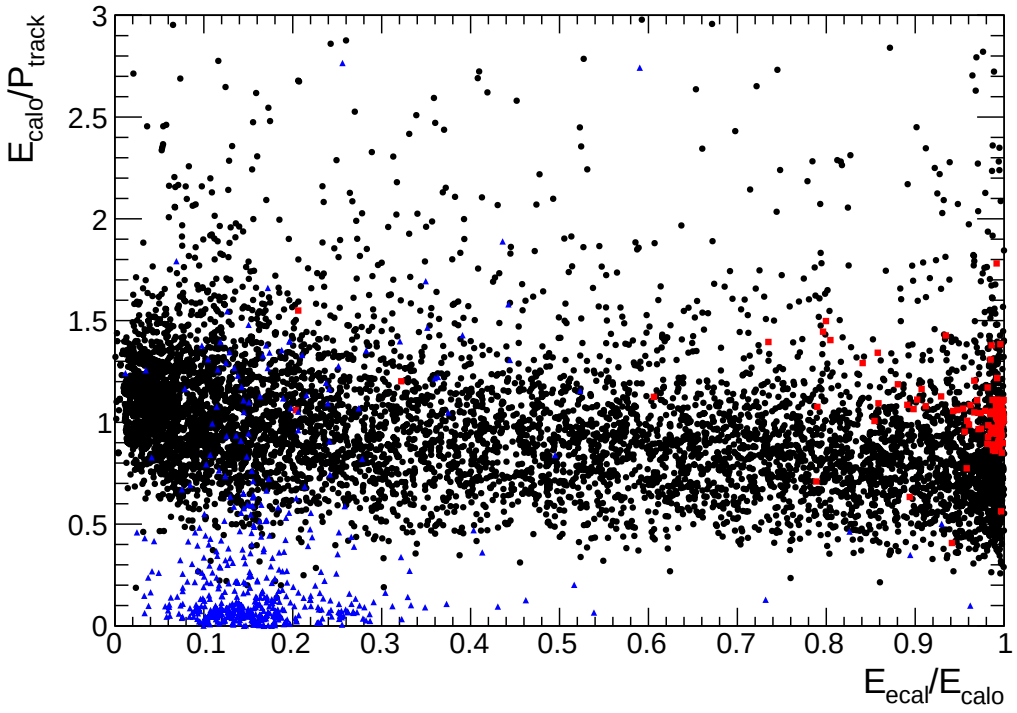

Figure 11.1: Energies and momenta of reconstructed objects in $E_{\text{calo}}/P_{\text{track}}$ vs $E_{\text{ecal}}/E_{\text{calo}}$ view. Real electrons (red) and muons (blue) are visualized among other particles which are charged hadrons (black).

A muon (blue in Fig. 11.1) is defined by:

$$E_{\text{calo}}/P < 0.5 \tag{11.1}$$

An electron (red in Fig. 11.1) is defined by:

$$E_{\text{calo}}/P < 0.8 \text{ and } E_{\text{ecal}}/E_{\text{calo}} > 0.9 \tag{11.2}$$

11.1.1 Isolation method

Once charged leptons have been identified in an event, the lepton from the decay of the W boson has to be selected. Only charged leptons with an energy larger than 5 GeV are kept in the following. The fraction of rejected signal events is indeed less than 1% for both electron and muon channels with this cut. It does not alter significantly the spectrum of these leptons as shown Fig. 11.5.

The charged lepton in the final state of a semileptonic decay of a top quark pair comes from the subsequent decay of a W boson which is accompanied by a neutrino. It is thus expected to be rather isolated since it is not the product of the jets. The strategy used in this analysis is to force the jet clustering algorithm to create only four jets in

each event. The searched lepton has distinct features with respect to other particles in the jet: it is either the leading particle in the jet or it has a large transverse momentum with respect to the axis of the closest jet, as depicted Fig. 11.2. In the following such lepton will be called "isolated".

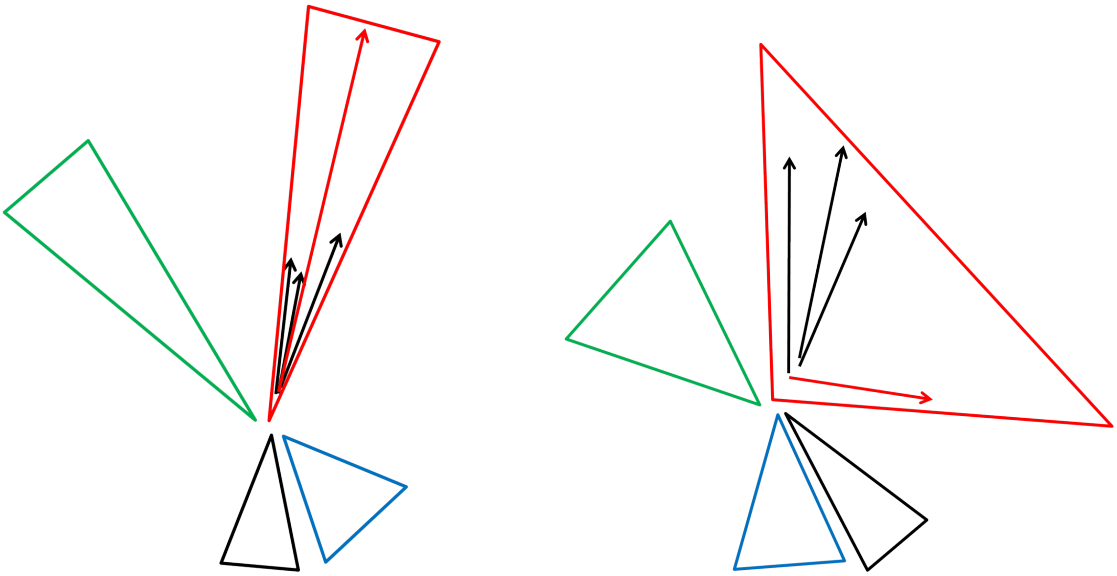

(a) Definition of a leading lepton in a jet.

(b) Definition of a lepton with large transverse momentum with respect to the axis of the jet.

Figure 11.2: Two cases of leptons (red arrow) from semileptonic decay after creating four jets (triangles).

The two variables x_T and z are defined to take these two configurations into account:

$$x_T = \frac{p_T}{M_{\text{jet}}} \tag{11.3}$$

where p_T is the transverse momentum of the identified lepton with respect to its jet and M_{jet} is the mass of the jet ($M_{\text{jet}}^2 = E_{\text{jet}}^2 - \vec{P}_{\text{jet}}^2$), and

$$z = \frac{E_{\text{lepton}}}{E_{\text{jet}}} \tag{11.4}$$

which corresponds to the fraction of energy of the lepton in the jet.

The values for leptons in semileptonic and full hadronic top events can be seen Fig. 11.3. The fraction z is bound to values smaller than 1. And the variable x_T must be less than $1/2$ which is the kinematic limit of a jet taken at rest where the lepton and the other particles are almost back-to-back and share the same energy $M_{\text{jet}}/2$.

The leptons present in the full hadronic top channel are mainly leptons from the decays of bottom mesons which are likely to be embedded in a jet without being isolated.

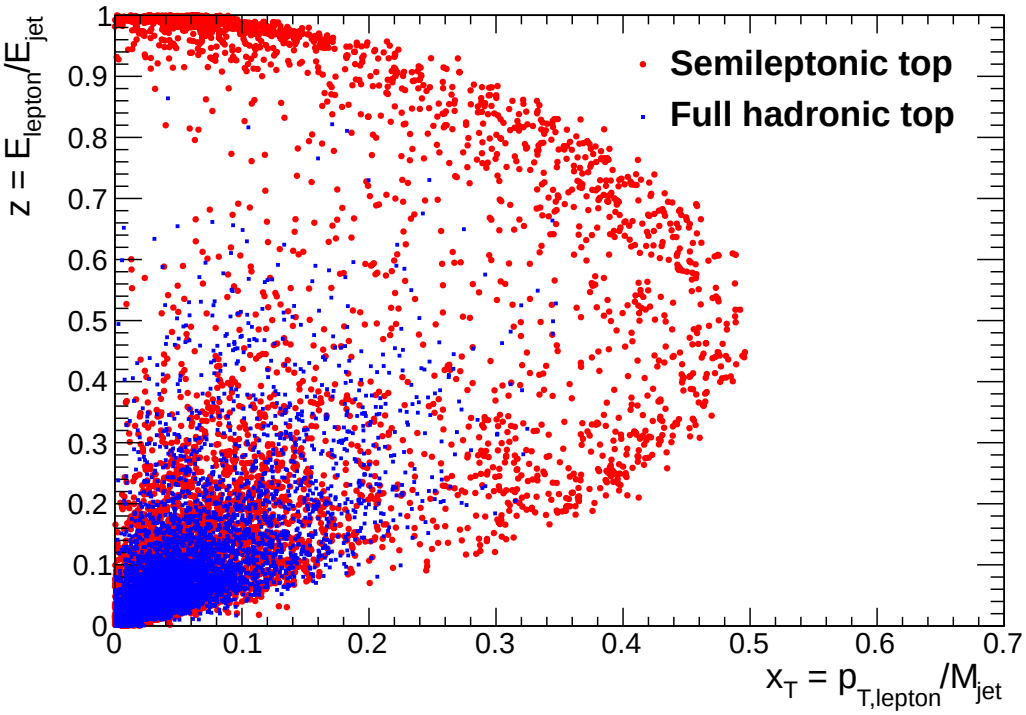

Figure 11.3: Isolation variables applied to a sample of leptons from semileptonic (red) and full hadronic (blue) top events. Isolated leptons and leptons from the decays of bottom mesons are identified and separated.

The following isolation criteria has been chosen to maximize the signal over background ratio:

$$x_T > 0.25 \text{ or } z > 0.6 \tag{11.5}$$

This method prevents to select secondary leptons coming from the decay of a bottom meson and pions contained in a jet which might have been identified as muons. In both cases they are unlikely to be isolated. We retain an event in the analysis if one single isolated lepton is found.

11.1.2 Quality of the isolated lepton

We further analyze the quality of the isolated leptons selected by the cuts in Eq. 11.5 using only signal events.

The fraction of isolated leptons found in a signal sample is given in Fig. 11.4. One may find mainly zero, one or two isolated leptons with the fractions f_0, f_1 and f_2. The fraction f_{3+} to find three or more isolated leptons is around 0.03% and neglected. The probability x to have the good lepton found and y to have a bad lepton found in all

signal events can be deduced from:

$$\begin{aligned} f_0 &= (1-x)(1-y) \\ f_1 &= x(1-y) + y(1-x) \\ f_2 &= xy \end{aligned} \tag{11.6}$$

These probabilities x and y are determined and given Table 11.1, as well as efficiency and contamination. An event is retained in the analysis if one single isolated lepton is found. The efficiency is defined by the number of retained events in the signal sample and is equal to the value f_1. The contamination is the fraction of bad leptons selected in the retained events, that is, $y(1-x)/f_1$.

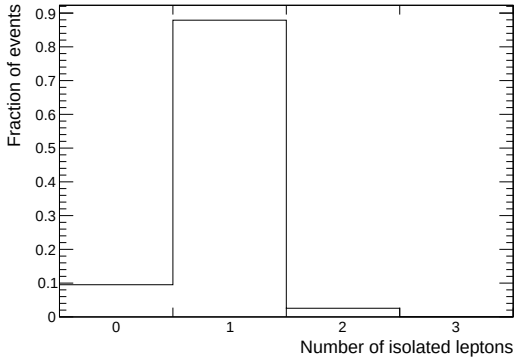

Figure 11.4: Fraction of isolated leptons found in semileptonic top events.

Fraction of	good leptons : x	bad leptons : y	Efficiency	Contamination
	90.2%	2.8%	87.9%	0.3%

Table 11.1: Results of the lepton isolation method on signal events. The probabilities x and y to select a good and a bad lepton respectively are derived from Eq. 11.6. Efficiency and contamination are defined for one single lepton by f_1 and $y(1-x)/f_1$.

From the contamination, one expects the observables connected to the lepton to be measured very accurately, as soon as contamination from other backgrounds is understood.

The energy distributions of the true and the reconstructed leptons are shown Fig. 11.5. A small drop in efficiency is seen at energies below 50 GeV. This is due to isolation cuts which reject leptons toward smaller energies. These leptons are neither leading nor having a large transverse momentum in their jet.

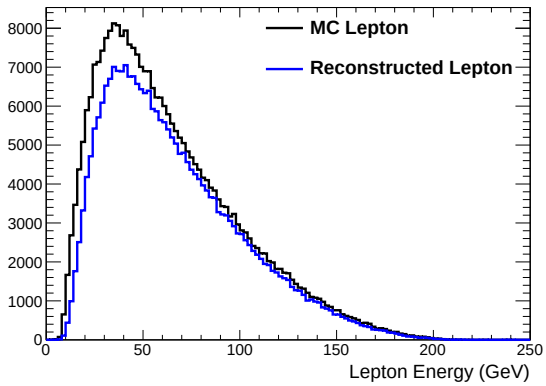

Figure 11.5: Energy distribution of the true lepton from Monte Carlo and the reconstructed one.

11.2 Reconstruction of the W boson and the top quark

After one isolated lepton has been found in an event, the jet clustering forced to four jets is applied again to the remaining particles, followed by B tagging. The two jets with highest B tag value are considered to be the b jets while the two remaining ones are associated to the light quarks from the hadronic W decay. The W mass is defined as the invariant mass of these two jets of light quarks. The mass of this di-jet is shown Fig. 11.6(a) where the W mass peak is clearly seen. The central value and width σ of the distribution are estimated by fitting with a gaussian within $\pm 1\sigma$. The mean is 79.96 ± 0.03 GeV with a width σ of 4.20 ± 0.05 GeV. At the partonic level a central value of 80.424 ± 0.005 GeV is obtained by fitting in the 70-90 GeV mass range with a Breit-Wigner function and the width is 2.02 ± 0.01 GeV, compatible with theoretical values.

The emphasis of this study is not on the precision of the reconstructed mass, rather on the quality and defects of the reconstruction. Problems in reconstruction could mainly be due to a bad particle flow which enlarges the mass spectrum, jet clustering which does not create jets reflecting the original partons, or B tagging which gives a too small B tag value to a true b jet which is used to reconstruct the W boson. Note that the effects of jet clustering can hardly be disentangled from the others: B tagging and the di-jet resolution of the particle flow depend on the content of the jets created. To give an idea of these contributions, an ad-hoc separation is done with the two jets used to reconstruct the W boson and the Monte Carlo information. B tagging is considered to have failed if one of these two jets is actually a b jet. Jet clustering is judged to fail if one of the two angles between the momentum of one jet and its initial hadron differs by more than 50 mrad. This angle is found to be the typical width of distributions of the angular difference of reconstructed jets with initial partons. Other di-jet candidates are assumed to be well tagged and clustered, so that the only errors left may be those of the particle flow. While in some cases these defects may be related, this separation

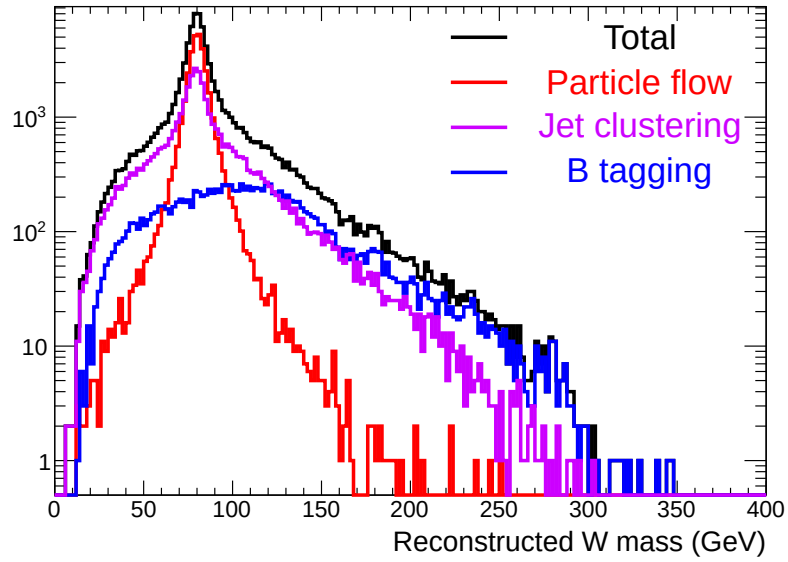

(a) Reconstructed mass of the W boson with semileptonic top events.

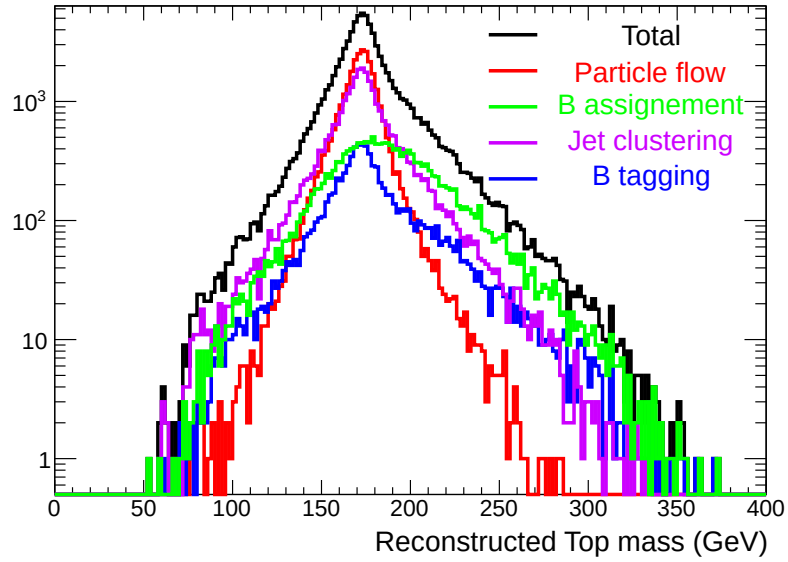

(b) Reconstructed mass of the top quark with semileptonic top events.

Figure 11.6: W and top reconstructed masses for the semileptonic decay channels. All the events are treated with the lepton selection and B tag cuts. The top is reconstructed by using the combination of b jet and W which minimizes d^2 in Eq. 11.7. The total histogram is subdivided into various contributions from the bad B tagging (blue), bad jet clustering (violet), particle flow (red) and b jet mis-assignment (green).

gives an idea of their contribution to the enlargement and tails of the reconstructed W mass. These contributions are shown separately Fig. 11.6(a) in colors.

The tail at small masses is due to the part associated to jet clustering. In case one or the two jets have not be built by picking enough particles, the reconstructed di-jet mass is smaller than the expectation. This also affects the tail at high mass in the opposite way, with jets that have contain particles of others. Nevertheless, the peak at the W mass can be seen in this case since there may be inter-migration of particles between the two light jets which vanish when reconstructing the W boson. Problems in the B tagging affect mainly the tail at high mass. A b jet is likely to appear in a direction different from the expected one, which in most cases increases to opening of the di-jet system and enhances its mass. The assumed contribution from the particle flow explains the width of the reconstructed mass and is in rough agreement with the goal on di-jet mass resolution.

Once the W boson is reconstructed, two b jets are left. Two candidates are defined by the sum of the four-momenta of a b jet and by that the W. Using constraints on their mass and energy, the best candidate for a top quark is chosen to be the one minimizing the quantity d^2, defined by:

$$d^2 = \left(\frac{M_{(\mathrm{b+W})} - M_{\mathrm{top}}}{\sigma_t}\right)^2 + \left(\frac{E_{(\mathrm{b+W})} - E_{\mathrm{top}}}{\sigma_E}\right)^2 \tag{11.7}$$

The values $\sigma_t = 6.3 \pm 0.1\,\mathrm{GeV}$ and $\sigma_E = 8.0 \pm 0.1\,\mathrm{GeV}$ are the widths of the top mass and energy obtained with the difference of the reconstructed top using Monte Carlo information and the partonic one. The two distributions are fitted by a gaussian function within one standard deviation. The value $M_{\mathrm{top}} = 174\,\mathrm{GeV}$ is the input top mass and $E_{\mathrm{top}} = 250\,\mathrm{GeV}$ is the valued expected from the kinematics.

The spectrum of the reconstructed top mass is given in Fig. 11.6(b), where defects of the reconstruction are emphasized. The top quark is reconstructed with a mass $m_t = 172.68 \pm 0.05\,\mathrm{GeV}$ and a width of $7.1 \pm 0.1\,\mathrm{GeV}$. Additional errors coming from a wrong assignment appear in the reconstruction of the top. This has a tendency to produce top quarks with higher mass, which is the same effect than with W bosons where a bad jet is used and the kinematics enhance the mass. Jet clustering still slightly enhances the tails at low and high mass. However, the significant fraction of light and heavy W bosons is here attenuated by selecting another jet and a significant number of reconstructed candidates agree with the top mass. The effect of a bad B tagging is minimum, in particular a small bump is seen at the mass of the top. Some candidates which had been poorly tagged and used to form the W boson are now balanced by the jet added which reconstructs the good top candidate. Finally, the particle flow is seen to be mainly responsible for the width of the peak at the top mass but this peak is shared with the events with original bad jet clustering for the W boson.

The reconstruction of the W boson and the top quark opens the possibility to further reduce the backgrounds left at this stage by cutting on their reconstructed mass. The direction of the top quark will be used for the forward-backward asymmetry.

11.3 Background suppression

The imposed cuts for event selection are to find one single isolated lepton, and that the two highest B tag values out of the four jets (B_{tag1} and B_{tag2}) must satisfy:

$$B_{\text{tag1}} > 0.8 \text{ or } B_{\text{tag2}} > 0.3 \tag{11.8}$$

These values are found after optimizing the signal over background ratio. However, some background is left due to contamination from B tagging and lepton selection, as shown Table 11.2. The next step is to remove the background by using other mostly independent variables. Optimal cut values are chosen to maximize the signal over background ratio.

Cut/Process	bbqqlv	bblvlv	bbqqqq	qqlv	bb
1 lepton	87.9%	37.4%	2.9%	76.4%	14.1%
$B_{\text{tag1}} > 0.8$ or $B_{\text{tag2}} > 0.3$	80.1%	33.9%	2.4%	2.5%	8.8%
Relative fraction	1	0.3	1.35	5.0	1.9

Table 11.2: Signal and main background events left after selecting one isolated lepton and cutting on the B tag values. The relative weights of each process is also shown.

Thrust As pointed out in Sec. 8.2, some backgrounds have different topologies. In particular events with light quark pairs feature in majority two back-to-back jets. One quantity which can be used to distinguish these topologies is the thrust T of the event, defined by:

$$T = \max_{\hat{n}} \frac{|\sum \vec{p_i}.\hat{n}|}{|\sum \vec{p_i}|} \tag{11.9}$$

where the sums run over all reconstructed particles of the event and $\hat{n}$ is a unitary vector, chosen to maximize the value. The thrust is maximally equal to 1, in the case of interest here: back-to-back particles.

Imposing a cut $T < 0.9$ on the thrust removes a substantial fraction of background events, e.g. bb and WW, as reported Table 11.3, while leaving the signal events almost unchanged.

Process	bbqqlv	bbqqqq	bb/qq	qqlv
Fraction left	98.6%	98%	11%	21%

Table 11.3: Efficiency of a cut on thrust smaller than 0.9 for specific events.

Hadronic mass The remaining background is mostly due to the semileptonic decay of W pairs, as well as from the other decays of the top pairs. The "hadronic mass" M_{hadronic} is introduced to suppress significantly the backgrounds left. It is defined by summing over all four-momenta of the particles without that of the lepton and taking the mass of the resulting four-vector.

In case of semileptonic decays of W pairs, the lepton of the leptonic decay was identified and the other particles come from the hadronic decay. The hadronic mass is thus the mass of the W boson which decayed into hadrons. In case of the non-semileptonic decays of the top pairs, the hadronic mass must be small in the case of full leptonic decays since two neutrinos exited the detector and large in the case of full hadronic decays, while the semileptonic decays are found in the intermediate regions. This is supported by Fig. 11.7 and the following cuts are applied:

$$180\,\text{GeV} < M_{\text{hadronic}} < 420\,\text{GeV} \tag{11.10}$$

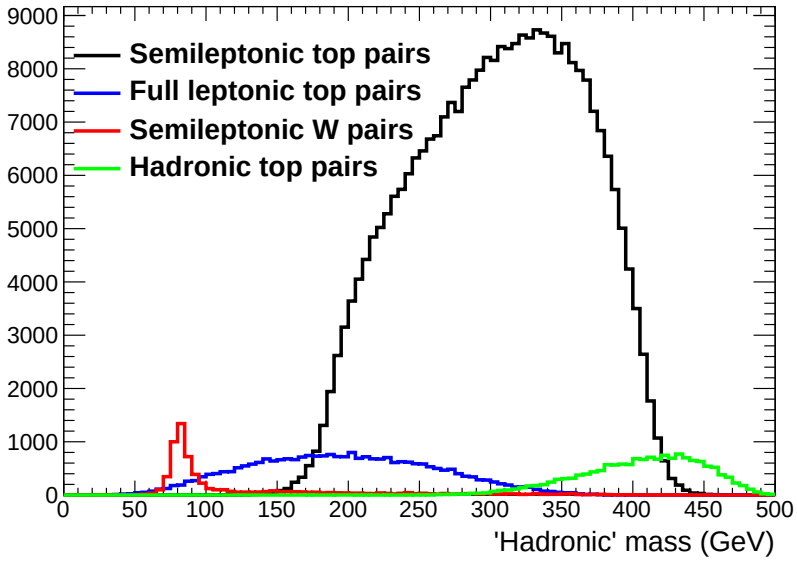

Figure 11.7: Invariant ('hadronic') mass of the event after lepton subtraction.

W and top masses Nevertheless, full hadronic and full leptonic decays are still present. Due to events still left, one has to cut in the $m_W - m_t$ plane to remove the remaining events (see Fig. 11.8). A rectangular cut is applied here:

$$50 < m_{\text{W}} < 250 \text{ and } 120 < m_{\text{t}} < 270 \text{ (all in GeV)} \tag{11.11}$$

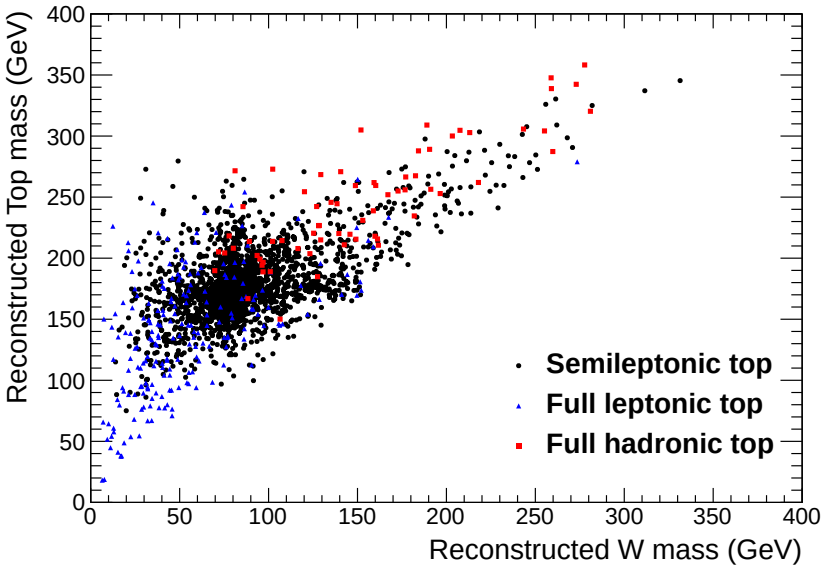

Figure 11.8: W-top reconstructed masses with the main backgrounds left: hadronic (red) and leptonic (blue) top pairs.

11.4 Results of the cuts and uncertainties on the cross-section and left-right asymmetry

The figures of background suppression and final efficiencies are given in Table. 11.4.

These numbers correspond to a 72.7% efficiency and a 95.4% purity using a purely cut-based analysis, where the efficiency is the fraction of signal events left after the cuts and purity is the fraction of these signal events within the final selected event sample. The major contamination in this cut-based analysis comes from the two other decay channels of the top pairs. In particular, the full leptonic decay of the top pairs mimics the semileptonic decay when one of the two charged leptons is a tau which decays

Cut/Process	bbqqlv	bblvlv	bbqqqq	qqlv	bb
1 lepton	87.9%	37.4%	2.9%	76.4%	14.1%
$B_{tag1} > 0.8$ or $B_{tag2} > 0.3$	80.1%	33.9%	2.4%	2.5%	8.8%
Thrust $T < 0.9$	79.4%	31.7%	2.4%	0.4%	0.9%
Hadronic mass	78.4%	18.4%	1.4%	0.07%	0.1%
m_W/m_t	72.7%	9.2%	1.1%	0.04%	0.09%
Relative cross-section	1	0.3	1.35	5.0	1.9

Table 11.4: Fractions of signal and main background events left after series of cuts. Relative cross-sections are shown to estimate purity.

hadronically. Since a jet from a tau lepton has a smaller multiplicity than the others, this background could be further reduced by a cut on the number of tracks in the jet.

A multivariate method using a boosted decision tree [HSS+07] has also been tested on the events after selection of the lepton only. The B tagging variables B_{tag1}, B_{tag2}, thrust T, hadronic mass $\text{M}_{\text{hadronic}}$, W boson and top mass have been used, like in this cut-based analysis. The efficiency to retrieve the signal is of 99% with less than 1% background left, that is, taking into account the efficiency to find the lepton, the total efficiency for the semileptonic decay mode of the top pairs can be as good as 87.0% with 99.5% purity, compatible with the result of the Letter Of Intent (LOI) of the ILD which used a multivariate likelihood method: 87.5% efficiency and 99.8% purity [AAA+10, Top].

To measure the cross-section, one has to count the number of events and know the luminosity $\mathcal{L}$ and efficiency to select the signal ϵ. The cross-section σ is given by the formula:

$$\sigma = \frac{N}{\epsilon \mathcal{L}} \tag{11.12}$$

with N the total number of signal events seen, i.e. measured in the $(|P|, -|P|')$ and $(-|P|, |P|')$ configurations of beam polarization. The corresponding errors on the cross-section is given by:

$$\left(\frac{\Delta\sigma}{\sigma}\right)^2 = \left(\frac{\Delta N}{N}\right)^2 + \left(\frac{\Delta\mathcal{L}}{\mathcal{L}}\right)^2 \tag{11.13}$$

with $\Delta N/N = 1/\sqrt{N}$ and the precision on the luminosity at the ILC, $\Delta\mathcal{L}/\mathcal{L} \approx 0.1\%$.

Using an ideal scenario with 100% polarized beams, one obtains $1/\sqrt{N} = 0.27\%$ ($N \approx 141000$) leading to $\Delta\sigma/\sigma = 0.28\%$, and $\Delta A_{LR}^{0,t}/A_{LR}^{0,t} = 0.68\%$ in this analysis and $(\Delta A_{LR}^{0,t}/A_{LR}^{0,t})_{LOI} = 0.41\%$ in the LOI which benefits from the full hadronic decay mode too.

Starting from the results with 100% polarised beams, the uncertainties can be derived for realistic sets of polarisations at the ILC. The two sets of values used (P, P') are the baseline of the ILC, namely $(\pm 80\%, 0)$ and the best scenario $(\pm 90\%, \mp 60\%)$. The number of events N entering the statistics are reduced by a factor $(1 + |P||P'|)/2$ with respect to the 100% polarised case, see e.g. Eq. 8.1.

As explained Chap. 8, the important uncertainty for precise measurement of $A_{LR}^{0,t}$ is given by the equivalent polarization $P_{\text{eff}} = (|P| + |P'|)/(1 + |P||P'|)$ and should remain below the per-mil level to be neglected, which is assumed here. Note that in the best scenario of polarization, $P_{\text{eff}} \approx 0.97$ is close to the case of 100% polarizations what gives $A_{LR} \approx A_{LR}^0$ with the difference that the statistics of available events will be reduced.

The following Table 11.5 summarizes the uncertainties on A_{LR}^t using those two sets of polarizations and show the gain of a factor two in the precision between them.

This analysis was pursued in a cut-based form, so that the efficiencies and purities at each step are understood. In particular, this helps in determining the systematics associated to the contamination of the background.

The left-right asymmetry with the remaining backgrounds $A_{LR}^{\text{sig+bgd}}$ is found to be 37.2%, close to the value $A_{LR}^{0,t} = 36.7\%$ since the top channels are the main backgrounds left and slightly larger since that of the WW process is close to 100%. The ZWW process

Polarization (P,P')	A^t_{LR}	$\Delta\sigma/\sigma$	$\Delta A^t_{LR}/A^t_{LR}$	$(\Delta\sigma/\sigma)_{LOI}$	$(\Delta A^t_{LR}/A^t_{LR})_{LOI}$
$(\pm 100\%, \mp 100\%)$	36.7%	0.28%	0.68%	0.19%	0.41%
$(\pm 90\%, \mp 60\%)$	35.6%	0.32%	0.78%	0.21%	0.47%
$(\pm 80\%, 0)$	29.4%	0.39%	1.24%	0.25%	0.75%

Table 11.5: Precisions reached on σ and A^t_{LR} with different sets of polarization and comparison with the ILD Letter Of Intent where the full hadronic decay mode is also accounted for.

which asymmetry is almost 90% accounts for 1% contamination and also contributes to this increase. The measured left-right asymmetry deviates from that of the top pair by a 1.36% relative change from its original value, comparable to its expected statistical uncertainty of 1.24%. In the favorable case of 99.5% purity, the shift in the measured left-right asymmetry is ten times smaller, i.e. negligible compared to the statistical uncertainty.

11.5 Forward-backward asymmetry and lepton-related observables

Reconstructing the top forward-backward asymmetry A^t_{FB} requires to have a top quark reconstructed and the knowledge of its charge. As explained before, the sign of the top quark is the opposite to that of the reconstructed lepton. The differential cross-section of reconstructed top quarks as a function of their polar angle θ is shown in Fig. 11.9, where reconstructed anti-top quarks of polar angle θ have been changed to a top quark of polar angle $\theta + \pi$.

The agreement between reconstructed top candidates and the Monte Carlo ones is found to be good in the configuration $e^-_R e^+_L$ compared to the opposite configuration which leads to much worse results. There is a systematic deviation of the reconstructed forward-backward asymmetry of -2.3% in the first configuration and of -13.8% in the second one. Several checks have been done in order to understand the differences. It seems to come from the population of top candidates in which the wrong combination of a b jet and the W boson was chosen. But even changing the combination method cannot improve the results substantially. Moreover several other sources of bad reconstruction may also explain these results such as a bad B tagging, bad jet clustering due to migration of particles between two jets or gluon radiation. The practical solution with real data would be to correct the value of A^t_{FB} from these differences for each polarization.

Because of this problem of reconstruction, the total forward-backward asymmetry with the background is found to differ from that of the Monte Carlo in relative values by -28.0%, mainly because of the pull in the e^-_L configuration which has a larger weight due to the larger cross-section with respect to the e^-_R configuration. The relative difference coming from the background only accounts for -2.2% here and could even be neglected

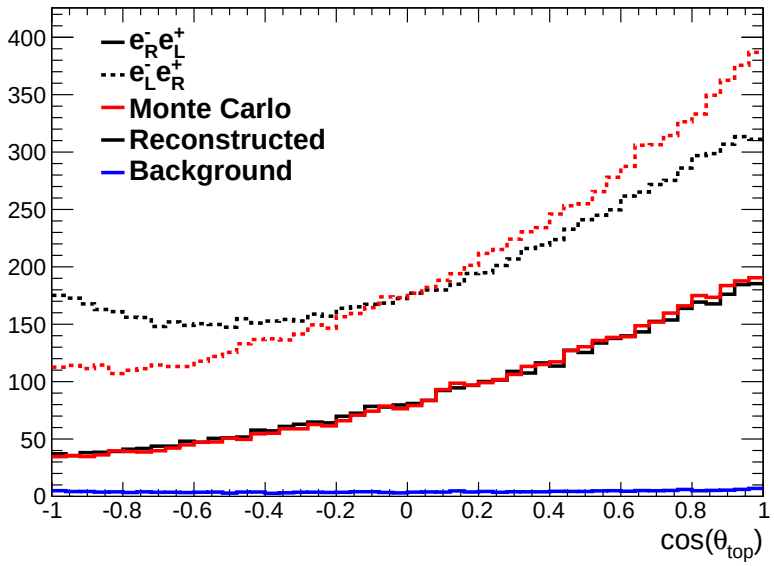

Figure 11.9: Angular distribution of the reconstructed top candidates in both configurations of polarization compared to the Monte Carlo ones. The configuration with e^-_R remains in substantial disagreement despite efforts to understand the differences. The background in the case e^-_R is also shown.

with a purity larger than 99.5%.

The distributions of the lepton are in much better agreement than the top quark, as shown in Fig. 11.10. Only very forward and backward regions suffer from the smaller tracking efficiencies spotted in Chap. 10.

In the following discussions, the systematics will be neglected and only statistical errors will be taken into account.

The measurement of A^t_{FB} uses only the semileptonic top pair events (34% of all top pair events). In the case of 100% polarized beams, the statistical uncertainty is found to be $\Delta A^t_{FB}/A^t_{FB} = 0.76\%$. Results for other polarisations are summarized Table 11.6. The precisions on the left and right couplings of the top quark to the Z boson $Q^{t_L}_Z$ and $Q^{t_R}_Z$ are derived from Eq. 8.12 and given Table 11.6 and are better than the 2% precision reached in the LOI.

Polarization (P,P')	$\Delta A^{0,t}_{LR}/A^{0,t}_{LR}$	$\Delta A^t_{FB}/A^t_{FB}$	$\Delta Q^{t_L}_Z/Q^{t_L}_Z$	$\Delta Q^{t_R}_Z/Q^{t_R}_Z$
$(\pm 100\%, \mp 100\%)$	0.68%	0.76%	0.87%	1.59%
$(\pm 90\%, \mp 60\%)$	0.78%	0.85%	0.95%	1.78%
$(\pm 80\%, 0)$	1.24%	1.07%	1.24%	2.28%

Table 11.6: Precisions reached with this analysis on $A^{0,t}_{LR}$, A^t_{FB} and the derived precisions on top to Z couplings.

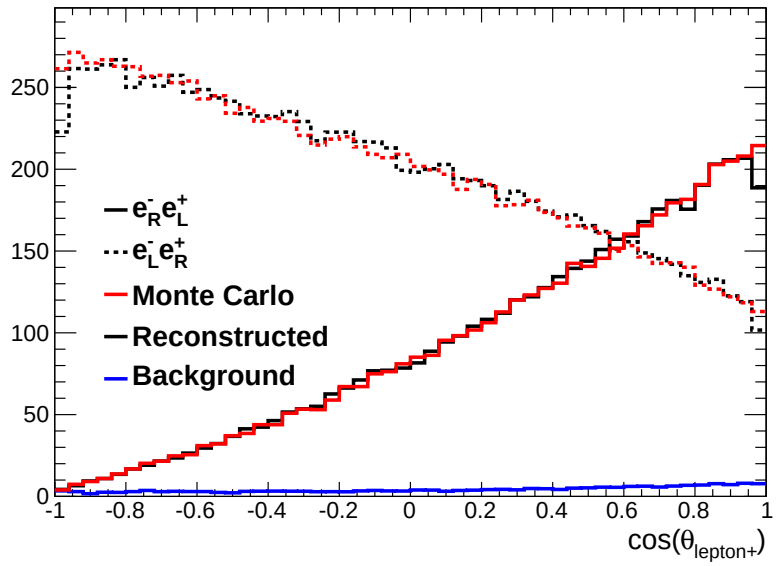

Figure 11.10: Angular distribution of the reconstructed lepton candidates in both configurations of polarization compared to the Monte Carlo ones. The background in the case e^-_R is also shown.

The couplings can be determined at the percent level. However other observables can be used in the case of semileptonic, like those suggested in Chap. 8: the forward-backward asymmetry of the lepton A^l_{FB} or the asymmetry D^l defined in Eq. 8.13. This study focuses on the top quark couplings to the Z boson, but these additional variables could be used to derive other coupling factors e.g. anomalous magnetic or dipole couplings.

The point of view adopted here is to combine these four observables to reach higher sensitivity in the couplings studied. This can be done for any set of uncorrelated observables, so that additional ones may be added there. To show the possibilities of such combination, the uncertainty adopted on $A^{0,t}_{LR}$ is the same than before. However better resolutions could be achieved by adding the full hadronic decay channel of the top quark of the LOI.

Eq. 8.12 and 8.14 show that the four observables studied here can all be written in the form $X = a_{\text{obs}} Q_Z^{t_L} + b_{\text{obs}} Q_Z^{t_R}$, where X is the observable considered. The quantity χ^2 is defined by:

$$\chi^2 = \sum_{\text{observables}} P_{\text{obs}} (a_{\text{obs}} Q_Z^{t_L} + b_{\text{obs}} Q_Z^{t_R} - X^{\text{exp}}) \tag{11.14}$$

where $P_{\text{obs}} = 1/\sigma^2(X)$ is the weight factor (inverse of the variance of the observable X) and X^{exp} is the experimental value of X. Minimizing this quantity with respect to $Q_Z^{t_L}$ and $Q_Z^{t_R}$ leads to their experimental value, as well as their variance given in Table 11.7.

The effect of the combination is not large but interesting: the precision achieved in the baseline configuration with combination is around that without combination, using the

Polarization (P,P')	$\Delta A^l_{FB}/A^l_{FB}$	$\Delta D^l/D^l$	$\Delta Q^{t_L}_Z/Q^{t_L}_Z$	$\Delta Q^{t_R}_Z/Q^{t_R}_Z$
$(\pm 100\%, \mp 100\%)$	2.74%	1.57%	0.77%	1.23%
$(\pm 90\%, \mp 60\%)$	3.05%	1.84%	0.86%	1.38%
$(\pm 80\%, 0)$	3.86%	3.00%	1.14%	1.76%

Table 11.7: Precisions reached on A^l_{FB}, D^l. The derived precisions on top to Z couplings use the combination method with the four observables $A^{0,t}_{LR}$, A^t_{FB}, A^l_{FB} and D^l.

best scenario. If the precision on $A^{0,t}_{LR}$ is taken to be that of the LOI, uncertainties below the percent level are foreseen, e.g. after combination with the baseline configuration $\Delta Q^{t_L}_Z/Q^{t_L}_Z = 1.03\%$ and $\Delta Q^{t_R}_Z/Q^{t_R}_Z = 1.75\%$.

11.6 Conclusion on the precision reached

11.6.1 Systematic uncertainties

A main systematic in this study comes from polarization. Given the uncertainties on the left-right and forward-backward asymmetries, the polarization needs to be known better than 0.1% in order not to affect the sensitivity given by the statistics.

Moreover, a high purity should guarantee small systematics from the background. As discussed in Sec. 11.4 for the left-right and forward-backward asymmetries, systematics can be as small as a few percent.

At this stage of the simulation, systematics from the subdetectors are not known. Systematic effects of an asymmetric configuration of the detector, e.g. cables, should have a minor effect. Indeed, assuming charge conservation, the same number of quarks reconstructed forward (backward) than anti-quarks reconstructed backward (forward) is expected in the detector. This amounts to the same counting in the measurement of the forward-backward asymmetry of top quarks.

However a problem of reconstruction was spotted in the reconstruction of the top quark. If it is not solved, systematics of the order of the statistical uncertainties and even larger can lead to sizable effects and decrease the precisions achieved. The use of leptonic observables introduces less systematics since the reconstruction of leptons is of high purity.

11.6.2 Extra-dimensional models

Regarding extra-dimensional models, the previously mentioned precisions on the left and right couplings of the top quark to the Z boson can lead to an excellent separation between each model, since the combined method leads to precisions around the one percent level. Each of the models highlighted in Fig. 7.3 can thus be disentangled.

It is possible to derive a limit on the Kaluza-Klein mass scale m_{KK} probed here by using the relative uncertainty on the right coupling of the top quark to the Z boson

$\Delta Q_Z^{t_R}/Q_Z^{t_R}$, and Eq. 7.3.

First, assuming no extension to $SU(2)_R$ of the symmetry in the bulk, i.e. no additional Z' boson thus $g_{Z'} = 0$ in Eq. 7.3, the mass probed can be as high as $m_{KK} \approx 2.8\,\text{TeV}$ at the level of three standard deviations. This assumption is valid, for instance in the case of [CVGQ11], using a typical value of $c_{t_R} = -0.5$ to generate the mass of the top quark [DMR07].

Second, extending to $SU(2)_R$, Eq. 7.3 becomes:

$$\frac{\Delta Q_Z^{t_R}}{Q_Z^{t_R}} \approx \left(\frac{M_Z}{0.4 M_{KK}}\right)^2 \left[\frac{0.75}{\sin^2\theta'}\right] F(c_{t_R}) \tag{11.15}$$

assuming that the Z-Z' mixing is the dominant contribution to the modification of this coupling. This is preferred in several models, like in [DMR07] where $\sin\theta'$ of about 0.1 is preferred to retrieve the measured value of $A_{FB}^{0,b}$ at LEP. This implies the possibility to probe $M_{KK} = 25\,\text{TeV}$ at the level of three standard deviations, in the case $\sin\theta' = 0.1$.

11.6.3 A comparison with LHC and CLIC

The top quark cross section at LHC is $\approx 160\,\text{pb}$ at $\sqrt{s}$ =7 TeV (see e.g. [Col, AAA$^+$11, AAA$^+$99]) where the dominant mechanism is gluon fusion $gg \to t\bar{t}$. The top production is there much more enhanced which allows for measurement of its rare decay modes. However the reconstruction efficiency is only around 10% and the signal over background ratio is worse due to the QCD background and the parton density functions that need to be known. Photon and Z couplings to the top quark are measured by isolating ttZ and ttγ final states. The precisions reached on photon couplings are similar to the ILC but worse for the Z couplings [A$^+$01, JKP$^+$06], where the vector and axial couplings $\tilde{F}_{1V}^Z$ and $\tilde{F}_{1A}^Z$ are considered to be measured with a precision of about 10%. These precisions at the LHC can be translated into precisions on the left and right couplings: $\Delta Q_Z^{t_L}/Q_Z^{t_L} = 17\%$ and $\Delta Q_Z^{t_R}/Q_Z^{t_R} = 40\%$ for $300\,\text{fb}^{-1}$ luminosity.

The coupling of the top quark to bottom quark and W boson can be probed at the LHC (at the ILC too but this was not the main focus here), via single top production i.e. $q\bar{q}' \to W \to tb$ which cross-section is of 4.3 pb. However, the efficiency of reconstruction is also worse with a small signal over noise ratio. The fact that it proceed via a charged current renders difficult to probe the Randall-Sundrum scenarios. Indeed, their important modifications arise via couplings of the Z boson to the additional Z' and their Kaluza-Klein modes.

The first study of top pair production at CLIC was performed at $\sqrt{s}$ =3 TeV [Sal03], and leads mainly to a topology of two jets given the velocity of the top $\beta_t \approx 8.6$. The measurements there require to develop new functionalities to directly tag a jet as a top jet, what is made difficult by the background of b jets and other heavy jets such as those of Z and W bosons. Moreover the cross-section is 36 times smaller and the accuracy of the measurements would be $\Delta\sigma/\sigma = 1.4\%$ and $\Delta A_{FB}^t/A_{FB}^t = 4.2\%$ with a luminosity of $1\,\text{ab}^{-1}$. The results suggest worse accuracies due to inefficiencies in the B tagging.

Chapter 12

Conclusion

The International Linear Collider (ILC) is likely to be the next electron position collider. It is aimed at precision measurements in the sector of the electroweak symmetry breaking. These precisions strongly suggest to base the design of a detector on the particle flow technique. The particle flow requires highly segmented calorimeters to separate various showers created by jets in a detector, such as the proposed International Large Detector (ILD).

A fine grained prototype for a silicon-tungsten electromagnetic calorimeter (SiW ECAL) was tested with hadrons of energies between 2 and 10 GeV, which are present in jets at the ILC. A detailed study of hadronic interactions was performed and brought unprecedented insight in the details of shower patterns of these interactions. It is possible to find low energy interactions within 2 layers of the ECAL ($\sim 2\,\mathrm{cm}$) with an efficiency between 62% and 83%. An algorithm appropriate to treat those showers was developped and used to compare the response of this device with various simulations available on the market. The events have been classified into four classes depending on the strength of the interaction. Events with small populated final states are identified and could serve as a basis to understand further the various patterns of hadronic interactions. A good agreement was found which validates the physics studies performed with ILD which are of essential importance for the main features of the top analysis performed in this work. This applies in particular for the particle flow method used to reconstruct neutral clusters and to the search of charged leptons in complex top final states. Future improvements of particle flow algorithms should include such knowledge to reduce confusion in jets.

A realistic simulation study of semileptonic top decays has been performed at a center-of-mass energy $\sqrt{s} = 500\,\mathrm{GeV}$ with an integrated luminosity $\mathcal{L} = 500\,\mathrm{fb}^{-1}$. This allows to confirm the excellent performances expected from a detector optimized for particle flow. Two essential features were the most important: first, the full angular coverage of the detector, thanks to the forward tracking systems. Second, the b-tagging efficiency and purity was crucial to identify top events but suffered essentially from early jet clustering before vertex finding. Some progress has already started regarding B tagging and jet clustering. New algorithms of B tagging which do not rely on jet clustering are being proposed and some improvement on jet clustering is expected in the

future.

The reconstruction efficiency reaches 72.7% and 95.4% purity using a cut-based analysis. Higher efficiencies and purities may be obtained by employing multivariate techniques like boosted decision trees. The observables of interest were the left-right polarization asymmetry $A_{LR}^{0,t}$ and the forward-backward asymmetry A_{FB}^{t}. With this analysis, the relative uncertainties using the baseline for polarisation at the ILC $(\pm 80\%, 0)$ are found to be $\Delta A_{LR}^{t}/A_{LR}^{t} = 1.24\%$ and $\Delta A_{FB}^{t}/A_{FB}^{t} = 1.07\%$. Sensitivities of the left and right couplings of the top quark to the Z boson have been derived from these two figures and found to be $\Delta Q_Z^{t_L}/Q_Z^{t_L} = 1.24\%$ and $\Delta Q_Z^{t_R}/Q_Z^{t_R} = 2.28\%$. It can be further reduced by using more observables, like the forward-backward asymmetry of the lepton A_{FB}^{l} and a proposed asymmetry D^l measured with 3.86% and 3.00% accuracies. The expected precisions could be $Q_Z^{t_L}/Q_Z^{t_L} = 1.14\%$ and $\Delta Q_Z^{t_R}/Q_Z^{t_R} = 1.76\%$. As an example, several Randall-Sundrum scenarios featuring modifications in the couplings of the Z boson to the top quark can be distinguished. These modifications are typically of order of 10% and could be distinguished with evidence of new physics seen with such precisions. It is possible to probe some scenarios up to typical Kaluza-Klein masses of 2.8 TeV and even up to 25 TeV in some cases.

In view of the challenges posed by the physics at the ILC, the detectors have proved to be able to meet the high precision requirements and new technological prototypes are ready to prove they are mature enough to build a detector for the ILC.

Bibliography

[A+01] T. Abe et al. Linear collider physics resource book for snowmass 2001-part 3: Studies of exotic and standard model physics. *Arxiv preprint hep-ex/0106057*, 2001.

[AAA+99] B. Abbott, M. Abolins, V. Abramov, BS Acharya, I. Adam, DL Adams, M. Adams, S. Ahn, H. Aihara, GA Alves, et al. Measurement of the top quark pair production cross section in pp collisions using multijet final states. *Physical Review D*, 60(1):012001, 1999.

[AAA+03] S. Agostinelli, J. Allison, K. Amako, J. Apostolakis, H. Araujo, P. Arce, M. Asai, D. Axen, S. Banerjee, G. Barrand, et al. Geant4-a simulation toolkit. *Nuclear Instruments and Methods in Physics Research-Section A Only*, 506(3):250–303, 2003.

[AAA+06] J. Allison, K. Amako, J. Apostolakis, H. Araujo, P.A. Dubois, M. Asai, G. Barrand, R. Capra, S. Chauvie, R. Chytracek, et al. Geant4 developments and applications. *Nuclear Science, IEEE Transactions on*, 53(1):270–278, 2006.

[AAA+10] T. Abe, J.M. Abernathy, H. Abramowicz, M. Adamus, B. Adeva, K. Afanaciev, J.A. Aguilar-Saavedra, C. Alabau Pons, H. Albrecht, L. Andricek, et al. The international large detector: Letter of intent. Technical report, 2010.

[AAA+11] G. Aad, B. Abbott, J. Abdallah, AA Abdelalim, A. Abdesselam, O. Abdinov, B. Abi, M. Abolins, H. Abramowicz, H. Abreu, et al. Measurement of the top quark-pair production cross section with atlas in pp collisions at tev. *The European Physical Journal C-Particles and Fields*, 71(3):1–36, 2011.

[Acc] International Committee For Future Accelerators. `http://www.fnal.gov/directorate/icfa/icfa_LCstatement0204.html`.

[ADMS03] K. Agashe, A. Delgado, MJ May, and R. Sundrum. Rs1, custodial isospin and precision tests. *Journal of High Energy Physics*, 2003(08):050, 2003.

[AKR+09] C. Adloff, Y. Karyotakis, J. Repond, J. Yu, G. Eigen, CM Hawkes, Y. Mikami, O. Miller, NK Watson, JA Wilson, et al. Response of the calice si-w electromagnetic calorimeter physics prototype to electrons. *Nu-*

clear Instruments and Methods in Physics Research Section A: Accelerators, Spectrometers, Detectors and Associated Equipment, 608(3):372–383, 2009.

[AKR+10a] C. Adloff, Y. Karyotakis, J. Repond, A. Brandt, H. Brown, K. De, C. Medina, J. Smith, J. Li, M. Sosebee, et al. Construction and commissioning of the calice analog hadron calorimeter prototype. *Journal of Instrumentation*, 5:P05004, 2010.

[AKR+10b] C. Adloff, Y. Karyotakis, J. Repond, J. Yu, G. Eigen, Y. Mikami, NK Watson, JA Wilson, T. Goto, G. Mavromanolakis, et al. Study of the interactions of pions in the calice silicon-tungsten calorimeter prototype. *Journal of Instrumentation*, 5:P05007, 2010.

[B+86] Y. Bigi et al. Production and decay properties of ultra-heavy quarks* 1. *Physics Letters B*, 181(1-2):157–163, 1986.

[Bal] V.E. Balakin. Travelling focus regime for linear collider.

[Bat10] M. Battaglia. Vertex tracking at a future linear collider. *Nuclear Instruments and Methods in Physics Research Section A: Accelerators, Spectrometers, Detectors and Associated Equipment*, 2010.

[BDG+09] D. Bailey, E. Devetak, M. Grimes, K. Harder, S. Hillert, D. Jackson, T. Pinto Jayawardena, B. Jeffery, T. Lastovicka, C. Lynch, et al. The lcfivertex package: Vertexing, flavour tagging and vertex charge reconstruction with an ilc vertex detector. *Nuclear Instruments and Methods in Physics Research Section A: Accelerators, Spectrometers, Detectors and Associated Equipment*, 610(2):573–589, 2009.

[BDJM07] T. Behnke, C. Damerell, J. Jaros, and A. Myamoto. Ilc reference design report volume 4-detectors. *Arxiv preprint arXiv:0712.2356*, 2007.

[BEM09] P. Bechtle, W. Ehrenfeld, and I. Marchesini. Measurement of the beam polarization at the ilc using the ww production. Technical report, LC-DET-2009-003, 2009.

[Blo88] A. Blondel. A scheme to measure the polarization asymmetry at the z pole in lep. *Physics Letters B*, 202(1):145–148, 1988.

[Bou10] Charles Bouchart. *Phenomenology of the Electroweak Sector in Warped (Supersymmetric) Extra Dimensional Models*. PhD thesis, Université Paris Sud - Paris XI, 2010.

[BOW07] J. Brau, Y. Okada, and N. Walker. Ilc reference design report volume 1-executive summary. *Arxiv preprint arXiv:0712.1950*, 2007.

[C+09] R. Cornat et al. Semiconductor sensors for the calice siw emc and study of the cross-talk between guard rings and pixels in the calice siw prototype. In *Journal of Physics: Conference Series*, volume 160, page 012067. IOP Publishing, 2009.

[Cal] Calice software webpage. `https://svnsrv.desy.de/viewvc/calice`.

[CDO+91] S. Catani, Y.L. Dokshitzer, M. Olsson, G. Turnock, and BR Webber. New clustering algorithm for multijet cross sections in e+ e-annihilation* 1. *Physics Letters B*, 269(3-4):432–438, 1991.

[CFA87] A. Chodos, P.G.O. Freund, and T.W. Appelquist. Modern kaluza-klein theories, 1987.

[CGPT04] C. Csaki, C. Grojean, L. Pilo, and J. Terning. Towards a realistic model of higgsless electroweak symmetry breaking. *Physical review letters*, 92(10):101802, 2004.

[CGS10] Y. Cui, T. Gherghetta, and J. Stokes. Fermion masses in emergent electroweak symmetry breaking. *Journal of High Energy Physics*, 2010(12):1–21, 2010.

[Col] ATLAS Collaboration. Atlas conference notes. `https://atlas.web.cern.ch/Atlas/GROUPS/PHYSICS/CONFNOTES/`.

[CPSW06] M. Carena, E. Ponton, J. Santiago, and C.E.M. Wagner. Light kaluza-klein states in randall-sundrum models with custodial su (2). *Nuclear Physics B*, 759(1-2):202–227, 2006.

[CVGQ11] J.A. Cabrer, G. Von Gersdorff, and M. Quiros. Warped electroweak breaking without custodial symmetry. *Physics Letters B*, 2011.

[Djo08] A. Djouadi. The anatomy of electroweak symmetry breaking:: Tome i: The higgs boson in the standard model. *Physics reports*, 457(1-4):1–216, 2008.

[DLM+07] A. Djouadi, J. Lykken, K. Mönig, Y. Okada, M. Oreglia, and S. Yamashita. Ilc reference design report volume 2-physics at the ilc. *Arxiv preprint arXiv:0709.1893*, 2007.

[DMR07] A. Djouadi, G. Moreau, and F. Richard. Resolving the puzzle in an extra dimensional model with an extended gauge structure. *Nuclear Physics B*, 773(1-2):43–64, 2007.

[DNP10] E. Devetak, A. Nomerotski, and M.E. Peskin. Top quark anomalous couplings at the international linear collider. *Arxiv preprint arXiv:1005.1756*, 2010.

[E+11] E. Elsen et al. International linear collider: A technical progress report. 2011. `http://ilcdoc.linearcollider.org/record/32863/files/ilc_interim_report_2011-lores.pdf`.

[FPR] K. Fujii, M. Peskin, and F. Richard. Reference reactions for the world-wide lc study. `http://www.slac.stanford.edu/~mpeskin/LC/refrxns.html`.

[FTB] Fermilab test beam facility. `http://www-ppd.fnal.gov/MTBF-w`.

[G4l] Reference physics lists in geant4. `http://geant4.web.cern.ch/geant4/support/proc_mod_catalog/physics_lists/referencePL.shtml`.

[Gea] Geant4 webpage. `http://geant4.web.cern.ch/geant4`.

[Gla61] S.L. Glashow. Partial-symmetries of weak interactions. *Nuclear Physics*, 22(4):579–588, 1961.

[GRS06] R.M. Godbole, S.D. Rindani, and R.K. Singh. Lepton distribution as a probe of new physics in production and decay of the t quark and its polarization. *Journal of High Energy Physics*, 2006:021, 2006.

[Han06] T. Han. Collider phenomenology: Basic knowledge and techniques. *Physics in D>: proceedings of the Theoretical Advanced Study Institute in Elementary Particle Physics: TASI 2004: Boulder, CO, USA, 6 June-2 July 2004*, page 407, 2006.

[Haw] R. Hawkings. Vertex detector and flavour tagging studies for the tesla linear collider. *LC-PHSM-2000-021.*

[HM05] Y. Hosotani and M. Mabe. Higgs boson mass and electroweak-gravity hierarchy from dynamical gauge-higgs unification in the warped spacetime. *Physics Letters B*, 615(3-4):257–265, 2005.

[HSS+07] A. Höcker, P. Speckmayer, J. Stelzer, J. Therhaag, E. von Toerne, H. Voss, M. Backes, T. Carli, O. Cohen, A. Christov, et al. Tmva-toolkit for multivariate data analysis. *Arxiv preprint physics/0703039*, 2007.

[ITR04] Internation technology recommendation panel report, 2004. `http://www.fnal.gov/directorate/icfa/ITRP_Report_Final.pdf`.

[JKP+06] A. Juste, Y. Kiyo, F. Petriello, T. Teubner, K. Agashe, P. Batra, U. Baur, CF Berger, JAR Cembranos, A. Ridder, et al. Report of the 2005 snowmass top/qcd working group. *Arxiv preprint hep-ph/0601112*, 2006.

[KOR07] W. Kilian, T. Ohl, and J. Reuter. Whizard: simulating multi-particle processes at lhc and ilc. *Arxiv preprint arXiv:0708.4233*, 2007.

[Krä06] T. Krämer. Track parameters in lcio. 2006.

[Lyk06] J. Lykken. Discovering the quantum universe. *Bulletin of the American Physical Society*, 2006.

[Mal99] J. Maldacena. The large-n limit of superconformal field theories and supergravity. *International journal of theoretical physics*, 38(4):1113–1133, 1999.

[Mok] Mokka webpage. `http://polzope.in2p3.fr:8081/MOKKA`.

[MPAA+08] G. Moortgat-Pick, T. Abe, G. Alexander, B. Ananthanarayan, AA Babich, V. Bharadwaj, D. Barber, A. Bartl, A. Brachmann, S. Chen, et al. Polarized positrons and electrons at the linear collider. *Physics Reports*, 460(4-5):131–243, 2008.

[MWS+05] K. Moffeit, M. Woods, P. Schüler, K. Moenig, and P. Bambade. Spin rotation schemes at the ilc for two interaction regions and positron polarization with both helicities. 2005.

[Nak10] K. Nakamura. Review of particle physics. *Journal of Physics G: Nuclear and Particle Physics*, 37:075021, 2010.

[Ohl00] T. Ohl. O'mega & whizard: Monte carlo event generator generation for future colliders. *Arxiv preprint hep-ph/0011287*, 2000.

[Pan] High Energy Physics Advisory Panel. Discovering the quantum universe. `http://www.interactions.org/pdf/Quantum_Universe.pdf`.

[PR96a] P. Poulose and S.D. Rindani. Decay-lepton angular distribution in polarized $e^+e^- \to t\bar{t}$ and cp-violating dipole couplings of the top quark. *Physical Review D*, 54(7):4326, 1996.

[PR96b] P. Poulose and S.D. Rindani. Simple decay-lepton asymmetries in polarized and cp-violating dipole couplings of the top quark. *Physics Letters B*, 383(2):212–218, 1996.

[PR00] P. Poulose and S.D. Rindani. Erratum: Decay-lepton angular distribution in polarized $e^+e^- \to t\bar{t}$ and cp-violating dipole couplings of the top quark [phys. rev. d 54, 4326 (1996)]. *Physical Review D*, 61(11):119901, 2000.

[PS96] S. Parke and Y. Shadmi. Spin correlations in top-quark pair production at e+ e-colliders. *Physics Letters B*, 387(1):199–206, 1996.

[PTW07] N. Phinney, N. Toge, and N. Walker. Ilc reference design report volume 3-accelerator. *Arxiv preprint arXiv:0712.2361*, 2007.

[Pyt] Standard model data samples. `https://confluence.slac.stanford.edu/display/ilc/Standard+Model+Data+Samples`.

[RCF] A. Raspereza, X. Chen, and A. Frey. Ldc tracking package.

[Ric] F. Richard. Cross-sections at ilc. *To appear in LAL reports.*

[Ric07] F. Richard. Scenarios for ilc in 2010. *LAL report*, 07-80, 2007.

[Rin00] S.D. Rindani. Effect of anomalous tbw vertex on decay-lepton distributions in $e^+e^- \to t\bar{t}$ and cp-violating asymmetries. *Pramana*, 54(6):791–812, 2000.

[RS99a] L. Randall and R. Sundrum. An alternative to compactification. *Physical Review Letters*, 83(23):4690–4693, 1999.

[RS99b] L. Randall and R. Sundrum. Large mass hierarchy from a small extra dimension. *Physical Review Letters*, 83(17):3370–3373, 1999.

[RYH+08] J. Repond, J. Yu, CM Hawkes, Y. Mikami, O. Miller, NK Watson, JA Wilson, G. Mavromanolakis, MA Thomson, DR Ward, et al. Design and electronics commissioning of the physics prototype of a si-w electromagnetic calorimeter for the international linear collider. *Journal of Instrumentation*, 3:P08001, 2008.

[Sal68] A. Salam. Elementary particle theory: Relativistic groups and analyticity (nobel symposium no. 8), 1968.

[Sal03] L. Salmi. tt cross-section and forward-backward asymmetry at clic. *Arxiv preprint hep-ex/0301021*, 2003.

[SLM01] T. Sjöstrand, L. Lönnblad, and S. Mrenna. Pythia 6.2 physics and manual. *Arxiv preprint hep-ph/0108264*, 2001.

[SP92] C.R. Schmidt and M.E. Peskin. Probe of cp violation in top quark pair production at hadron supercolliders. *Physical Review Letters*, 69(3):410–413, 1992.

[The06] The ALEPH, DELPHI, L3, OPAL, SLD Collaborations, the LEP Electroweak Working Group, the SLD Electroweak and Heavy Flavour Groups. Precision Electroweak Measurements on the Z Resonance. *Phys. Rept.*, 427:257, 2006.

[Tho09] MA Thomson. Particle flow calorimetry and the pandorapfa algorithm. *Nuclear Instruments and Methods in Physics Research Section A: Accelerators, Spectrometers, Detectors and Associated Equipment*, 611(1):25–40, 2009.

[Top] Top pair production at 500 gev. `http://www.ilcild.org/documents/optimization/loi-physics-analyses-1/top-pair-production-at-500-gev`.

[UAF+09] V. Uzhinsky, J. Apostolakis, G. Folger, VN Ivanchenko, MV Kossov, and DH Wright. Geant4 simulation of hadronic interactions at 8–10 gev/c: response to the harp-cdp group. *The European Physical Journal C-Particles and Fields*, 61(2):237–246, 2009.

[Wal09] R. Walsh. Flavour tag studies with the lcfivertex package. *Arxiv preprint arXiv:0901.4894*, 2009.

[web] Large Hadron Collider web. `http://lhc.web.cern.ch/lhc/`.

[Wei67] S. Weinberg. A model of leptons. *Physical Review Letters*, 19(21):1264, 1967.

[Whi] The whizard event generator. `http://projects.hepforge.org/whizard/`.

[XHJHD01] S. Xella-Hansen, DJ Jackson, R. Hawkings, and C. Damerell. Flavour tagging studies for the tesla linear collider. Technical report, LC-PHSM-2001-024, 2001. `http://www-flc.desy.de/lcnotes/notes/LC-PHSM-2001-024.ps.gz`.